UNIVERSITY OF CALIFORNIA

Los Angeles

Microfabrication of Three-Dimensional Complex Structures for Biomedical Applications

A dissertation submitted in partial satisfaction of the

requirements for the degree Doctor of Philosophy

in Chemical Engineering

by

Sohyung Lee

2022

ABSTRACT OF THE DISSERTATION

Microfabrication of Three-Dimensional Complex Structures

for Biomedical Applications

by

Sohyung Lee

Doctor of Philosophy in Bioengineering

University of California, Los Angeles 2022

Panagiotis D. Christofides, Committee Co-Chair

Dino Di Carlo, Committee Co-Chair

The evolution of microfabrication has greatly contributed to the advances in biology and medicine, as it can interface with and manipulate the interactions between biological systems and materials with micrometer-scale precision. In addition, microfabrication allows the development of new materials with unique properties by providing the tools to tailor defined topography as well as overall geometry.

In the field of tissue engineering, to provide suitable functional microenvironments for cells or tissues, there is a great need to structure artificial tissue constructs at the micrometer scale. In

addition, micrometer-sized reactors with defined shape and spatial chemistries can be utilized for diagnostic applications to concentrate or enrich rare biomolecules or cells, otherwise not detectable. The dissertation reports on the development of novel multifunctional biomaterials to overcome current challenges in microfabrication techniques such as 3D bioprinting and microfluidics, highlighted in Chapter 1.

In Chapter 2, we present a highly biocompatible and elastic bioink for fabrication of complex biomimetic structures such as vascularized cardiac tissue constructs. The 3D bioprinting of soft tissues has been challenging primarily due to the lack of suitable bioinks. To address these shortcomings, we use recombinant human tropoelastin as a novel bioink with high printability, biocompatibility, biomimicry, and proper mechanical properties. Using the freeform reversible embedding of suspended hydrogels (FRESH) printing method, we demonstrate bioprinting vascularized cardiac constructs using two-nozzles and we extensively characterize their functions in vitro and in vivo.

In Chapter 3, we explore a scalable method to fabricate spatially functionalized microparticles for "lab on a particle" applications. For the design of a novel high throughput microfabrication method, we highlight the important role of thermodynamic factors, such as temperature and polymer concentrations, on intermolecular interactions, and therefore, the phase-separation behavior of a polymer mixture. These particles are utilized to analyze secretion phenotypes and heterogeneity of CHO DP-12 cells and to sort rare populations of high-yielding producer cells using fluorescence activated cell sorting (FACS).

In Chapter 4, we prove the broad generalizability of this lab-on-a-particle platform by demonstrating their ability to screen and sort primary human T cells as well as genetically engineered chimeric antigen receptor (CAR)-T cells based on cytokine production.

Overall, we believe the work presented here demonstrates the importance and utility of microfabrication techniques, especially 3D bioprinting and microfluidics. Combined with novel biomaterials, microfabrication methods can significantly upgrade conventional platforms, such that we can better recapitulate the in vivo microenvironment for tissue engineering or suggest an entirely new technology as with lab-on-a particle technology for single-cell analysis and sorting.

The dissertation of Sohyung Lee is approved.

Junyoung O. Park

Daniel Kamei

Panagiotis D. Christofides, Committee Co-Chair

Dino Di Carlo, Committee Co-Chair

University of California Los Angeles

2022

DEDICATION

This work is dedicated to my friends and family who have given me courage and support to continue my life journey. First, I must acknowledge my parents who always emphasized the importance of education and taught me to be curious. Your unconditional love and trust kept me on the right track.

I would also like to thank Sevana Baghdasarian, Ehsan Shirzaei Sani, Brian Walker and Tricia Walker who brighten my world and helped me feel home in a foreign country. You are my best friends, teachers, and family to me.

I appreciate every member of the Di Carlo lab who taught me to become a better researcher. We shared the challenges and triumphs of working in a lab. I look forward to hearing of your future successes and accomplishments.

Lastly, I must acknowledge my incredible advisor Dino Di Carlo who is extremely talented and committed to his profession. Thank you for taking a chance on me and teaching me the joy of research. It was my best luck to see you in vicinity how kindly and peacefully you can orchestrate the lab.

For me, doctoral training was a process in which I could learn how to adapt to a new environment, troubleshoot problems, and manage myself in addition to building scientific knowledge. I would like to thank all of you who watch over my steps, guides and encouraged me to move forward.

TABLE OF CONTENTS

ACKNOWLEDGMENTS

Chapter 2 is adapted from “Human Recombinant Elastin Based Bioinks for 3D Bioprinting of Vascularized Soft Tissues” Advanced Materials, 2020, 2003915. Doi.org/10.1002/adma.202003915. SL, ES, YG performed experiments. ARS aided in experimental set up. SL prepared manuscript. ASW, NA provided guidance throughout the work and manuscript.

Chapter 3 is adapted from "Scalable Fabrication and Use of 3D Structured Microparticles Spatially Functionalized with Biomolecules" ACS Nano, 2021. Doi.org/10.1021/acsnano.1c05857. SL performed all experiments. JD, RD, DK aided in experimental set up. SL, JD, DD prepared manuscript. DD provided guidance throughout the work and manuscript.

Chapter 4 is adapted from unpublished work on “Selective Nanovial Capture and Single-Cell Sorting of Antigen-Specific T Cells Based on Cytokine Secretion” done by DK, SL, RD, MS, CS, WW and DD. RD, WW and DD conceived and planned out the main experiments of this Study. DK, SL, RD, MS and CS performed experiments. DK, SL prepared manuscript. DD provided guidance throughout the work and manuscript.

VITA

Education

M.S. in Chemical and Biomolecular Engineering, Seoul National University, South Korea (2014)

B.S. in Chemical and Biomolecular Engineering, Seoul National University, South Korea (2012)

Research Appointment

Graduate Student Researcher, University of California, Los Angeles (2018-2022)

Research Engineer, Samsung Electronic Materials Research Center, South Korea (2014-2017)

Publications

[1] S. Lee, J. de Rutte, R. Dimatteo, D. Koo, D. Di Carlo, "Scalable Fabrication and Use of 3D Structured Microparticles Spatially Functionalized with Biomolecules" ACS Nano, 2021, in press.

[2] S. Lee, J. de Rutte, R. Dimatteo, D. Koo, D. Di Carlo, "Scalable Fabrication of 3D Structured Microparticles Using Induced Phase Separation." bioRxiv, 2021.

[3] S. Lee, E. Shirzaei Sani, A. R. Spencer, Y. Guan, A. S. Weiss, N. Annabi, "Human Recombinant Elastin Based Bioinks for 3D Bioprinting of Vascularized Soft Tissues" Advanced Materials, 2020, 2003915.

[4] M. van Zee, J. de Rutte, R. Rumyan, C. Williamson, T. Burnes, R. Radakovits, A. S. Eugenio, S. Badih, S. Lee, D. Lee, M. Archang, D. Di Carlo, "High-throughput Selection of Cells Based on Accumulated Growth and Division Using PicoShell Particles" PNAS, in revision.

[5] J. de Rutte, R. Dimatteo, M. M. Archang, M. van Zee, D. Koo, S. Lee, A. C. Sharrow, P. J. Kroh, M. P. Mellody, S. Zhu, J. Eichenbaum, M. Kizerwetter, S. Udani, K. Ha, A. L. Bertozzi, J.

B. Spangler, R. Damoiseaux, and D. Di Carlo, “Suspendable microcontainers for massively parallel single-cell functional analysis and sorting”, under review.

[6] U. Gokberk, J. Jones, S. Baghdasarian, N. Kaneko, E. Shirzaei Sani, S. Lee, S. Gholizadeh, S. Tateshima, N. Annabi "Engineering elastic sealants based on gelatin and elastin-like polypeptides for endovascular anastomosis" Bioengineering & Translational Medicine, 2021, e10240.

Conference Proceedings

[1] S. Lee, J. de Rutte, R. Dimatteo, D. Koo, D. Di Carlo, “Scalable Fabrication of 3D Structured Microparticles Using Induced Phase Separation”, SLAS, February 2022, Boston, Massachusetts, USA. (Tony B. Award)

[2] S. Lee, J. de Rutte, R. Dimatteo, D. Koo, D. Di Carlo, “Scalable Fabrication of 3D Structured Microparticles Using Induced Phase Separation”, MicroTAS, October 2021, Palm Springs, California, USA. (Best Poster Presentation Award)

[3] S. Lee, A. R. Spencer, E. Shirzaei Sani, A. S. Weiss, N. Annabi, “Engineering a Highly Elastic Protein-Based Bioink for Printing Complex Soft Tissues”. AIChE Annual Meeting, October/November 2018, Pittsburgh, PA, USA. (Podium Presentation)

[4] D. Koo, S. Udani, R. Dimatteo, S. Lee, D. Di Carlo, “Sorting Single-Cells Based on Extracellular Vesicle Secretion Using 3D Structured Microparticles”, MicroTAS, October 2021, Palm Springs, California, USA.

[5] L. A. Jackson, H. Shi, J. F. Acevedo, S. Lee, N. Annabi, R. A. Word, M. E. F. Rodriguez, “Effect of Gelatin Methacryloyl (GelMA) Hydrogel on Healing of the Vaginal Wall”. IUGA Annual Meeting, September 2019, Nashville, TN, USA.

Chapter 1 Biomedical Applications of Different Micro-fabrication Techniques

In biomedical field, microfabrication is a technology that broadly describe manufacturing of physically or chemically complex products using biology-based materials such as living cells, extracellular matrices, and biocompatible polymers.[1-2] This technology has enabled the manufacture of custom-designed implants and the precise control over the cellular microenvironment in cell culture, addressing challenges in tissue engineering, *in vitro* cell culture studies and many other biomedical applications. For example, different microfabrication techniques can be used to modify the surface of scaffolds with important functional groups in biology including hydroxyl, methyl, carbonyl, carboxyl, amino, phosphate, and sulfhydryl groups, enabling to achieve a certain surface charge, cellular/molecular interactions, or wettability.[3]

Microfabrication techniques, such as 3D bioprinting has proven its potentials to generate constructs that more closely recapitulate the complexity and heterogeneity of tissues and organs than traditional regenerative medicine therapies.[4] Such constructs can be applied for tissue regeneration or as in vitro 3D models. The potential of biofabrication technology is not limited to the traditional medically oriented tissue engineering and organ printing. It provides the unprecedented abilities for developing highly predictive cell- and tissue-based technologies for drug delivery and cell-based assays.[5]

As this field is maturing and growing, scientists with different backgrounds and skills are joining this field. This chapter is to provide an introduction for different microfabrication technologies and their potential applications in biology and medicine, as well as a discussion of the common challenges being faced by the technologies.

1.1. Soft lithography

Soft lithography is a general term include microfabrication techniques that use elastomeric stamps to pattern or mold materials at micro/nano-scales. In soft lithography, the precursor material is casted and cured on previously fabricated masters to make defined structures. Though the master mold is typically fabricated by photolithography which requires expensive clean-room facilities, the subsequent fabrication steps can be performed in common wet lab area. The master molds can be re-used repeatedly with a proper care, minimizing the need for access to the clean room facilities. Therefore, soft lithography is considered as a simple, low-cost, and high-throughput process to fabricate micro- and nanoscale patterns of different materials.

Numerous soft lithography-based patterning techniques have been investigated in a wide range of biomedical applications. One important application of soft lithography in biology is control the topography and the spatial distribution of molecules on a surface so that it either promotes or resists the adhesion of proteins or anchorage-dependent cells.[6] Using this strategy, cells were isolated on a defined surface to study behavior of single cells instead of relying on statistical distributions based on ensembles of cells. In another example, high-density arrays of microscopic wells which were as small as size of a cell were fabricated by replica molding of PDMS against a master of photoresist.[7] The surface of wells was coated with an adhesive extracellular matrix protein such as fibronectin that promotes cell adhesion, while the space between the wells were treated with materials that resist the adhesion of proteins and cells (i.e. bovine serum albumin). The micro-well platform can be applied to cell-based screens such that it enables identifying the phenotype of a cell in a population of heterogeneously transfected cells. Using the platform, the production of a fluorescently labeled gene product could be localized and detected in the well.

Cells can be encapsulated within hydrogels using soft lithography techniques. Encapsulation of mammalian cells within hydrogels has great utility for a variety of applications ranging from tissue engineering to cell-based assays.[8] The use of microgels such as microrods or microbeads and hydrogels with micro-feature such as microchannels, has been useful in various tissue engineering applications.[9] These gels could be subsequently assembled to form complex 3D structures. Also, the encapsulation of cells in microgels can prevent cell aggregation, which can be useful for stirred bioreactor experiments. Furthermore, cell-laden hydrogels can be coated with various polymers to immunoisolate the encapsulated cells from the surrounding environment, preventing allogenic or xenogeneic responses from the host's immune system when the cell-laden hydrogels were implanted.

1.2. Electrospinning

Electrospinning is a relatively old technology which was first discovered and described as the behavior of magnetic and electrostatic phenomena in the late 16th century. The fiber meshes are created by passing a biomaterial solution through a high-voltage electric field near the deposition nozzle. The high voltage charges a liquid droplet so that their electrostatic repulsion counteracts the molecular cohesion of the liquid (surface tension), which stretches liquid droplet and forms a charged liquid jet. The liquid stream is dried in flight and collected on a grounded plate, making a fiber mesh with micro/nano-scale surface texture. The technique was originally developed for manufacture of textile, but now it is widely adopted for biomedical applications, because it can produce fiber meshes that resemble native extracellular matrix (ECM).

Simon, in a 1988 NIH SBIR grant report, showed that solution electrospinning could be used to produced nano- and submicron-scale polystyrene and polycarbonate fibrous mats specifically

intended for use as in vitro cell substrates.[10] This early application of electrospun fibrous lattices for cell culture and tissue engineering showed that various cell types would adhere to and proliferate upon the fibers in vitro. The eletrospun fibers have been investigated for wound dressings, medical implants, and scaffolds for artificial human tissues and these scaffolds fulfill a similar purpose as the extracellular matrix in natural tissue.[11-13] Biodegradable polymers, such as polycaprolactone and polysaccharides, are typically used for this purpose. These fibers can be coated with other biomaterials to give additional benefits to the scaffolds such as improved cell adhesion and cellular growth.

1.3. Microfluidics

The behavior of fluids at the micro-scale that differs from the behavior of bulk fluid because the influence of surface tension, energy dissipation, and fluidic resistance become more dominant when the liquid body is at micro-scale. Microfluidics is a field of study focuses on these unique properties of the micro-scale fluid as well as the ability to hold a minimal volume of liquid and apply these factors for multiple research areas.

To confine fluids in micro volume, microfluidics research is performed on a small device which consists in micro-channels etched or molded into a different material such as glass, silicon and a polymer. Since George Whitesides in 1998, for the first time introduced the use of PDMS in microfluidics,[14] PDMS has become the primary material of choice, and it has been playing an essential role in microfluidics and enabling the rapid prototyping of microfluidic devices via soft lithography. PDMS possesses unique advantages for biomedical applications including biocompatibility, optical transparency, flexibility, and durability, which made microfluidics technology a powerful tool for biologists to control the complete cellular environment, leading to

new questions and discoveries. Different designs of PDMS microfluidics chips were created for cell biology applications, such as sorting or patterning cells and proteins, cells-based biosensors, studies of cocultures.

Microfluidic chips are beneficial in that they require small fluid volumes and provide faster analysis and precise control over the on-chip experiments, which enables the integration of almost all the processes required for complete biological, chemical and biomedical protocols on a single microfluidic chip, often called labs-on-chips. One important subset of labs-on-chips is organs-on-chips where a microfluidic device recapitulates the complex structures and functions of living human organs. These three-dimensional human organ models can replace animals for testing of drugs and toxins, and they can exhibit the highly differentiated tissue structures and functions that was unavailable in conventional cell cultures or explant cultures of tissues.[15] To make organs-on-chips, microfluidic devices are selectively patterned with cells by modifying the surface of the devices with cell adhesion molecules such as collagen and fibronectin. In recent research from Donald Ingber group, a human lung bronchial-airway model was fabricated to study the human-lung responses to infection by influenza and SARS-CoV-2 viruses and to test the efficacy of therapeutic drugs.[16] To make air-liquid interfaces, two parallel micro-channels separated by a porous membrane were coated with lung bronchial-airway epithelial cells and endothelial cells, creating an air channel and a vascular channel, respectively. Infection of human airway chips were achieved by injecting a fluid containing viruses into the air channels, and neutrophils were perfused in their vascular channel to study the interaction between influenza virus and neutrophils. The resulting device exhibited multiple physiologically relevant features such as mucus layer formation, cross-talk between the epithelium and endothelium, mucociliary clearance, and recruitment of

circulating immune cells which play critical roles in the host responses to infection by respiratory viruses.

On the other hand, droplet microfluidics has been extensively utilized as powerful tools to fabricate high-throughput monodisperse microdroplets or micro-hydrogels for tissue engineering and molecular analysis. Conventional macro-scale tissue scaffolds have limited oxygen delivery because the oxygen diffusion limit within hydrogel scaffolds is often below 200 μm. To avoid that, cells can be encapsulated within microgel by injecting cell-laden precursor solution into a microfluidic droplet generator and polymerizing the cell-laden microdroplets.[17] The cell-laden microgels have a large surface-area-to-volume ratio, which lead to efficient mass transfer and enhanced interactions between cells and their surrounding ECM. Another tissue engineering application of microgels is interconnected microporous annealed particle (MAP) scaffold. [18] In MAP technology, cells are cultured in a scaffold composed of microgel building blocks that circumvent the need for material degradation prior to tissue ingrowth by providing an interconnected network of micropores for cell migration and proliferation.

The droplet microfluidics provides a high-throughput and precise analytics tool which led to its widespread application in single-cell analysis. The ability to fabricate monodisperse water-in-oil emulsions is exploited to enrich the target biomolecules such as single-cell RNA or secretions within sub-microliter volume of liquids, revealing the heterogeneous behavior of cells which are overlooked in conventional analog assays, typically performed in a well-plate.[19-20] There are three prevalent droplet-based single-cell RNA sequencing (scRNA-sq), inDrop, Drop-seq and 10x Genomics that are extensively studied in literature.[21-23] In these scRNA-sq platforms, droplet microfluidics were used to encapsulate single cells and barcoded beads in droplets where cells are

lysed to release mRNA. Reverse transcription and cDNA amplification are carried out before or after demulsification of droplets.

1.4. 3D Bioprinting

Three dimensional (3D) bioprinting is the utilization of 3D printing–like techniques to combine cells, growth factors, and biomaterials to fabricate biomedical parts, often with the aim of imitating natural tissue characteristics. Tissue engineering offers tremendous potential to overcome issues with organ transplant shortage, drug screening, and to study molecular phenomena that are involved in higher biological functions (such as tissue morphogenesis, wound healing, inflammatory reactions).[24] However, conventional planar fabrication techniques are unable to create the complex multiscale architecture such as the interface between the vascular endothelium and surrounding connective tissue and parenchymal cells, which allows them only to investigate basic functions of the respective tissue.[25] In that regard, 3D bioprinting, which can continuously move in Cartesian (XYZ) coordinates, holds great potential to address the unmet needs of tissue manufacturing to create realistic 3D tissue or organ models by mimicking the complex cellular arrangement of native tissues in 3D structures.

One of the greatest challenges in tissue engineering is to fabricate vascularized tissues that can easily integrate into the host's circulatory system with the architectural complexity of native tissues. It is reported that tissue constructs quickly develop necrotic regions when there is no perfusable vasculature within a few hundred microns of each cell. Therefore, different 3D bioprinting strategies have been developed to introduce vascular channels in tissue scaffolds.[26-27] Sacrificial inks that leave a hollow structure behind after washing, have been used successfully to make vascularized constructs.[28] Pluronic, PVA, glass and gelatin have been embedded within a different

surrounding material and washed after polymerization of the constructs to create vascular network. These channels were often seeded with human umbilical vein endothelial cell (HUVEC), obtaining perfusable endothelialized vascular channels. The needle gauge can be replaced to fabricate vascularized constructs with different sizes to mimic the hierarchical vascular networks in native tissues.

On the other hand, coaxial extrusion printing has been increasingly explored for direct 3D bioprinting of vascular constructs.[29-31] The nozzle of coaxial printer is a concentric set of coaxial capillaries composed of an outer and inner needle, which enables simplified printing process and scalability. Jia et al. designed a multi-layered coaxial extrusion bioprinting system and successfully fabricated a range of cell-laden vascular constructs using a biocompatible hydrogel mixture containing GelMA, alginate and PEGDA.[32]

Another printing method that has been used to create vascular networks is stereolithography (SLA) 3D printing.[33-34] SLA printing works by selectively curing a light sensitive liquid resin within a vat in a layer by layer fashion using photochemical processes. Cui et al. recently employed SLA to fabricate a 3D vascularized model, that allows circulation of oxygen and cell growth gradients, to investigate the breast cancer metastasis to bone.[34] By using a light crosslinkable material, GelMA/PEGDA with or without nano-hydroxyapatite (nHA), the author successfully printed a 3D vascularized construct which consists of three chambers: micro-vascularized bone, endothelialized vessel and cancer tumor.

Chapter 2 3D Bioprinting of Complex Soft Tissues Using Elastin-Based Multifunctional Bioinks

2.1. Introduction

Tissue engineering offers tremendous potential to overcome issues with organ transplant shortage, drug screening, and to study molecular phenomena that are involved in biological functions such as tissue morphogenesis, wound healing, and inflammatory reactions.[24] However, conventional planar fabrication techniques are unable to create the complex multi-scale architectures such as the interface between the vascular endothelium and surrounding connective tissue and parenchymal cells. This may limit the applications of these structures for studying basic functions of the respective tissues.

A recent interesting development in the field of tissue engineering is the use of three dimensional (3D) bioprinting technologies to merge the use of cells, biomaterials, and microfabrication.[35-37] The selection of a proper biomaterial as the ink is important for 3D bioprinting of constructs with biomimetic architectures and properties. In the past few years, different biomaterials, including synthetic polymers,[38-39] natural polymers,[40-41] and decellularized extracellular matrix (ECM),[42] have been engineered as bioinks to print complex 3D structures such as perfusable vascular networks. For example, in a recent study, Dvir and colleagues 3D bioprinted a decellularized ECM hydrogel into a vascularized heart model.[43] However, the construct was not perfused long term *in vitro*, and the viability and function of the encapsulated cells were not reported. Alternatively, different techniques such as casting[44] and sacrificial ink-writing,[26] that involve extra processing steps, have been combined with 3D bioprinting to mimic vasculatures. The fabrication of complex biomimetic structure that are entirely based on 3D bioprinting is still challenging primarily due to

the lack of suitable bioinks with high printability, biocompatibility, biomimicry, and proper mechanical properties. Therefore, new biomaterial-based approaches are needed to address the limitations of currently available bioinks.

2.2. Results and Discussion

Here, we present a highly biocompatible recombinant human tropoelastin-based bioink for 3D bioprinting of complex soft tissues. The engineered bioink is composed of two ECM-based biopolymers gelatin methacryloyl (GelMA) and methacryloyl-substituted recombinant human tropoelastin (MeTro) which can be crosslinked with visible light. ECM materials have been widely used in tissue engineering field given that they provide a cell the environment similar to its origin. However, tropoelastin as one of the main components of connective tissues has not yet been studied for 3D bioprinting of soft tissues. Our recombinant human tropoelastin is identical to the naturally secreted human form. Elastic fibers are integral to vertebrate tissues such as blood vessels, skin, lung, and heart, where strength and elasticity are required for regular tissue function (i.e. stretching and contracting). Elasticity of tropoelastin originates from its intermolecular alignment governed by a modular structure of alternating hydrophobic and hydrophilic domains including lysine residues (Figure 2-1A). In addition to intrinsic elasticity and resilience, tropoelastin provides cell binding motifs and cell signaling pathways.[45] Though the binding site or mechanism of bonding are not clearly revealed, tropoelastin have been demonstrated to support endothelial cell recruitment and growth and to play a significant role in migration and angiogenesis.[46-47] In addition to tropoelastin, gelatin was selected as a base material in bioink formulation due to its properties. Gelatin is an irreversibly hydrolyzed form of collagen, yet possesses many characteristics of collagen (i.e. cell-binding sites, and matrix-metalloproteinase (MMP) degradation sites).[48] While elastin is synthesized in the body by enzymatic cross-linking of lysine residues of tropoelastin,

recombinant human tropoelastin can be chemically modified with methacryloyl groups to synthesize MeTro, which can be photopolymerized to form highly elastic hydrogel (Figure 2-1B).[49] Similarly, gelatin backbone can be also chemically functionalized with methacryloyl groups to form GelMA (Figure 2-1C).[50] While GelMA in the bioink supports an amenable cell culture environment,[51] the incorporation of MeTro enhances elasticity and mechanical stability for the printed structures.[52] An optimized formulation of bioink based on testing different ratios of GelMA/MeTro was used as a versatile platform for 3D bioprinting of soft tissues.

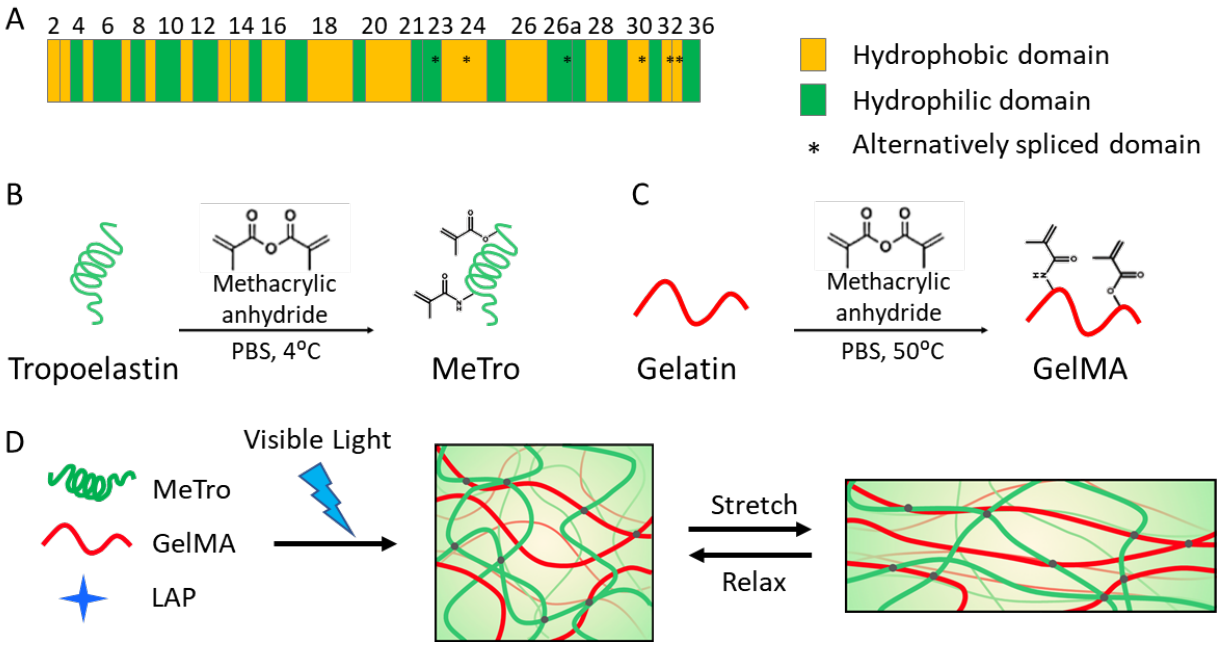

Figure 2-1. Synthesis of GelMA/MeTro composite hydrogel. (A) Domain map of human tropoelastin. Methacrylation of (B) tropoelastin and (C) gelatin. (D) A schematic to describe the formation of MeTro/GelMA hydrogels. GelMA and MeTro polymers are covalently crosslinked upon exposure to visible light in the presence of LAP photoinitiator to form a highly elastic hydrogel network.

In our previous work, we engineered GelMA/MeTro composite hydrogels for different tissue engineering applications such as wound healing[53] and nerve tissue regeneration[54]. Here, we aim to explore the use of GelMA/MeTro as ink for 3D bioprinting of vascularized soft tissues such as cardiac tissue. Due to the hydrophobic hydration of tropoelastin, water molecules around tropoelastin are expelled at temperatures above a characteristic transition temperature, which results in coacervation of tropoelastin. Therefore, solutions of tropoelastin or MeTro, whose solubility is identical with tropoelastin, in this study were handled in temperature around 8 °C. We previously reported that the Young's moduli of the visible light crosslinked MeTro/GelMA hydrogels, using Eosin Y/triethanolamine (TEA)/N-vinylcaprolactam (VC) photoinitiation system, was in the range of 4.05–10.25 kPa,[55] which was comparatively lower than those for UV crosslinked MeTro/GelMA hydrogels using Irgacure 2959 (16.5–49.8 kPa).[56] Although the UV crosslinked hydrogels were highly elastic, the procedure required exposure to UV light for a few min, which can be harmful for the encapsulated cells by damaging their DNA.[57] To eliminate the negative effects of UV irradiation, in this study, we investigated another photoinitiator, lithium phenyl-2,4,6-trimethylbenzoylphos-phinate (LAP), to photopolymerize the bioprinted structures containing different type of cells (Figure 2-1D). LAP can initiate photocrosslinking around 405 nm and demonstrated remarkable advantages as compared to other photoinitiators, including high water solubility and low cytotoxicity.[58] To verify the crosslinking within the hydrogels, the ^{1}H NMR (400 MHz) spectra of the MeTro/GelMA hydrogels was compared with MeTro and GelMA prepolymers (Figure 2-2). The results demonstrated that 87.7 ± 8.6% of the methacryloyl groups in the MeTro/GelMA prepolymers were involved in the formation of the hydrogel network.

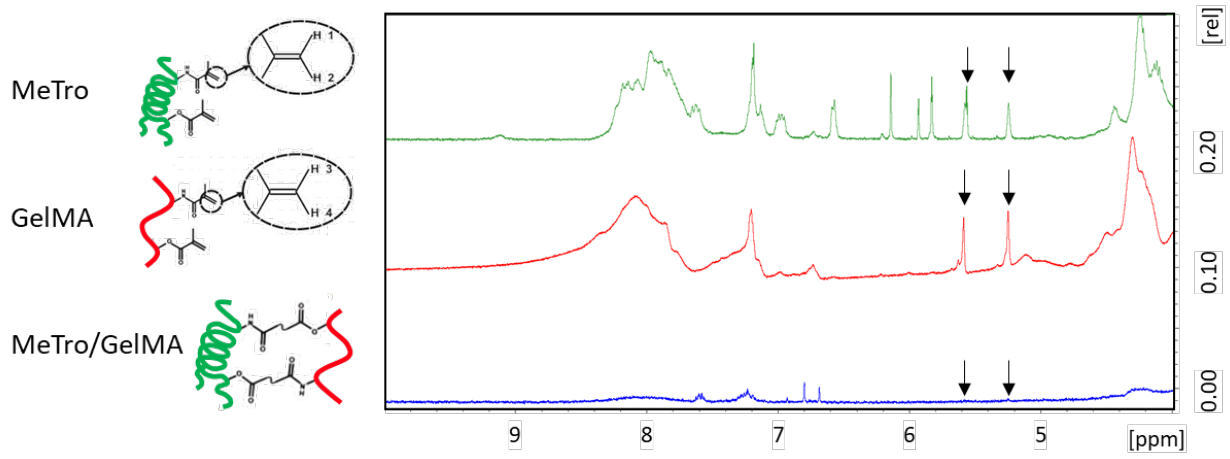

Figure 2-2. ^{1}H NMR (400 MHz; D_2O) spectra of MeTro prepolymer, GelMA prepolymer, and MeTro/GelMA hydrogels confirming the degree of crosslinking in the composite to be 87.7 %.

Tensile tests demonstrated statistically significant differences in the mechanical properties between the composites, pure GelMA and MeTro hydrogels. Specifically, the tensile modulus of MeTro/GelMA hydrogel was calculated to be 47.9 ± 2.6 kPa, which was higher than the value for pure MeTro (39.7 ± 3.8 kPa), and lower than pristine GelMA hydrogel (79.2 ± 8.5 kPa) (Figure 2-3A, B). In contrast, an opposite trend was observed for the extensibility and ultimate stress values (Figures 2-3A, C). As expected, pure MeTro hydrogel had extensibility around 2-fold higher than pure GelMA hydrogel and the MeTro/GelMA exhibited extensibility of 33.1 ± 8.3 %. Cyclic compression test showed similar trend where MeTro/GelMA hydrogels presented compressive modulus of 49.2 ± 8.7 kPa between the modulus of pure GelMA (46.6 ± 5.6 kPa) and pure MeTro hydrogels (70.2 ± 13.2 kPa) (Figure 2-3D, E). In addition, energy loss calculation proved that the addition of MeTro increased the resilience of the composite hydrogel by showing a reduced energy loss for both MeTro and MeTro/GelMA hydrogels as compared to pristine GelMA hydrogel (Figure 2-3F, J).

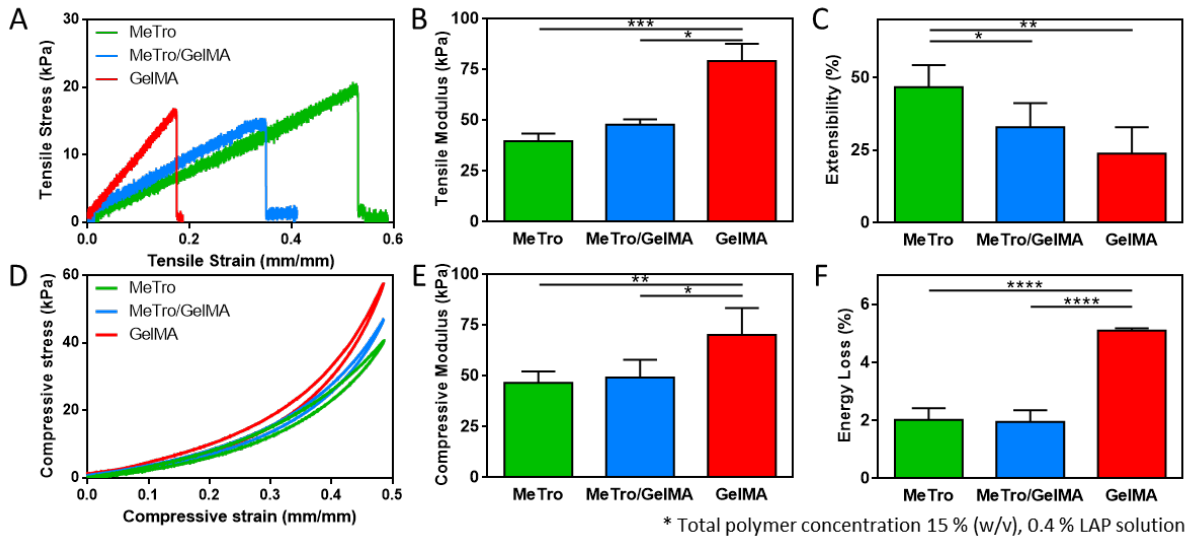

Figure 2-3. Mechanical characterization of GelMA/MeTro composite hydrogel. Mechanical properties of MeTro, GelMA and MeTro/GelMA composite hydrogels, showing (A) representative tensile stress-strain curves; (B) tensile moduli; (C) extensibility; (D) representative compressive stress-strain curves; (E) compressive moduli; and (F) energy loss. (* $p<0.05$, ** $p<0.01$, *** $p<0.001$, **** $p<0.0001$)

Biodegradable hydrogels are the most promising bioinks for 3D bioprinting as they mimic salient features of ECMs, can be modified to achieve mechanics similar to soft tissues, and can support cell adhesion and proliferation. However, many of these hydrogel precursors shear easily and have a low resistance to deformation, which limits their utilization as bioinks for 3D printing purpose. To address this limitation, rheology modifiers such as glycerol,[59] cellulose nanofibers,[60-61] or silicate nanoparticles[38, 61-63] have been used to endow the enhanced printability to the existing bioinks. However, these additional bioink components can alter the mechanical and physiological properties of the resulting printed structures, which can negatively affect the cell growth and

differentiation within the materials. Therefore, sacrificial materials, such as alginate[64] and poloxamer 407[65] have been used to improve printability of hydrogel-based bioinks. In this study, cold water fish gelatin was used as a sacrificial material to enhance the printability of the designed bioink (Figure 2-4A).

The MeTro/GelMA solution originally exhibited a viscosity (η) of ~162.6 mPa·s at shear rate of ~50 s^{-1} and temperature of ~8 °C which were close to the conditions used during printing (Figure 2-4B). The addition of gelatin transforms the solution into a viscoelastic fluid and imparts the shear thinning behavior under 10 °C due to the reversible gelation of gelatin (Figure 2-4C, D). The resulting material, referred to MeTro/GelMA bioink, possesses a viscosity that exceeded 3000 mPa·s which was 20-fold higher than the composite bioink without gelatin. The non-Newtonian behavior of this bioink was also evidenced by its high storage modulus (G′) over the loss modulus (G″) (Figure 2-4E).

Although the use of gelatin increases the rheological properties, the uncured ink lacks the ability to provide mechanical stability and immediately deforms upon exiting the nozzle. Thus, we utilized a freeform reversible embedding of suspended hydrogels (FRESH) printing technique to enable the fabrication of complex structures.[66] Carbopol bath was used due to its biocompatibility and ease of processing. Our biocompatible support bath is mainly composed of crosslinked poly(acrylic acid) particles, which can be deswollen post printing and removed from the structure permanently. Following photopolymerization of the printed construct, Carbopol bath was liquefied by addition of monovalent cations such as Dulbecco's phosphate-buffered saline (DPBS) and the print was released from the Carbopol.

Next, extrusion pressure and printing speed for 3D printing of MeTro/GelMA bioink were optimized to achieve the optimal printing time, provide structural integrity to the printed

constructs, and reduce stress to the cells during the printing process. We indirectly measured actual shear stress on the cells to study the impact of the extrusion pressure on the cells encapsulated within the bioink. The results revealed that the shear stress increased from 0.79 to 1.17 kPa, when the extrusion pressure increased from 5 kPa to 25 kPa (Figures 2-4F, G).

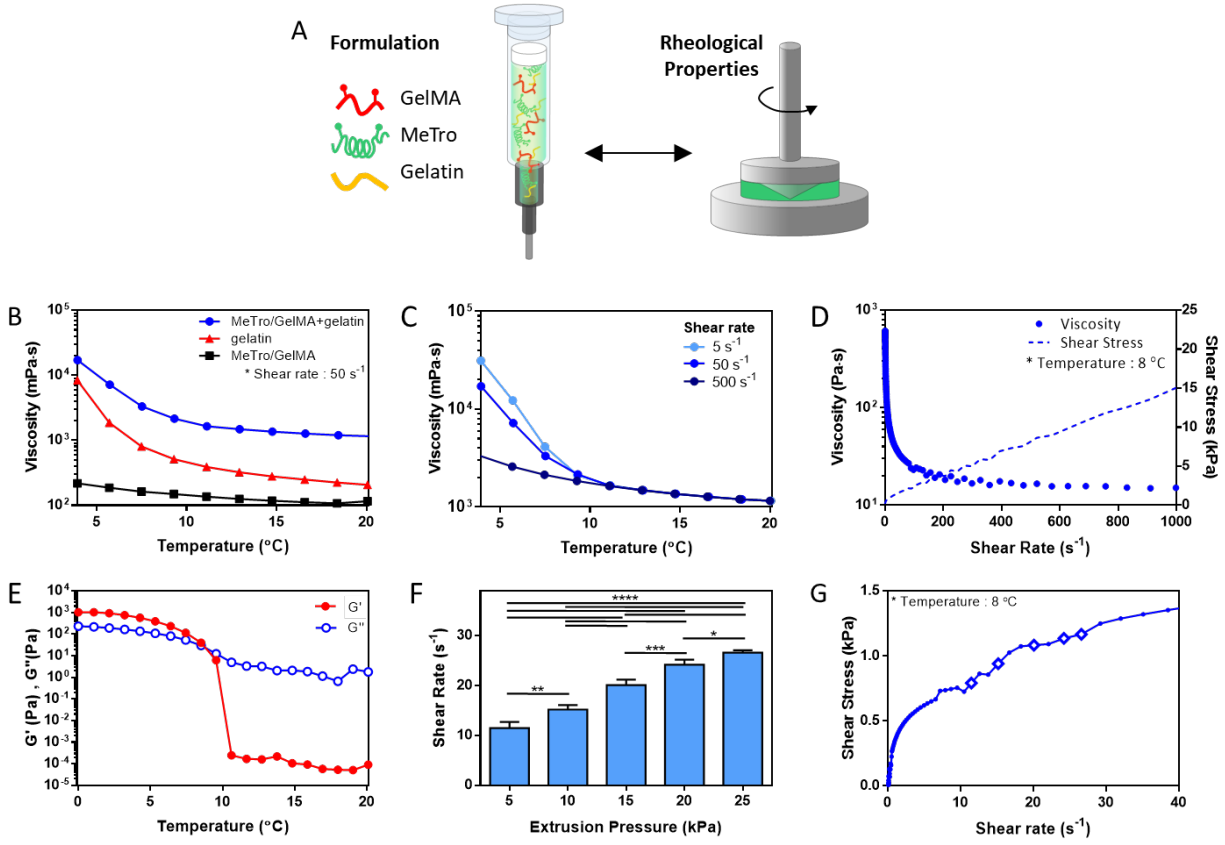

Figure 2-4. Rheological properties of MeTro/GelMA bioink. (A) Bioink formulation for 3D bioprinting. (B) Viscosity of MeTro/GelMA/gelatin, gelatin, and MeTro/GelMA as a function of temperature at shear rate 50 s^{-1}. Rheological properties of MeTro/GelMA bioink. (C) Temperature dependence of viscosity of MeTro/GelMA bioink with different shear rate. (D) Viscosity and shear stress of MeTro/GelMA bioink as a function of shear rate. (E) Storage modulus, G′, and loss modulus, G″, of MeTro/GelMA bioink formulations as a function of temperature. (F) Shear rate during the 3D printing of MeTro/GelMA Bioink as a function of extrusion pressure. (* $p<0.05$, **

p<0.01, *** p<0.001, **** p<0.0001) (G) Shear stress of MeTro/GelMA bioink measured as a function of shear rate. The diamond points indicate the actual shear stresses on the cells encapsulated in the bioink exiting the nozzle under the extrusion pressures 5, 10, 15, 20, and 25 kPa, respectively (from left to right).

To qualitatively assess the printability of MeTro/GelMA bioink, curved-line structures were printed under different printing speeds from 10 mm/s to 50 mm/s and extrusion pressures from 5 kPa to 25 kPa (Figure 2-5A). The printing conditions were categorized into good, normal and bad. Based on the results, the final printing condition was selected to be 15 kPa pressure and 30 mm/s speed at 8-10 °C which had 1.08 kPa of shear stress on the cells in MeTro/GelMA bioink (Figure 2-5B). The flow of MeTro/GelMA bioink exiting the nozzle was smooth without clogging and the resulting constructs after crosslinking were mechanically stable and robust, allowing to print multi-layered constructs. To ensure reliable printing fidelity of our bioink and printing system, constructs with complex architecture were designed and printed with different sizes and heights including a heart slice, a lattice cube, and a cat toy (Figure 2-5C, D).

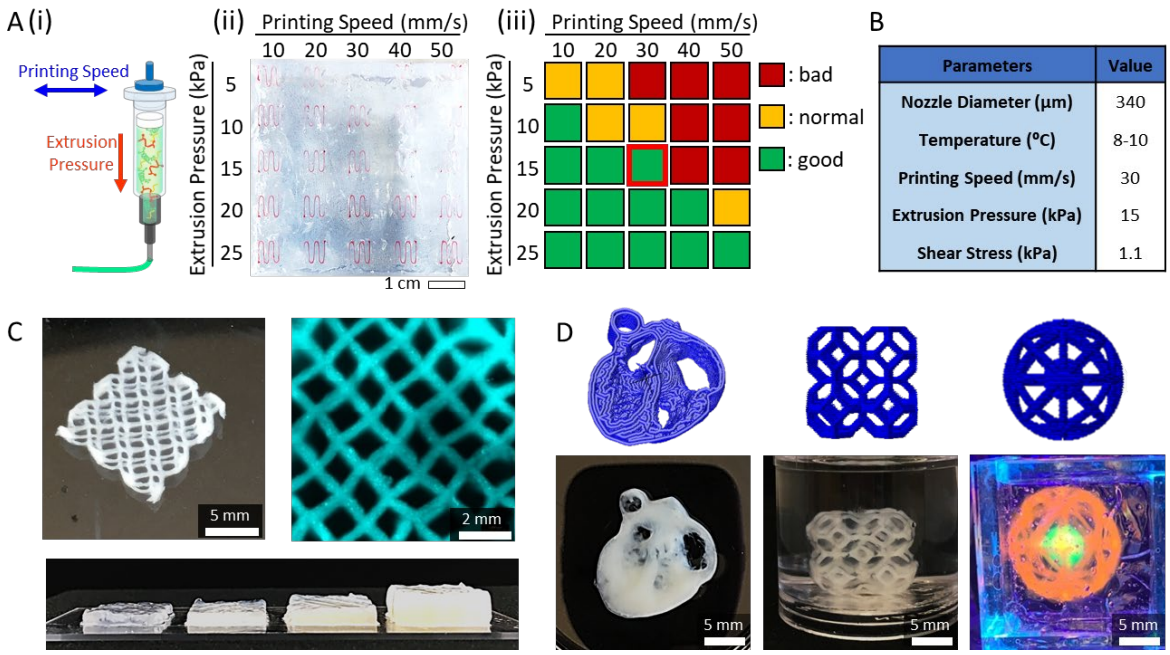

Figure 2-5. Optimization of 3D printing parameters. (A) Optimization of the printing speed and extrusion pressure: (i) a schematic to illustrate printing speed and extrusion pressure; (ii) MeTro/GelMA bioink filaments printed into the support bath at different printing pressures and speeds; (iii) qualitative evaluation of the MeTro/GelMA bioink printability at different printing pressures and speeds. (B) Optimized printing parameters for MeTro/GelMA bioink. (C) A lattice-shaped construct printed up to 16 layers to form constructs with a linear relationship between the number of layers and the height of the construct. (D) Various 3D constructs printed with MeTro/GelMA bioink (from left to right: heart slice, lattice cube and cat toy).

Lattice constructs were printed up to 16 layers (corresponding to 5 mm) and a linear relationship was obtained between the number of layers and the height of the construct (Figures 2-6).

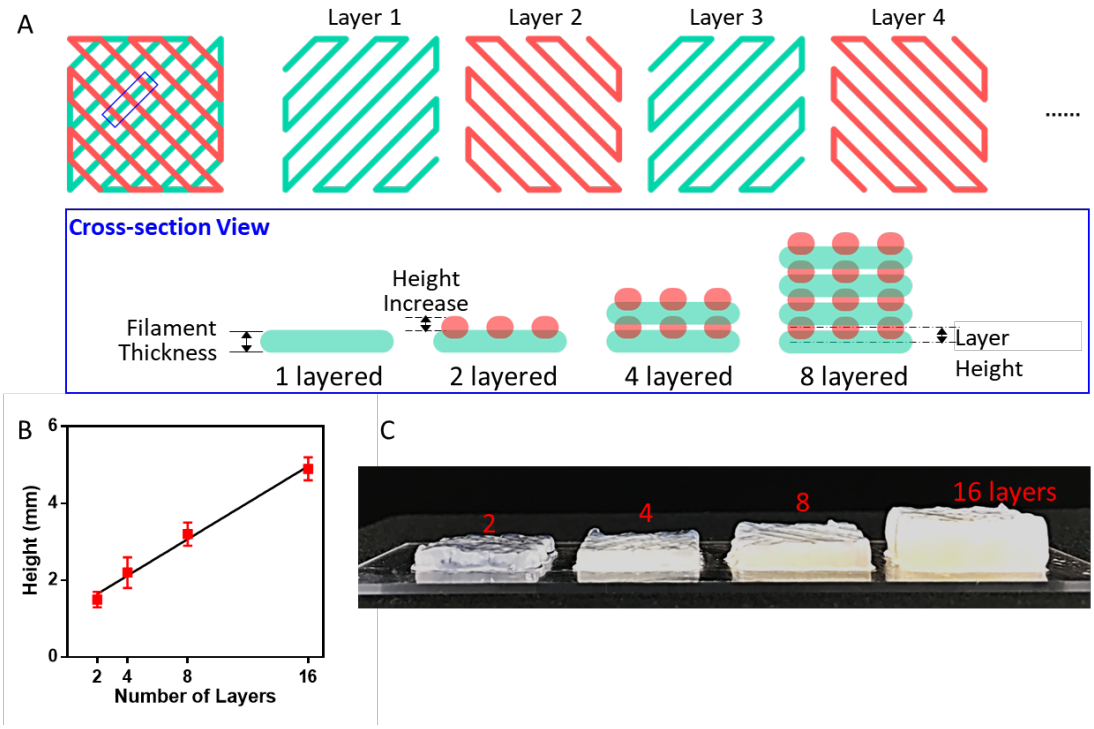

Figure 2-6. MeTro/GelMA lattice constructs printed up to 16 layers to form constructs with a linear relationship between the number of layers and the height. (A) Schematic representation of layer-by-layer printing of multi-layered lattice structure. Each layer was overlapped with the next layer to form an interconnected construct. (B) The heights of printed lattice constructs as a function of the number of layers. (C) Representative images of the printed lattice constructs with different number of layers.

To test the stability of the 3D printed MeTro/GelMA lattice constructs in aqueous solution, the weight and microscopic structure of the constructs were monitored during a week of incubation in DPBS at 37 °C (Figure 2-7A-C). The results showed more than 30 %(w/w) of the original weight of the printed structures decreased in a day with no significant changes afterwards, implying the gelatin and residual Carbopol gel in the 3D printed constructs were removed during the first 24 h. The enzymatic degradation of 3D printed constructs was characterized using collagenase type II solution in DPBS for up to 14 days (Figure 2-7D). Since we observed significant amount of the

construct weight was lost due to the removal of gelatin and Carbopol, the printed constructs were incubated in DPBS at 37 °C in order to remove the residual gelatin and Carbopol for 3 days prior to the degradation test. Results showed 12.7 ± 2.5 % enzymatic degradation of the construct during the first 24 h, however, the degradation rate slowed down and reached 17.9 ± 3.5 % at day 14.

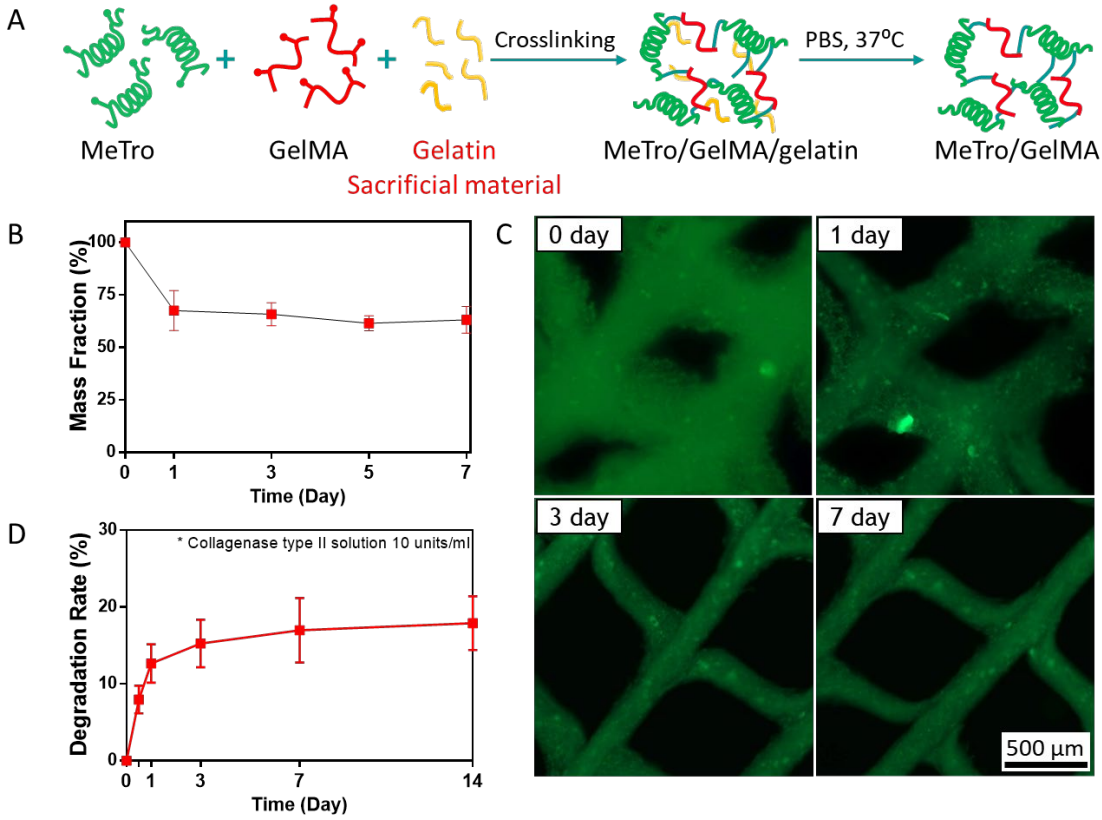

Figure 2-7. Post printing stability and degradation of 3D printed MeTro/GelMA constructs. (A) A Schematic illustration of gelatin diffusing out of the printed constructs during the incubation at 37 °C following the crosslinking. (B) Mass fraction of printed MeTro/GelMA constructs at days 0, 1, 3, 5 and 7 post incubation showing removal of remaining Carbopol and gelatin from the printed construct. (C) Microscope images of printed MeTro/GelMA constructs at days 0, 1, 3 and 7 post incubation. (D) Degradation rate of the lattice construct at days 0.5, 1, 3, 7 and 14 post incubation in collagenase solution.

Cytocompatibility of MeTro/GelMA bioink was studied using different cell types. First, 3T3 cells were used for 2D cell seeding on the printed structure as well as for bioprinting 3D cell-laden structures. In both 2D and 3D culture conditions, high cell viabilities (> 90 %) were achieved (Figures 2-8, 9).

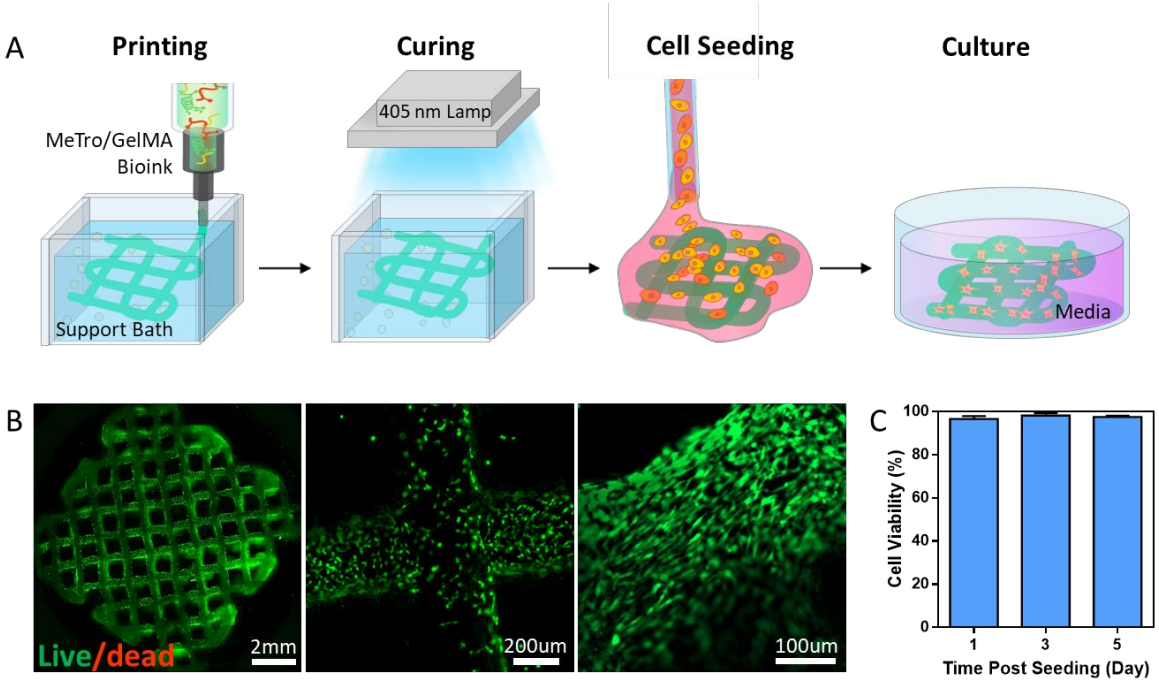

Figure 2-8. 2D cell seeding on 3D printed MeTro/GelMA constructs. (A) A schematic diagram of 2D cell seeding following the 3D bioprinting process. (B) Representative live/dead images of 3T3 cells seeded on 3D printed MeTro/GelMA constructs at day 3 post seeding. (C) Quantification of cell viability of 3T3 cells seeded on 3D printed MeTro/GelMA constructs at days 1, 3 and 5 post seeding.

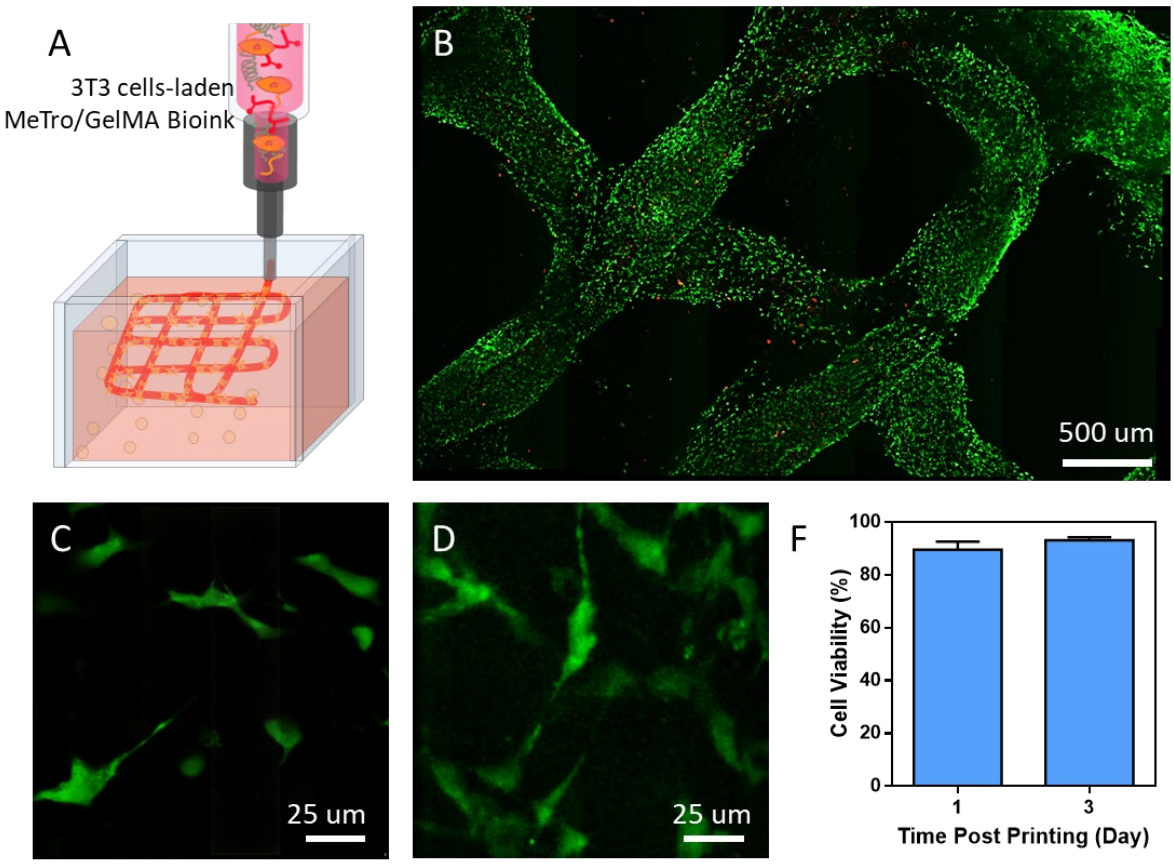

Figure 2-9. 3D bioprinting of 3T3 cell-laden MeTro/GelMA lattice. (A) Schematic showing the bioprinting of 3T3 cells-laden MeTro/GelMA bioink procedure. (B) A representative image of live/dead stained 3T3 cells within the 3D bioprinted MeTro/GelMA lattice at day 3. Representative live/dead images showing the distribution and spreading of 3T3 cells in the 3D bioprinted MeTro/GelMA constructs (C) at day 1 and (D) day 3 post printing. (C) Quantification of cell viability of 3T3 cells within 3D bioprinted MeTro/GelMA constructs at days 1 and 3 post bioprinting.

To evaluate the suitability of our engineered bioinks for printing cardiovascular tissues, we next encapsulate cardiomyocytes (CMs), cardiac fibroblasts (CFs) and human umbilical vein endothelial cells (HUVECs) within the MeTro/GelMA bioink to 3D bioprint constructs containing multiple cell types. A CM/CF-laden bioink and a HUVEC-laden bioink were loaded to separate

syringes and sequentially co-printed into a heterogeneous lattice construct (Figure 2-10A). For 3D bioprinting, duration of the time during which cells were encapsulated in the bioink at 8°C was around 30 minutes. The cold shock responses of mammalian cells generally involve suppression of transcription and subsequent translation, modulation of the cell cycle and reduction in metabolism. However, no significant responses of cells to cold stress were observed in our *in vitro* experiments, suggesting that the exposure to 8°C for this relatively short period of time had negligible effects on cells. All cells showed over 85 % of cell viability during the 7 days of culture (Figure 2-10B-D). In addition, the result of immunostaining analysis confirmed the expression of sarcomeric α-actinin by the CMs and CD31 by HUVECs on day 7 (Figure 2-10E). These results demonstrate that our printing approach supports cellular growth and proliferation without affecting the cells' phenotype.

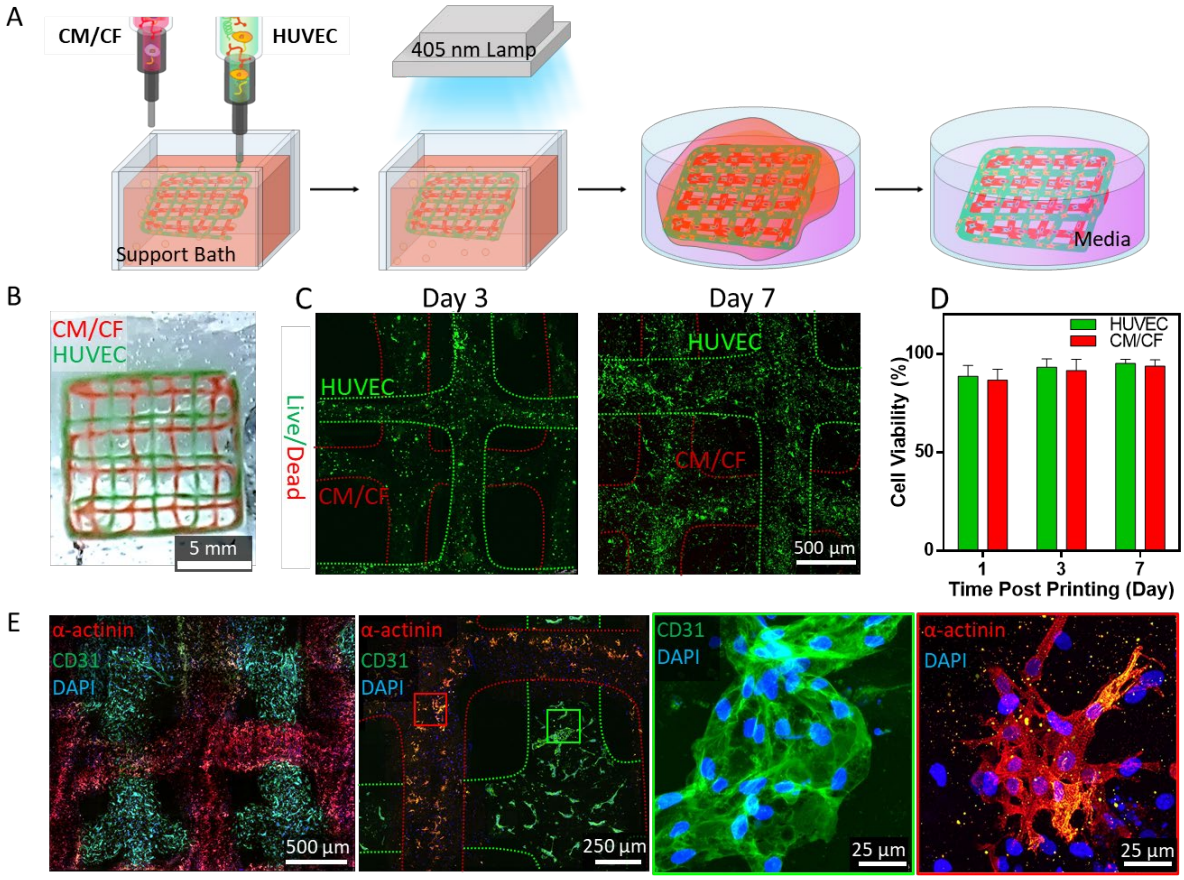

Figure 2-10. 3D bioprinting of cell-laden elastic constructs using MeTro/GelMA bioink. (A) A schematic illustration of 3D bioprinting of lattice scaffolds using HUVECs- and CMs/CFs-laden MeTro/GelMA bioinks. Green and red food colors were used to distinguish the HUVECs- and CMs/CFs-laden inks, respectively, only for imaging experiments. 3D bioprinting of lattice scaffolds containing HUVECs and CMs/CFs. (B) A representative camera image of the 3D printed lattice construct in the support bath. (C) Quantification of cell viability for 3D bioprinted cell-laden Metro/GelMA hydrogels at days 1, 3 and 7 post bioprinting. (D) Representative images of live/dead stained CMs/CFs and HUVECs incorporated within the construct at days 3 and 7 post bioprinting. (E) Immunostaining of the lattice structure against sarcomeric α-actinin (red), CD31

(green), and DAPI (blue) at day 7 post bioprinting. Printed CMs/CFs and HUVECs are marked with red and green boxes, respectively.

In human body, blood vessels have essential roles in constant nutrient-waste exchange between the blood and tissue as well as in homeostasis and regulation of the human body system. Likewise, 3D bioprinted tissue constructs require vascular systems in order to circumvent necrosis and mimic native tissue function. Connective tissues such as cartilage and bone have been successfully printed without vasculature,[67-68] however, the creation of human-sized soft tissues for clinical translation remains challenging due to slow vascularization rate in tissue constructs. One solution for this challenge is to create vascular channel within artificial tissues to speed up the vascularization process when implanted *in vivo*,[43-44] which requires higher standards on printing speed, accuracy, processability and structural heterogeneity compared to printing simple structure like lattice. Therefore, in our second *in vitro* model, we aimed to use our elastin-based bioink to print a vascularized cardiac tissue as a proof of concept.

To this end, two bioinks were prepared to engineer a vascularized cardiac tissue model (Figure 2-14A): i) GelMA bioink loaded with CFs/CMs and HUVECs to represent parenchymal cardiac tissue; ii) MeTro/GelMA bioink loaded with HUVECs for vessel formation. Prior to 3D bioprinting, rheological properties and printing conditions for GelMA bioink were optimized using a similar method as described for MeTro/GelMA bioink (Figure 2-11).

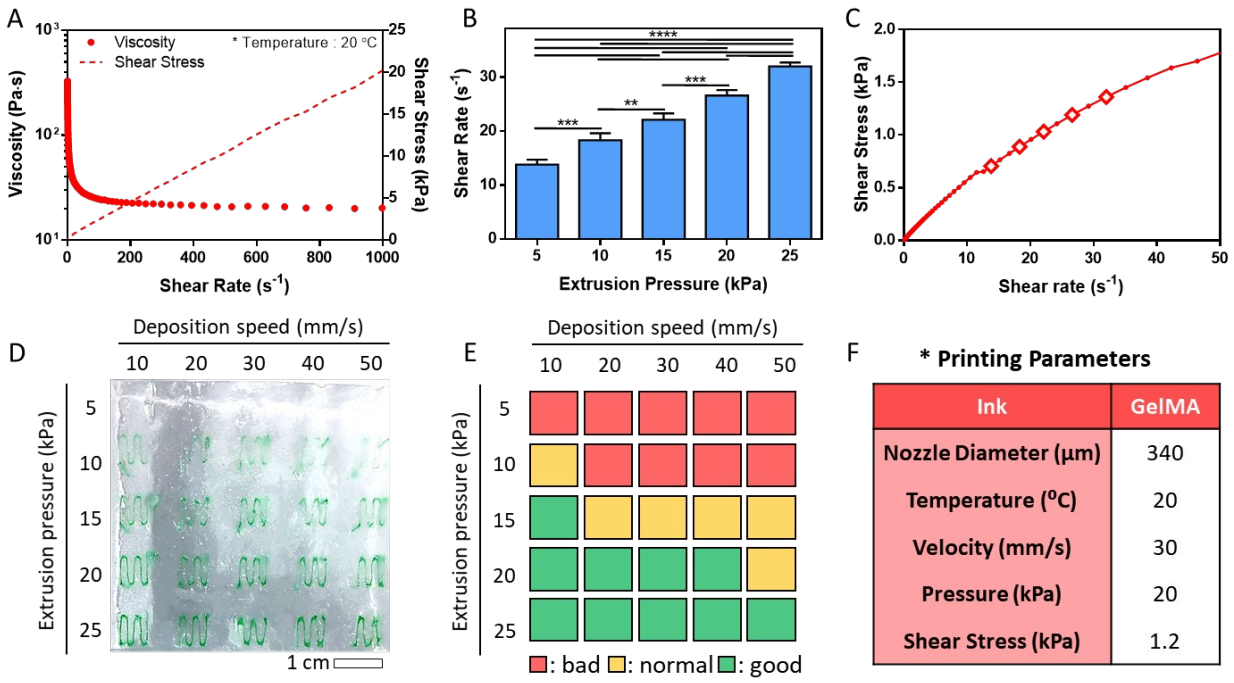

Figure 2-11. Rheological properties of GelMA bioink. (A) Viscosity and shear stress of GelMA bioink as a function of shear rate. (B) Varied shear rates of GelMA bioink depending on extrusion pressure. (C) Shear stress of GelMA bioink measured as a function of shear rate. The diamond points indicate the actual shear stresses on the cells encapsulated in the bioink exiting the nozzle under the extrusion pressures 5, 10, 15, 20, and 25 kPa, respectively (from left to right). (* $p<0.05$, ** $p<0.01$, *** $p<0.001$, **** $p<0.0001$) (D) GelMA bioink filaments embedded into support bath with different printing pressures and speed. (E) Evaluation of printability of GelMA bioink with different printing pressures and speeds. (F) Optimized printing conditions for GelMA bioink.

In the degradation study, 3D printed GelMA constructs showed faster degradation rate than MeTro/GelMA constructs due to the high MMP-sensitivity of GelMA (Figure 2-12).

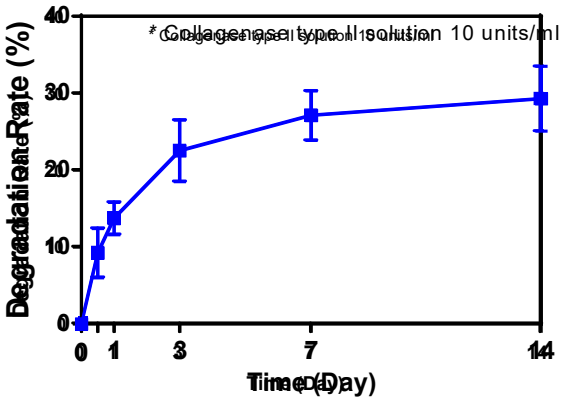

Figure 2-12. Degradation rate of lattice constructs printed with GelMA bioink at days 0.5, 1, 3, 7 and 14 post incubation in collagenase solution.

Our cardiac tissue model was composed of 67 layers with 7.2 mm in length and width, and 16.5 mm in height (Figure 2-13). The bioprinting process took around 11 min and the bioprinted structure was photocrosslinked upon exposure to visible light for 3 min (Figure 2-14D).

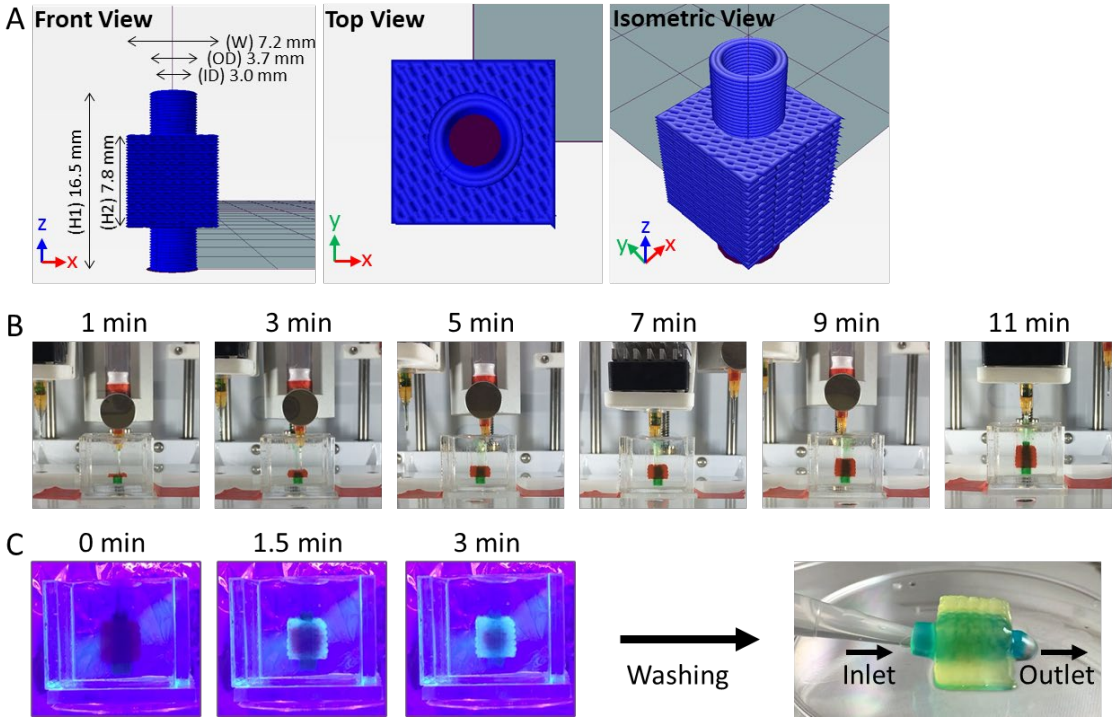

Figure 2-13. Representative images of 3D printed vascularized cardiac tissue model. (A) Schematic of the printed tissue model in different angles. (B) The process for 3D printing of the vascularized cardiac tissue construct. (C) Photocrosslinking of the printed construct with a 405 nm LED lamp. The printed structure was perfusable after washing step.

For the *in vitro* analysis, the printed constructs were sectioned into 3 mm slices with a razor blade. The viabilities of CFs/CMs and HUVECs in the printed structure were above 85% up to 15 days of culture (Figure 2-14B, C). In addition, the printed cardiac tissue constructs demonstrated high retention of cells' phenotype as confirmed by immunofluorescent staining for sarcomeric α-actinin, CD31 and DAPI at day 10 (Figure 2-14E). The endothelial cells proliferated in both GelMA and MeTro/GelMA hydrogels, as confirmed by CD31 expression throughout the whole constructs. Also, we observed that the CMs were elongated and branched in every direction to connect to each other.

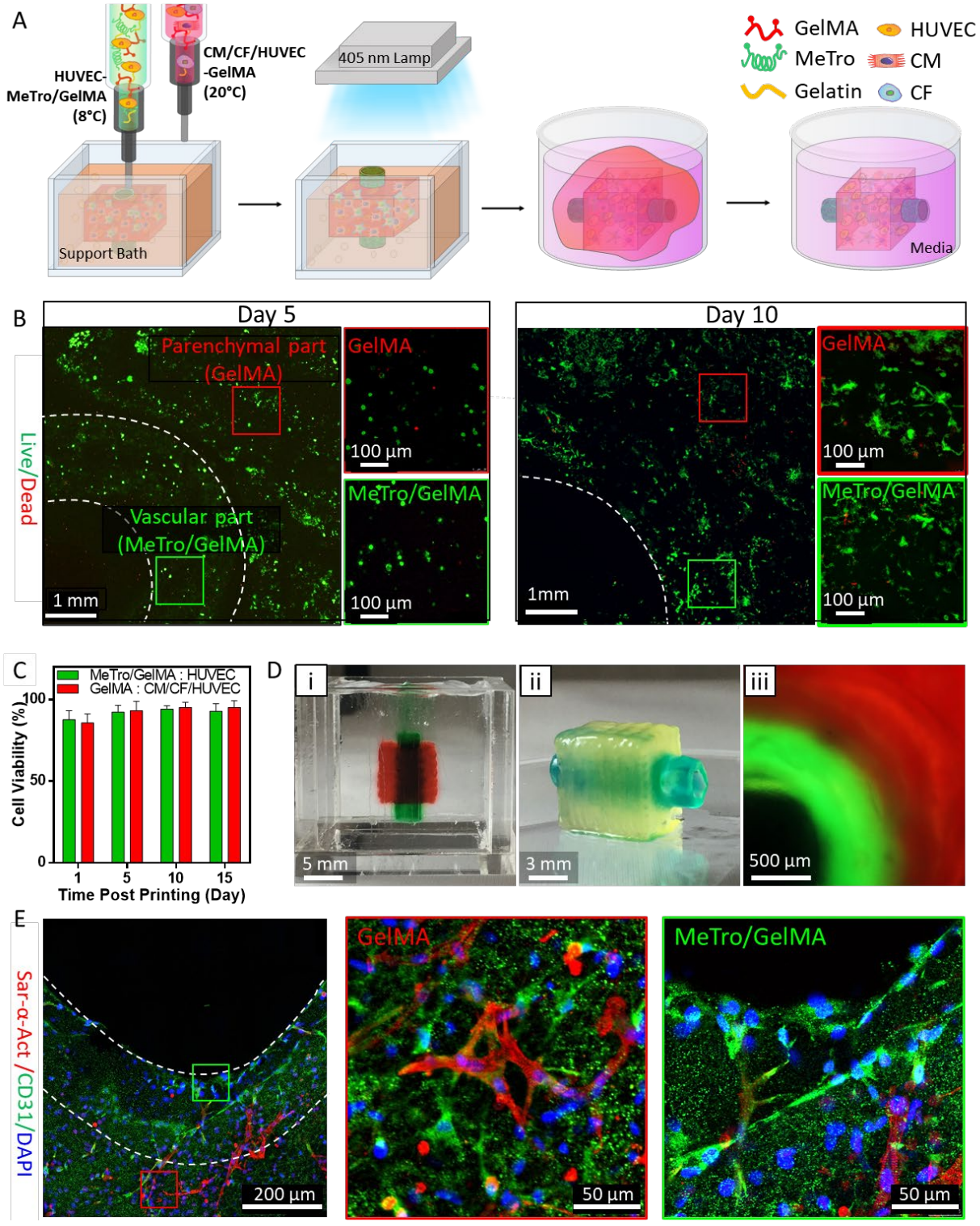

Figure 2-14. 3D bioprinting of cell-laden elastic constructs using MeTro/GelMA bioink. (A) A schematic to describe 3D bioprinting vascularized cardiac constructs with HUVECs-laden

MeTro/GelMA bioink and CMs/CFs/HUVECs-laden GelMA bioink. (B) Representative images of live/dead stained CMs, CFs and HUVECs incorporated within the bioprinted structure at days 5 and 10 post bioprinting. Parenchymal tissue printed with GelMA bioink and vasculature printed with MeTro/GelMA bioink are marked with red and green boxes, respectively. (C) Viability of HUVECs (in MeTro/GelMA bioink) and CMs/CFs/HUVECs (in GelMA bioink) within vascularized cardiac tissue constructs. (D) A vascularized cardiac construct in the support bath right after printing process (i) and the construct after the photocrosslinking and washing steps (ii). Green and red food colors were used to distinguish the MeTro/GelMA and GelMA bioinks, respectively, only for imaging experiments. (iii) A cross-sectional fluorescence image of the vascularized cardiac construct. Fluorescein and rhodamine dyes were added to the MeTro/GelMA and GelMA bioinks, respectively. (E) Immunostaining of the vascularized cardiac construct against sarcomeric α-actinin (red), CD31 (green), and DAPI (blue) at day 10 post bioprinting. HUVECs (in MeTro/GelMA bioink) and CMs/CFs/HUVECs (in GelMA bioink) are marked with green and red boxes, respectively.

The layer of endothelial cells in human blood vessel is essential to form a semi-permeable barrier that regulates the transport of water, proteins and blood cells between the blood and interstitial fluids, which is important for normal blood vessel function.[69] In our study, to quantify the barrier properties imparted by HUVECs in vascular construct, we measured the diffusional permeability of fluorescein isothiocyanate-conjugated dextran (FITC-Dex). The results revealed that compared to the acellular construct ($1.4 \pm 0.4 \times 10^{-3}$ cm/s), the HUVECs-laden structure ($0.8 \pm 0.3 \times 10^{-3}$ cm/s) showed a 2-fold reduction in diffusional permeability, confirming the barrier function of the endothelium (Figure 2-14A-C).

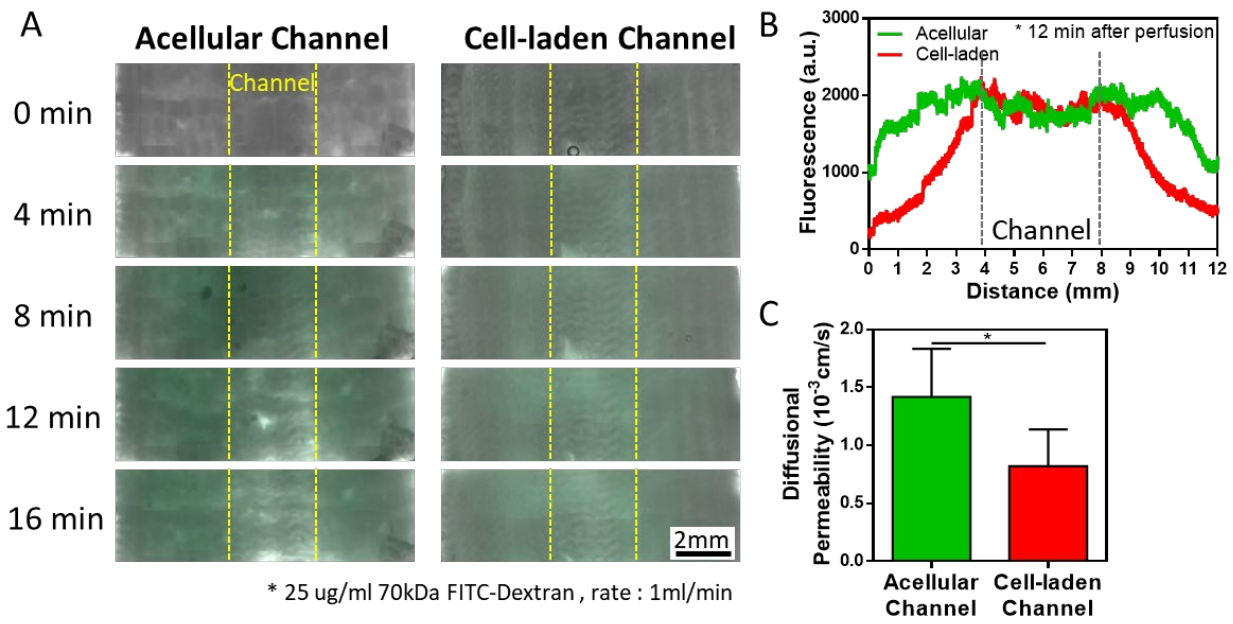

Figure 2-14. Evaluation of endothelium barrier function of 3D bioprinted constructs. (A) Microscope images showing FITC-Dextran distribution within the constructs with acellular and HUVECs-laden channel 0, 4, 8, 12 and 16 min after infusion of FITC-Dex to quantify the barrier properties imparted by HUVECs in vascularized cardiac construct. (B) FITC-Dex distribution within the constructs plotted as a function of distance from vasculature. (C) Diffusional permeability of FITC-Dex in acellular and HUVECs-laden channels.

Cardiac excitation-contraction coupling (EC coupling) describes a series of events from the production of an electrical impulse to the contraction of muscles in the heart.[70] In a native heart tissue, when more than two independently beating cardiomyocytes are joined, the cell with the highest inherent rate sets the pace. Cardiomyocytes are interconnected with gap junctions and the electrical impulses to stimulate contractions spread from the fastest one to the rest, resulting in synchronized beating. In this study, we evaluated EC coupling of the 3D bioprinted cardiac tissue

constructs via video microscopy and a custom algorithm to quantify beat frequency and degree of coordination as previously described.[58] Beating cardiac cells were identified within 3D constructs based upon inclusion criteria (i.e., signal-to-noise ratio, peak-to-peak frequency) and the dynamic beating behavior of individual cells was quantitatively analyzed (Figure 2-15A-C). The contracting CMs were first noticed at day 5 post bioprinting. During the 15 days of culture, the contractions became more synchronous with increased interconnection between striated muscles, as confirmed by immunofluorescent staining of sarcomeric α actinin-positive myofibrils. The beating rate and the coordination reached 42.0 ± 3.1 bpm and 73.1 ± 3.2 % at day 15 (The degree of coordination for native heart is considered 100 %) (Figure 2-15D, E). This result implies that the cells were tightly interconnected through gap junctions, which contributed to the rapid transmission of the electric impulse between cells and enabled the synchronized contraction.

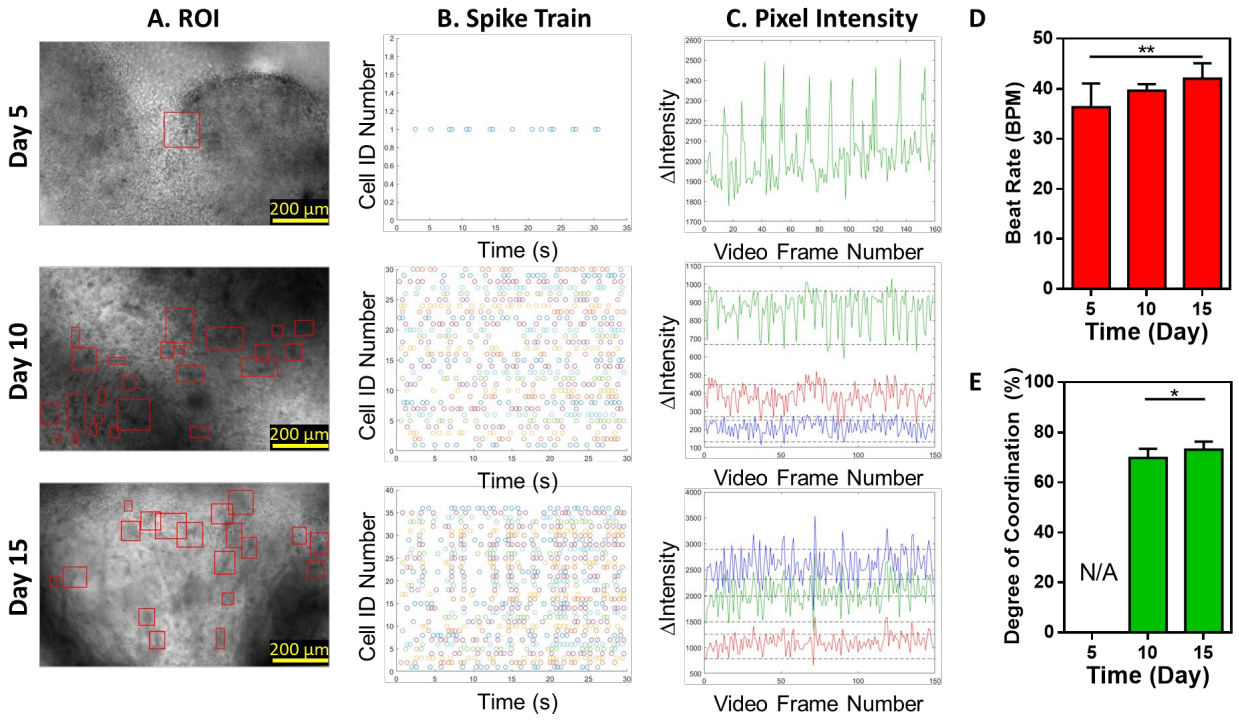

Figure 2-15. Evaluation of synchronized cardiac beating of 3D bioprinted constructs. (A)

Microscope bright field images with automated identification of encapsulated cells at day 5, 10 and 15 post bioprinting. Beating CMs were identified and marked with red boxes as region of interests (ROIs). (B) Representative spike train analogs used to quantify the degree of coordinated contractions of cardiac cells encapsulated in 3D bioprinted constructs at day 5, 10 and 15 post bioprinting. (C) Representative plots showing the change in pixel intensity over time for cardiac cells encapsulated in 3D bioprinted constructs at day 5, 10 and 15 post bioprinting. (D) Beat rate and (E) degree of coordination measured for the beating CMs.

To assess *in vivo* degradation and biocompatibility of our bioink, the acellular constructs that were 3D printed with MeTro/GelMA and GelMA bioinks were subcutaneously implanted in rats (Figure 2-16A). The samples were explanted on days 7, 14, and 21 in order to obtain the degradation rate and perform histological examination. The average biodegradation of the implanted samples increased from 15.8 ± 8.1 % at day 7 to 67.4 ± 11.9 % at day 21 post-implantation (Figure 2-16B). Similarly, the hematoxylin and eosin (H&E) staining of the samples revealed effective biodegradation and significant integration between engineered constructs and surrounding tissue (Figure 2-16C). This result suggests that the bioink can be potentially used for repair and replacement of the damaged or diseased soft tissues due to fast degradation and bio-integration. A fibrous capsule was observed around the explanted samples at day 7 but disappeared after 14 and 21 days, indicating minimal inflammatory response after implantation of the constructs (Figure 2-16D). In addition, the immunohistochemical (IHC) staining for macrophages (CD68) and T-lymphocytes (CD3) was performed on the cryo-sectioned samples and analyzed both qualitatively and quantitatively to evaluate biocompatibility of the constructs (Figure 2-16E-G). The results showed infiltration of CD3 and CD68 antigens on day 7 due to natural foreign body response.

However, this response was not observed after 21 days, showing significant reduction of both markers, which proves high biocompatibility of the printed constructs. Similar to H&E stain results, a significant cell infiltration was observed on day 21 post implantation, confirming the construct was well-integrated with the host tissue.

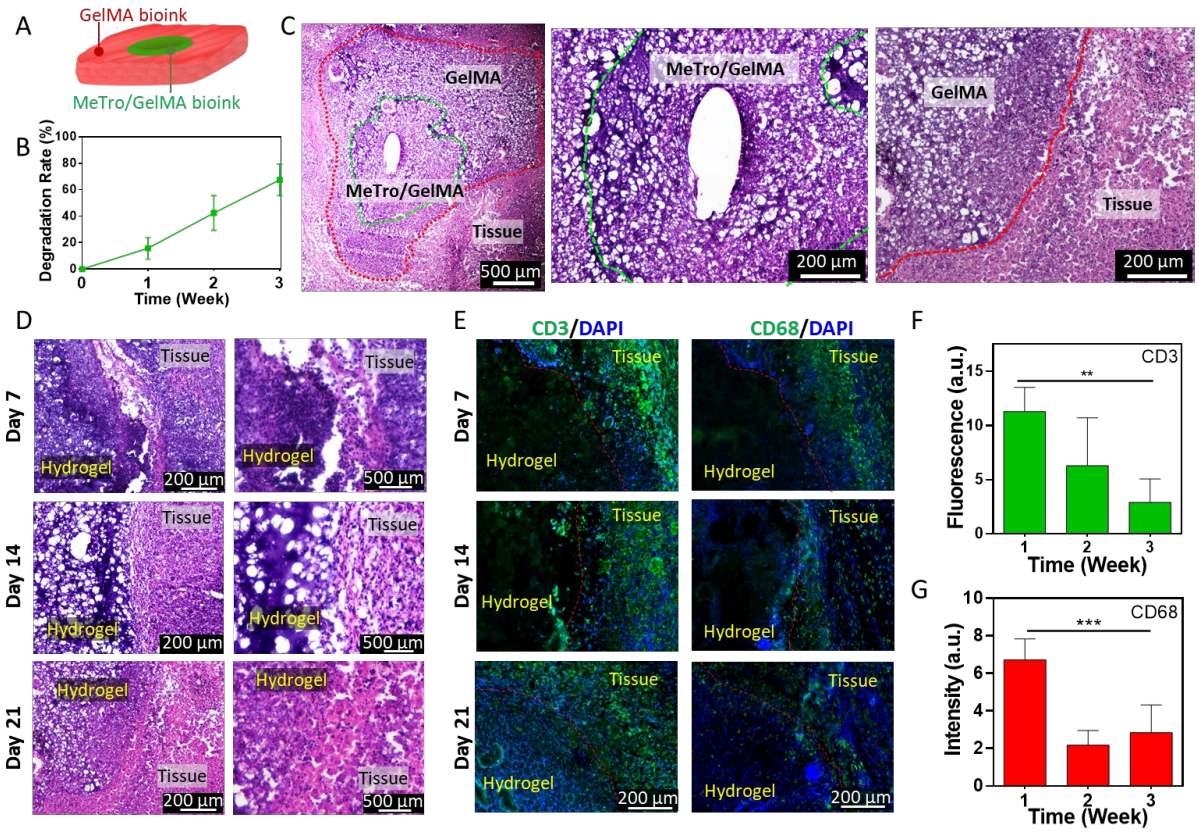

Figure 2-16. *In vivo* biocompatibility of the 3D printed vascularized cardiac constructs. (A) A schematic of the 3D printed implant structure. (B) *In vivo* biodegradation rate of the 3D printed constructs. (C) H&E staining of the 3D printed constructs explanted at day 21 post implantation. (D) H&E staining images showing the interface between implanted hydrogel constructs and tissues at day 7, 14 and 21 post implantation at 10 × (left) and 40 × (right) magnifications. (E) IHC staining against CD3, (left, green) and CD68 markers (right, green) and DAPI (blue) in the explanted 3D printed constructs at day 7, 14 and 21 post implantation. (F, G) Inflammatory response was

quantified by calculating fluorescence intensity of CD3 and CD68 markers from IHC images. (* $p<0.05$, ** $p<0.01$, *** $p<0.001$)

2.3. Conclusion

In this work, we demonstrate, for the first time, the use of recombinant human tropoelastin combined with gelatin as an elastic bioink for 3D bioprinting. The synergistic association of two biopolymers allowed a high-resolution printing with great cell viability. As a proof of concept to fabricate an entirely 3D-printed artificial tissue, vascularized cardiac tissue constructs were 3D printed and characterized both *in vitro* and *in vivo*. The printed constructs presented endothelium barrier function and spontaneous beating of cardiac cells which are important functions of cardiac tissue *in vivo*. Furthermore, the printed construct elicited minimal inflammatory responses, and were shown to be efficiently biodegraded *in vivo* when implanted subcutaneously in rats. Taken together, our results demonstrate the potential of MeTro/GelMA bioinks for printing complex 3D functional cardiac tissues which could eventually be used for cardiac replacement.

3D printing holds great promise for engineering whole organs, but there are still challenges remaining. These include the needs for a physiologically relevant number of cells and scalable approaches to print complex human-scale tissues with hierarchical vascular network. The vascularized cardiac construct presented in this work has proven that we can fabricate small-scaled constructs that recapitulate the architectural and functional properties of native tissues. For clinical translation, therapeutic value of cell-laden cardiac tissue should be evaluated by using a relevant animal model (e.g. myocardial infarction model). We envision that integrating our approach with modular tissue design will enable fabricating a complex multifunctional tissue at a clinically relevant scale.

2.4. Materials and Methods

Synthesis of gelatin methacryloyl (GelMA)

GelMA was synthesized as previously described elsewhere.[48, 71] Briefly, 10 g gelatin derived from cold-water fish skin (Sigma-Aldrich) was dissolved in 100 ml Dulbecco's phosphate buffered saline (DPBS) and heated to 60 °C for 30 min. Next, 8 ml methacrylic anhydride (Sigma-Aldrich) was added gently and dropwise to the gelatin solution under vigorous stirring (300 rpm) at the same temperature. The reaction was stopped after 3 hours by adding 300 ml DPBS and dialyzed in dialysis tubing (Spectrum Laboratories, MWCO = 12-14 kDa) against deionized (DI) water at 50 °C for 5 days to remove any unreacted methacrylic anhydride. After sterile filtration, the solutions were subsequently lyophilized for 4 days to generate a fibrous white foam.

Synthesis of methacryloyl substituted tropoelastin (MeTro)

Tropoelastin was expressed in bacteria and purified essentially as described previously.[72] Methacrylated tropoelastin (MeTro) was synthesized as previously described elsewhere.[73] Briefly, 2 g tropoelastin (Synthetic Human Elastin without domain 26A, recombinant human tropoelastin isoform SHELdelta26A) was dissolved in 20 ml DPBS at 4 °C to reach a 10% (w/v) tropoelastin solution. Once completely dissolved, 3 ml methacrylic anhydride was added dropwise to the solution and allowed to homogenize at 4 °C. The reaction was stopped after 16 hours by adding 20 mL DPBS (pre-cooled at 4 °C) to the solution. This solution was then dialyzed against DI water at 4 °C in a dialysis cassette (Slide-A-Lyzer™, MWCO = 3.5 kDa) for 3 days. After dialysis, MeTro was lyophilized for 4 days.

Hydrogel preparation

To form MeTro/GelMA hydrogels, different concentrations of MeTro (0, 7.5 and 15 % (w/v)) and GelMA (0, 7.5 and 15 % (w/v)) were dissolved in DPBS with 0.4 % (w/v) Lithium phenyl-2,4,6-trimethylbenzoylphosphinate (LAP) as a photoinitiator at 4 °C. The precursor solutions were then placed in polydimethylsiloxane (PDMS) molds and photocrosslinked using a LED light (405 nm, 10 W) for 120 sec.

Bioink preparation

Gelatin from cold water fish skin (Sigma-Aldrich) were used to enhance the printability of the both MeTro/GelMA and GelMA bioinks. After evaluating the extrudability and the cell viability, the final concentrations of gelatin were determined for each bioinks. For MeTro/GelMA bioinks, 7.5 % (w/v) of MeTro, 7.5 % (w/v) of GelMA, 20 % (w/v) gelatin and 0.4 % (w/v) LAP were dissolved in cell culture media at around 10 °C and the pH was adjusted to 7. For GelMA bioinks, 10 % (w/v) of GelMA, 23 % (w/v) gelatin and 0.4 % (w/v) LAP were dissolved in cell culture media and the pH was adjusted to 7.

To make cell-laden bioinks, each step was carefully conducted under sterile conditions and appropriate number of cells were mixed with the solutions at the last step. The lattice structures were printed with MeTro/GelMA bioink with 2×10^7 cells/ml of HUVECs and MeTro/GelMA bioink with 2×10^7 cells/ml of CMs and 1×10^7 cells/ml of CFs. For the vascularized cardiac constructs, MeTro/GelMA bioink with 2×10^7 cells/ml of HUVECs and GelMA bioink with 2×10^7 cells/ml of CMs, 1×10^7 cells/ml of CFs and 5×10^6 cells/ml of HUVECs were used.

Proton nuclear magnetic resonance (^{1}H NMR) characterization

Spectra were acquired with Bruker AV400 NMR spectrometer for uncrosslinked GelMA and MeTro dissolved in deuterated dimethyl sulfoxide (DMSO-d6) and the supernatant from a partially dissolved composite (50/50 GelMA/MeTro, 15% (w/v) total polymer concentration) kept under vigorous shaking in DMSO-d6 overnight at room temperature. The degree of methacryloyl groups consumption was calculated by the following equation, where PA_b is equal to the peak area before crosslinking, and PA_a is the peak area after crosslinking (n = 3):

$$\text{Degree of methacryloyl consumption}(\%) = \frac{(PA_b - PA_a)}{PA_b} \times 100\ \% \quad (1)$$

Peak areas were measured using TopSpin 3.5pl4 to integrate the area of the curve with respect to phenolic conjugated peaks at d = 6.5–7.5 ppm.

Mechanical characterization

Hydrogel samples were prepared in rectangular PDMS molds (12 mm length, 6 mm width, 1.5 mm height) for tensile test or in cylindrical molds (6 mm diameter, 3 mm height) for compression test as described before. The dimensions of the hydrogels were then measured using a caliper. An Instron 5542 mechanical tester was used to perform tensile and cyclic compression tests. For the tensile test, hydrogels were placed between two pieces of tape within tension grips and extended at 1 mm/min until failure. The tensile strain and stress placed on the hydrogel samples were recorded through the Bluehill 3 software during the test and the compressive moduli of the hydrogels were calculated from the slope of the stress-strain curves. For the compression tests, hydrogels were loaded between compression plates. Cyclic compression tests were performed at 50% strain level and a rate of 1 mm/min by performing 10 cycles of loading and unloading. The

compressive strain and stress on the samples were measured using the Bluehill 3 software and the compressive moduli were obtained from the linear region (0.15-0.25 mm/mm strain) in the stress-strain curve. Energy loss were determined based on the area between the loading and unloading curves for cycle 8. (n = 4)

$$\text{Energy Loss (\%)} = \frac{\text{Area below loading curve} - \text{Area below unloading curve}}{\text{Area below loading curve}} \times 100\ \% \quad (2)$$

Preparation of Carbopol support bath

The Carbopol gel was prepared as described earlier with some modification.[74] Briefly, 1.8% (w/v) of Carbopol ETD 2020 (Lubrizol) was dissolved in 50 mL of Dulbecco's modified eagle medium (DMEM, Gibco) and vortexed. 1.1 mL of 10 M NaOH was added to 50 mL Carbopol solution and followed by vortexing until it became a gel. Next, the Carbopol gel was centrifuged at 1000 × g for 1 hour until the gel became homogeneously dispersed. The Carbopol gel were manually stirred with spatula once or twice during the centrifugation to facilitate the mixing process. The homogeneous Carbopol gel was kept in a 4 °C fridge for storage.

Rheological properties: A rheometer (MCR 92, Anton Paar) equipped with a parallel plate with a gap size of 1 mm and a diameter of 8 mm was used to characterize the rheological properties different solutions including MeTro/GelMA pre-polymers, gelatin solution, MeTro/GelMA bioinks and GelMA bioinks. Viscosity and dynamic modulus of the solutions were determined as a function of temperature. Viscosity and shear stress of both bioinks were measured as a function of shear rate from 0.1 to 1000 s^{-1}. The shear force applied to cells during bioprinting was measured indirectly by calculating the shear rate during printing and matching it to shear stress-shear rate

data. More details on rheological properties are outlined in Methods Section, Supporting Information.

Rheological characterization

A rheometer (MCR 92, Anton Paar) equipped with a parallel plate with a gap size of 1 mm and a diameter of 8 mm was used to characterize the rheological properties of different solutions including MeTro/GelMA pre-polymers, gelatin solution, MeTro/GelMA bioinks and GelMA bioinks. Different solutions were prepared as outlined before and pipetted onto the rheometer. Any excess solution was trimmed with a spatula before these measurements.

Viscosity of MeTro/GelMA pre-polymers, gelatin solution and MeTro/GelMA bioinks were measured as a function of temperature. Shear rate was constant at 50 s^{-1} and the temperature was swept at the rate of 2 ºC min^{-1}. To demonstrate the shear thinning behavior of the MeTro/GelMA bioinks, viscosity was measured as a function of temperature under three different shear rates of 5, 50 and 500 s^{-1}.

In a temperature sweep test, the storage modulus and the loss modulus were recorded as a function of temperature under a constant shear rate of 50 s^{-1}.

For a shear rate sweep test, viscosity and shear stress of bioinks were measured while shear rate was swept from 0.1 to 1000 s^{-1}. During the test, temperature for the GelMA bioinks and the MeTro/GelMA bioinks were set at 20 °C and 8 °C respectively.

The actual shear force applied on cells during the bioprinting was measured indirectly. Briefly, time spent for 1 ml bioink extrusion, T, was recorded and put into the equation below, where $\dot{\gamma}$ is

shear rate (s^{-1}); V is volume of the extruded bioink (1 ml); d is diameter of printing nozzle (0.34 mm); T is time of extrusion (second).:

$$\dot{\gamma} = \frac{8V}{\pi d^3 T} \quad (3)$$

Then, the shear stress on cells according to the calculated shear rate was obtained from shear stress-shear rate data.

3D printing of bioinks

Acellular and cell-laden bioinks were prepared as outlined before and were loaded into a 3 mL syringe affixed to a 25-gauge blunt end needle. Support baths were prepared as described and poured into a container large enough to hold the structure to be 3D printed. The syringe was loaded onto an INKREDIBLE+ bioprinter printhead from Cellink® and MeTro/GelMA bioink was maintained at 10 ºC. Pressure was varied to change the flow rate (10-25 kPa) of the bioinks and printed into different structures with a layer height of 250 µm with custom G-code. The printed structures were then exposed to light (405 nm) to crosslink up to 3 min depending on the shape and the size of the structures, carefully removed from the support bath with a spatula, washed with warm DPBS.

For 3D bioprinting, cells were mixed with the bioink before loading onto the bioprinter and the printed structures were further washed with media to facilitate the removal of Carbopol bath around constructs before they were immersed in media and kept in CO_2 incubators. The media was changed once in the first 30 min to remove unreacted photoinitiator, gelatin and remaining Carbopol gel and then changed every day.

Enzymatic degradation

MeTro/GelMA lattice (8 mm L × 8 mm W × 1 mm H) were printed as described previously. The printed constructs were incubated in DPBS at 37 °C in order to remove the residual gelatin and Carbopol in the printed constructs for 3 days. The DPBS solution was refreshed on a daily basis. The dry weights of the samples were measured after freeze-drying. The samples were immersed in 1 mL of DPBS containing 10 units/mL of collagenase II (Worthington Biochemical, Lakewood, NJ, USA) and incubated at 37 °C. Samples were removed from the collagenase solution, lyophilized and weighed at different time points (days 0.5, 1, 3, 7 and 14). The degradation rate was calculated following the equation, where W_d is the weight of dried samples after degradation and W_0 is the initial weight of dried samples before swelling (n = 4):

$$Degradation\ Rate\ (\%) = \frac{W_0 - W_d}{W_0} \quad (4)$$

Cell culture and isolation

Human umbilical vein endothelial cells (HUVECs) were obtained from Lonza and cultured in endothelial growth BulletKit (EGM-2, Lonza) at 37°C in a humidified atmosphere containing 5 % CO_2. The 6–12th passages of HUVECs were used in this study. Neonatal ventricular rat cardiomyocytes and cardiac fibroblasts were isolated at the UCLA NRVM core facility using 2- to 4-days old rats. Myocytes and fibroblasts were separated using Percoll density gradient. NRVMs were used on the same day that they were provide and NRVFs were cultured under standard conditions (37 °C, 5% CO_2) in DMEM with 10% fetal bovine serum and 1% penicillin/streptomycin before they were used at passage 1-3.

Determination of cell viability

The viability of bioprinted neonatal cardiac cells and HUVECs was evaluated by LIVE/DEAD™ Viability/Cytotoxicity Kit (Invitrogen) at days 1, 3, 5, 7 and 15. Ethidium homodimer (EthD-1) and calcein AM were diluted into 50:1 and 200:1 with DPBS respectively. Depending on the structure, appropriate amount of the solution was assigned to 3D bioprinted constructs and incubated for 45 min in 5% CO_2 at 37 °C. Live and dead cells were observed by a fluorescence optical microscope (Primovert, Zeiss) or a confocal fluorescence microscope (SP8-STED, Leica). Living cells were detected by calcein AM (green fluorescence), and death cells by EthD-1 (red fluorescence). The number of viable cells was quantified using ImageJ (NIH) software. The number of cells was calculated by the ratio among the area of each cluster with the area of a known single cell. Then, the viability rate was obtained by comparing the number of viable cells with total number of viable and non-viable cells.

Immunofluorescence staining

Cell-laden structures were cultured under standard condition as described before. At different time points (days 5 and 10), samples were fixed for 1 h at room temperature using 4 % (v/v) paraformaldehyde (Sigma-Aldrich) in DPBS. Cells were permeabilized by soaking the samples in 0.1 % (v/v) Triton X-100 (Sigma-Aldrich) dissolved in DPBS for 30 min while non-specific binding was inhibited using 10 % (v/v) bovine serum albumin (BSA, Sigma-Aldrich) for 1 h at room temperature. Samples were then incubated for overnight at 4 °C in a solution containing primary antibodies at 1:200 dilution in 10 % (v/v) BSA and 0.1 % (v/v) Triton X-100 in DPBS. In particular, rabbit polyclonal anti-CD31 (ab28364, Abcam) and mouse monoclonal anti-sarcomeric

α-actinin (ab9465, Abcam) were used. Samples were then incubated for 1 hour at room temperature in a solution containing secondary antibodies at 1:400 dilution in 10 % (v/v) BSA in DPBS. Alexa 488-conjugated goat anti-mouse (ab150116, Abcam) and Alexa Fluor 594-conjugated goat anti-rabbit (a11008, Invitrogen) were acquired from Abcam and Invitrogen respectively. Nuclei of the cells were stained by 40,6-diamidino-2-phenylindole (DAPI, Invitrogen). Images were taken using a fluorescence optical microscope (Primovert, Zeiss) or a confocal fluorescence microscope (SP8-STED, Leica).

Evaluation of endothelium barrier function

To assess barrier function of the printed vasculature, diffusional permeability was quantified by perfusing culture media with 25 μg/mL FITC-conjugated 70-kDa dextran (FITC-Dex; Sigma product 46945) in the vascular channel at a rate of 1mL/min for 20 min. The diffusion of FITC-Dex was monitored using tile scan of a fluorescence microscope with 2.5× objective (Zeiss). Fluorescence images were captured before perfusion and every 4 min. Diffusional permeability of FITC-Dex is calculated by quantifying changes of fluorescence intensity over time using the following equation:

$$P_d = \frac{1}{I_1 - I_b} \cdot \left(\frac{I_2 - I_1}{t}\right) \cdot \frac{d}{4} \quad (5)$$

P_d is the diffusional permeability coefficient, I_1 is the average intensity at an initial time point, I_2 is an average intensity after time t (s), I_b is background intensity (before introducing FITC-Dex), and d is the channel diameter (cm). The measurements are performed on embedded channels with and without endothelium (n = 3).

Evaluation of cardiomyocyte beating

The beating behavior of the engineered cardiac tissues were assessed as previously described [75]. Briefly, individual CM contractions within the engineered cardiac tissues were quantified with a custom MATLAB code to calculate beats per minute (BPM) and degree of coordination using video microscopy. Cardiac cells were recorded at 30 frames per second and raw video files were exported as AVIs and imported into MATLAB for analysis. Regions of interest (ROIs) were identified from the first frame of the video recording as objects between 75 μm^2 – 1000 μm^2 in size. The average BPM was calculated as the mean number of contractions for all ROIs in field of view ($m > 20$) multiplied by 60 and divided by the video length from a minimum of three samples per condition ($n > 3$). Timestamps for each contraction from the identified CMs were assigned a unique identification number to gather a quantification on the degree of coordinated contraction in the tissue models.

Dorsal subcutaneous implantation of hydrogels

All animals were handled in strict accordance with good animal practice as defined in the federal regulations set forth in the Animal Welfare Act (AWA), the 1996 Guide for the Care and Use of Laboratory Animals, PHS Policy for the Humane Care and Use of Laboratory Animals, as well as UCLA's policies, and procedures as set forth in the UCLA Animal Care and Use Training Manual. All animal work was approved by the UCLA Chancellor's Animal Research Committee (ARC # 2018-076-01B).

3D printed cardiac tissue constructs (7.2 mm L × 7.2 mm W × 3 mm H) were used for this study to evaluate biodegradation and inflammatory response of the MeTro/GelMA and GelMA bioinks.

The 3D printed constructs were immersed in DPBS and incubated at 37 °C for 7 days to stabilize before implantation. Male Wistar rats (200−250 g) were purchased from Charles River Laboratories (Wilmington, MA, USA). 3D printed constructs were prepared under sterile conditions and their initial wet weights were recorded. General anesthesia and analgesia were induced by inhalation of isoflurane (2.5% (v/v)), followed by subcutaneous meloxicam administration (5 $mg \cdot kg^{-1}$). Next, 1.2 mm subcutaneous pockets were made through the posterior dorsal skin. The 3D printed constructs were then implanted into the subcutaneous pockets. The acellular tissue constructs were inserted into the left pocket and the right pocket respectively. Afterwards, the wounds were thoroughly closed with 3-0 polypropylene sutures. The tissue constructs were harvested at weeks 1, 2 and 3 post-implantations.

Histological and immunohistochemical analysis

Histological and immunohistochemical analysis were performed on cryosections of the explanted hydrogel samples in order to characterize the inflammatory response elicited by the implanted material. After explantation, samples were fixed in 4% paraformaldehyde for 4 hours, followed by overnight incubation in 30% sucrose at 4 °C. Samples were then embedded in Optimal Cutting Temperature compound (OCT) and flash frozen in liquid nitrogen. Frozen samples were then sectioned using a Leica Biosystems CM1900 Cryostat. 15-µm cryosections were obtained and mounted in positively charged slides. The slides were then processed for hematoxylin and eosin staining (Sigma) according to instructions from the manufacturer. The stained samples were preserved with DPX mountant medium (Sigma).

Immunohistofluorescent staining was performed on mounted cryosections as previously reported.[55] Anti-CD3 (ab16669) and anti-CD68 (ab125212) (Abcam) were used as primary

antibodies, and an Alexa Fluor 594-conjugated secondary antibody (Invitrogen) was used for detection. All sections were counterstained with DAPI (Invitrogen) and visualized on an AxioObserver Z7 inverted microscope.

Statistical analysis

All values are presented as mean ± standard deviation. Statistical differences between sample means at each condition were evaluated with two-way ANOVA tests using GraphPad (Software Inc., CA, USA) as P-values were defined as *< 0.05, **< 0.01, ***< 0.001, and ****< 0.0001.

Chapter 3 Scalable Fabrication of 3D Structured Microparticles with Spatially Functionalized with Biomolecules

3.1. Introduction

Microparticles with defined shapes and chemical modification promise to transform the way we interface with cells and tissues, acting as *in vitro* cell carriers that can tune biochemical and physical signals,[76] scaffolds to promote the growth and infiltration of cells *in vivo* to regenerate tissue,[18, 77] compartments for high-throughput single cell analysis,[78-79] and solid phases for barcoded molecular assays.[80-81] Numerous approaches to manufacture shaped hydrogel particles have been developed including wafer scale photolithography,[82] microfluidic emulsion polymerization, and continuous and stop-flow lithographic methods.[83-84] These conventional methods have had trade-offs between the throughput of manufacture and precision of particle shape and chemical functionalization.

Droplet microfluidics, where single, double, or aqueous two-phase emulsions have been employed to generate shaped microparticles,[85-86] has emerged as a powerful platform to produce uniform microparticles with different functions and properties. In particular, crescent-shaped microparticles[79] or hollow shell particles[87] produced by polymerizing precursors following aqueous two-phase separation (ATPS), possess a sub-nanoliter size cavity which can hold cells, and can template water in oil emulsions for performing single-cell and digital molecular assays. The current approach to manufacture these shaped particles, such as “nanovials”, requires precise injection of multiple polymer precursors into flow focusing microfluidic geometries, limiting scalability. Further, these previous approaches lacked robust approaches to spatially pattern different chemical functionalities, limiting the flexibility of the platform. For example, by locally

patterning cell adhesive proteins to the cavity region of the nanovials, cells can be preferentially bound within the nanovials, protecting them from shear stress during more vigorous handling steps such as emulsification, fluorescent activated cell sorting (FACS), or delivery *in vivo* into tissue for therapeutic applications. Additionally, selective adhesion can direct loading to an adhesive region or cavity sized to the dimensions of a single cell,[88-90] improving loading statistics beyond random Poisson processes. While more scalable manufacturing devices such as parallelized step emulsifiers and highly parallelized flow focusing devices have been used to dramatically enhance the production rate of spherical microparticles,[18, 91-93] high-throughput production of shaped 3D-particles or capsules which require two phases has not been achieved.

In this study, we use a induced-phase separation concept to overcome tradeoffs between particle complexity and fabrication throughput for the manufacture of microparticles with tunable localized surface chemistry and shape. We fabricate monodisperse 3D-axisymmetric particles with a chemically-functionalized cavity using a parallelized step emulsification device and temperature-induced phase separation. Harnessing the conditional phase separation of polyethylene glycol (PEG) and gelatin, photocrosslinkable PEG and gelatin ATPS droplets were generated and crosslinked with UV light to form uniform 3D axisymmetric particles with geometries dictated by the balance of interfacial tensions between the different phases (Figure 3-1).

The engineered particles were found to be selectively functionalized on their inner cavities with higher densities of gelatin, which we showed was beneficial for their application as a platform for cell-carriers and reaction vessels to perform single-cell assays. The embedded gelatin promoted deterministic attachment of cells only within the cavities *via* integrin binding. The diameter and the opening of the crescent particles were also controlled to efficiently encapsulate single cells within nanovials, improving upon previous stochastic loading limitations governed by Poisson

statistics. Cells adhered to nanovials could be sorted using standard FACS and viability was increased for cells attached to nanovials compared to unbound cells, suggesting these nanovials provide protection from fluid shear stresses during the sorting process. Finally, we showed the localized gelatin, when functionalized with capture antibodies, could be used to locally enrich secreted products from captured cells.

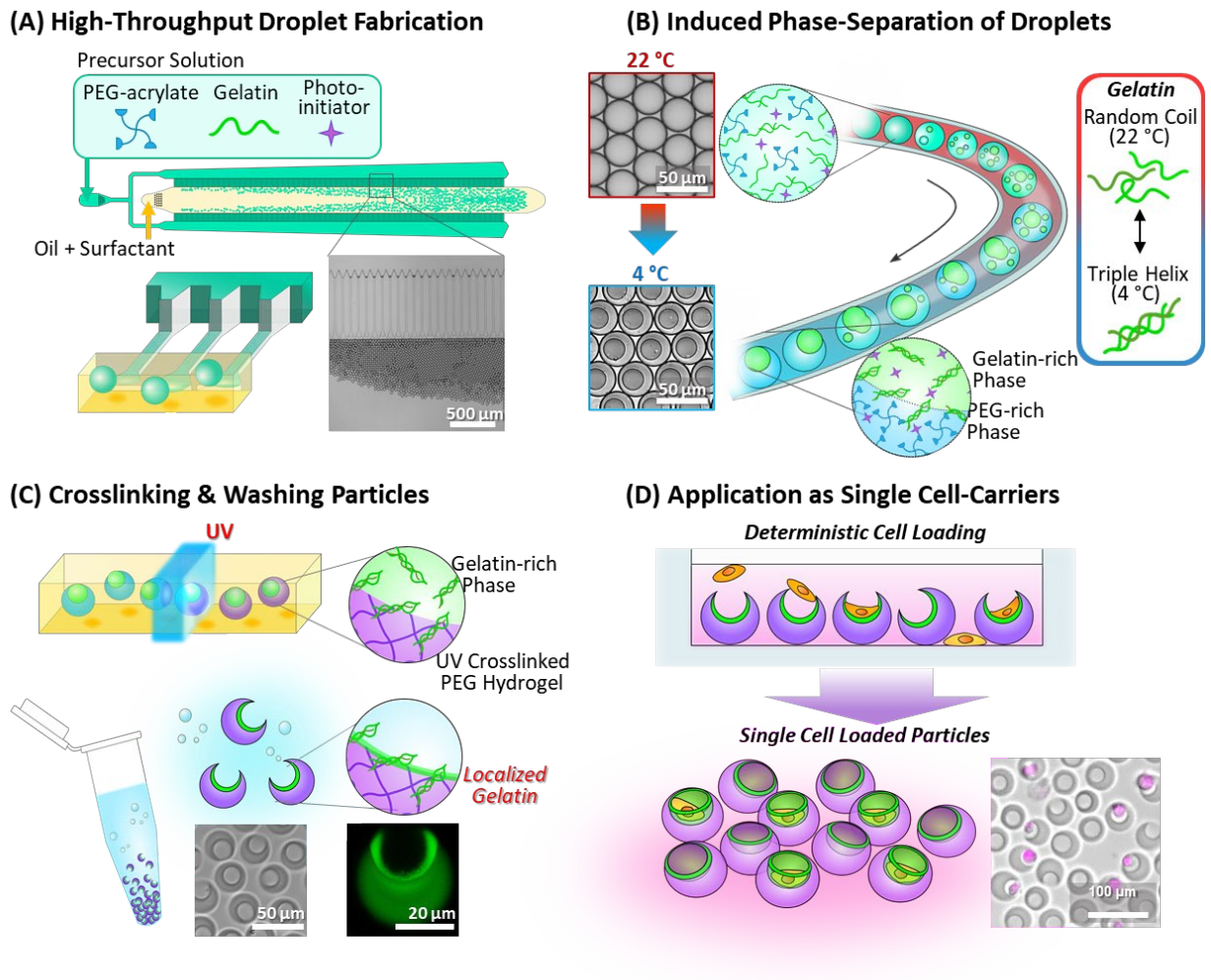

Figure 3-1. Overview of 3D structured microparticle fabrication using induced phase separation and their use. (A) Polymer precursors containing a mixture of PEG-acrylate, gelatin, and photo-initiator are injected into a high-throughput microfluidic droplet generator to create a

uniform two-phase water in oil emulsion. (B) By reducing the temperature of the emulsions, PEG and gelatin undergo phase separation to create a three-phase PEG/gelatin/oil system. (C) The emulsion is exposed to UV light to selectively crosslink the PEG-rich phase and washed to recover 3D structure particles with gelatin remaining localized on the cavity surface. (D) The structured particles with localized surface chemistries act as cell carriers that protect cells from shear stress and show enhanced performance for single cell loading, secretion capture and live cell sorting using FACS.

3.2. Results and Discussion

While PEG and dextran have been commonly used as two components of an ATPS in droplets,[79, 94-95] in this study, gelatin, instead of dextran, was used to enable us to trigger phase separation following massively parallel step emulsification using a temperature change. Gelatin, as denatured collagen, dissolves in water above its critical temperature and behaves as random coils in solution. Upon cooling gelatin molecules partially revert to triple helical collagen-like sequences altering the relative exposure of hydrophobic sites or other chemical groups on the surface of the gelatin molecules,[96] which we found to affect the miscibility of gelatin with PEG (Figure 3-2A). Thereby, we could control the miscibility and the partitioning behavior of PEG/gelatin solutions by varying the temperature and composition (Figure 3-2B). Here, we exploit these properties to create multiphase water-in-oil templates that can be polymerized into 3D structured particles following UV polymerization.

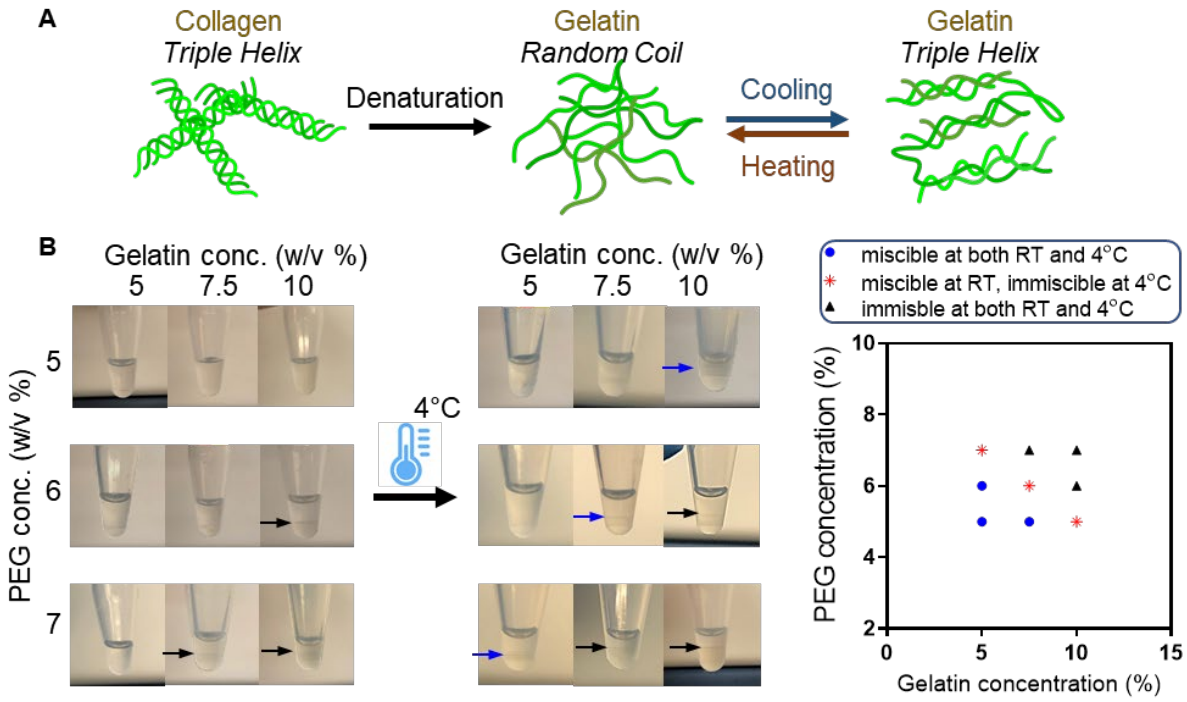

Figure 3-2. Conditional miscibility of PEG and gelatin in aqueous solutions. (A) Conformational change of gelatin molecules induced by temperature variation. (B) The phase separation behavior of a solution comprising different concentrations of 4 arm PEG acrylate 5000 Da and fish gelatin depending on temperature. Three sets of conditions are highlighted in red in which a single phase of precursor materials transitions to separated phases upon a temperature reduction from 25 °C to 4 ° C.

Phase separation of PEG and gelatin is dependent on both the concentration of each component and the temperature of the system.[97] Using a microfluidic droplet generator, we constructed two isothermal binodal curves, corresponding to which PEG and gelatin undergo phase transitions at 4 and 22 °C respectively (Figure 3-3A, B). We used gelatin derived from fish as it still remains liquid at 4 °C, allowing flow to form a minimal energy configuration unlike for porcine-derived gelatin. At concentrations above the binodal curves, the system undergoes phase separation to

create PEG-rich and gelatin-rich regions within microscale water in oil droplets. For concentrations below the binodal curves, PEG and gelatin were miscible. The binodal boundary was found to be lowered by decreasing the temperature, which was attributed to favored interactions between gelatin molecules at lower temperatures (Figure 3-3C, D). By using compositions of the PEG/gelatin solutions located at points between the 4 and 22 °C binodal curves, a transition is enabled from a miscible solution to a phase-separated state induced by the temperature change.

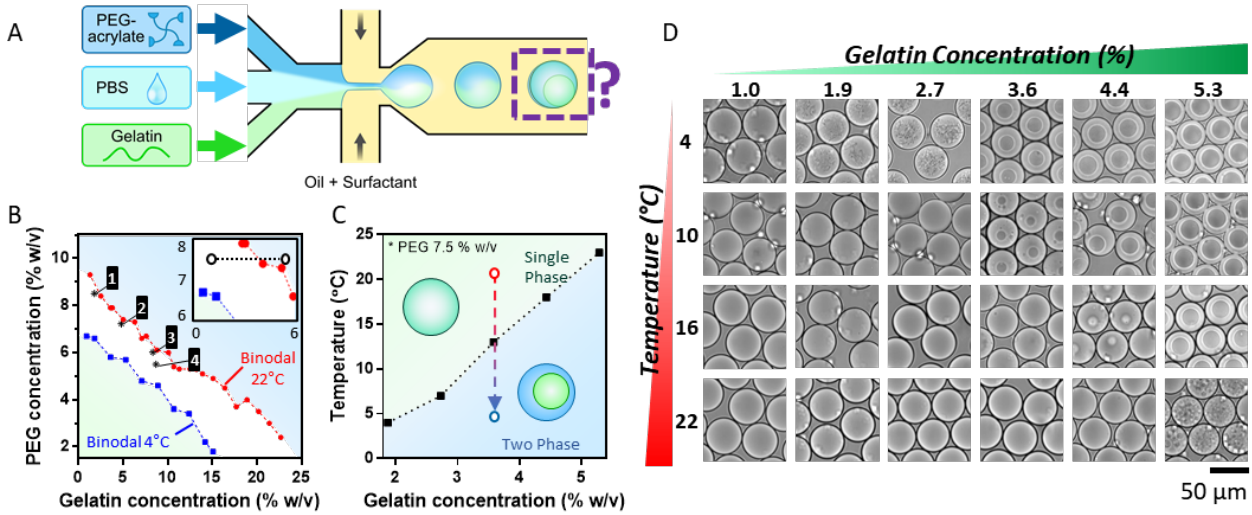

Figure 3-3. Temperature-induced phase separation of PEG and gelatin droplets. (A) Microfluidic setup for construction of PEG-gelatin phase diagrams. PEG acrylate, PBS, and gelatin are injected into separate inlets of a flow focusing device and mixed prior to a droplet generating junction. The composition of droplets is controlled by adjusting the corresponding flow rates. (B) Phase diagram of PEG and gelatin. The isothermal binodal curve is shown for 22 °C and 4 °C. The dashed line in the inset shows the composition range whose transition temperature is indicated in Figure 3-3C. (C) At concentrations between the binodal curves, phase separation can be induced by adjusting the temperature of the system. (D) Example images of droplets with different gelatin

compositions and temperatures (PEG concentration is 7.5% w/v). Phase separation is observed in several different conditions.

When there is no flow, the ATPS droplet geometry is prescribed by the balance of interfacial energies between the PEG-rich, gelatin-rich, and oil phases.[98] These energies reflect the interfacial tensions as well as the interfacial areas between each pair of phases. The more hydrophobic PEG-rich phase encloses the gelatin-rich phase, as the interfacial tension between PEG and fluorinated oil, $\gamma_{PEG-oil}$, is smaller than the interfacial tension between gelatin and the oil, $\gamma_{gelatin-oil}$. However, completely enclosing the gelatin-rich phase leads to an increased interfacial area (PEG-gelatin and PEG-oil) which can be reduced if the gelatin rich phase partially wets the oil phase over an area, *A*. This partial interaction, leading to a Janus morphology, is observed when the interfacial energy of the gelatin-rich and oil phase over *A* is smaller than the interfacial energy of the combined PEG-rich and gelatin-rich ($\gamma_{PEG-gelatin}$) and the PEG-rich and oil phases acting over the same increased area, such that $\gamma_{gelatin-oil} < \gamma_{PEG-gelatin} + \gamma_{PEG-oil}$.

We use a parallelized microfluidic droplet generator to fabricate structured microparticles in high-throughput by exploiting PEG/gelatin compositions that undergo induced phase separation. Step emulsification devices can be easily scaled to generate droplets in high-throughput using hundreds to thousands of parallel channels (Figure 3-4).[18, 91, 99]

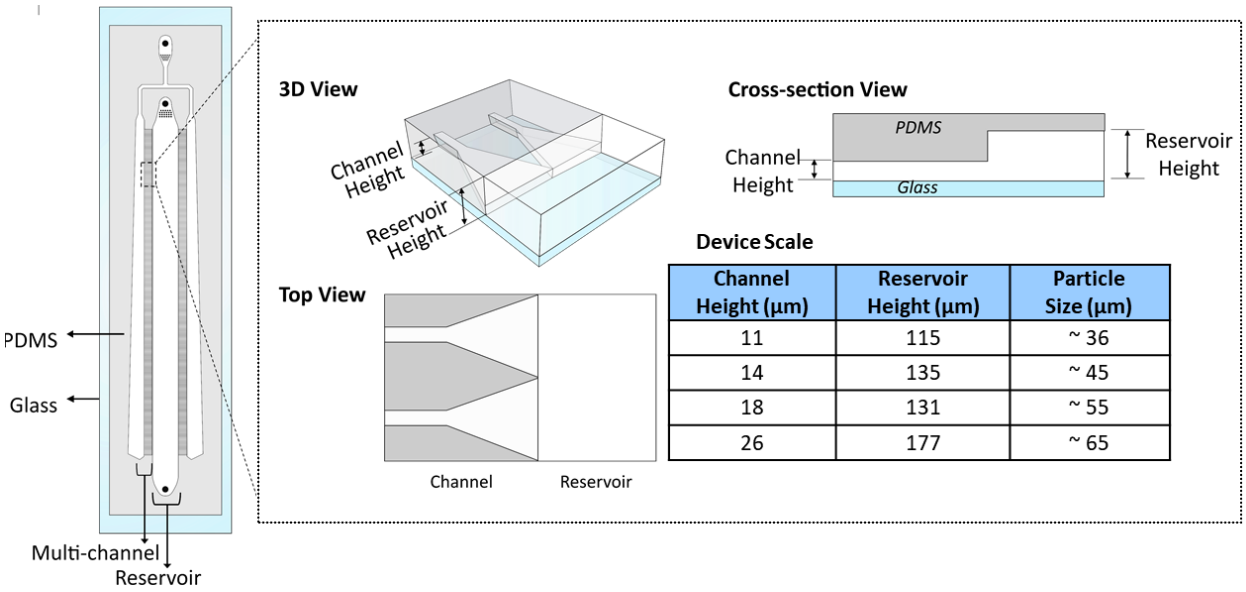

Device Scale

Channel Height (μm)	Reservoir Height (μm)	Particle Size (μm)
11	115	~ 36
14	135	~ 45
18	131	~ 55
26	177	~ 65

Figure 3-4. A schematic of a multi-channel step-emulsification microfluidic device which can be used for high-throughput production of droplets for induced phase separation-based manufacturing at high rates.

The high-scalability of the step-emulsifiers are beneficial especially for manufacturing microparticles with small diameters such as ~35 μm particles. The flow focusing microfluidic device has been commonly used to make two-phased droplets, since it can precisely control different components to make different structures. However, to make small-sized droplets using the flow-focusing device, channels' size of the devices should be reduced accordingly. This causes high viscous force in the channel during the fabrication and lead to a chaotic and unstable flow, which results in non-uniformity in the droplet fabrication. Therefore, we had to use flow rate as low as 0.06 $mL \cdot h^{-1}$ to stably manufacture crescent shaped microparticles with diameter 36 μm using a flow-focusing device, limiting the scalability of manufacturing. Using the step-emulsification device, we dramatically increased the manufacture-throughput. We fabricated

droplets of average diameter 36.5 µm which were highly monodispersed (CV = 3.2 %) at a production rate of 1 mL/hr using a step-emulsifier with a channel height of 11 µm, which is more than 15 times faster than the production rate using a flow-focusing device (Figure 3-5A, B).

Since the droplet formation in a step-emulsifier is mainly driven by interfacial tension,[100] the droplet size was determined by the height of the inlet channel and did not change significantly over a range of flow rates of both the dispersed miscible precursor solution and the continuous oil phases. However, as flow rate increases, collisions between the generated drops resulted in droplet coalescence, which can explain the increase in droplet sizes and their variance at higher flow rates, despite not reaching a jetting regime (Figure 3-5C).

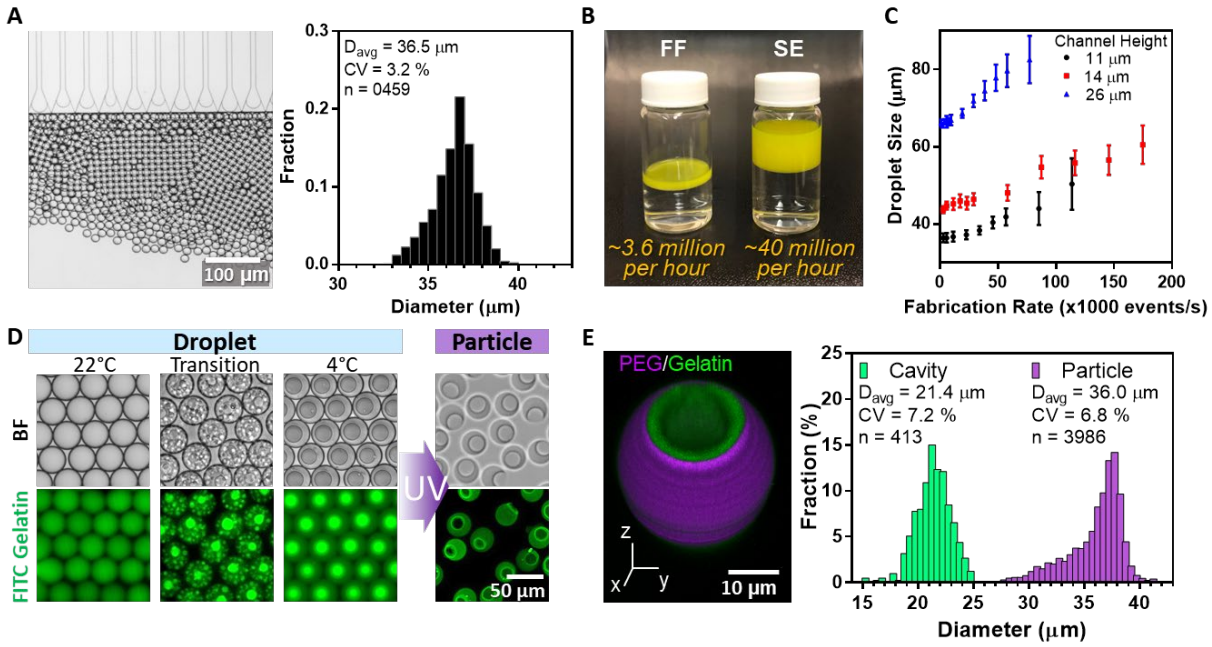

Figure 3-5. Characterization of PEG/gelatin droplets and particles generated using a highly parallelized microfluidic droplet generator. (A) The step-emulsification device yielded droplets of average diameter 36.5 µm which were highly monodispersed (CV = 3.2 %) at a production rate of 1 mL/hr. (B) Visual comparison of the production rate of the parallelized step emulsification

device versus a flow focusing device (1mL·h^{-1} and 0.06 mL·h^{-1}, respectively). (C) Step-emulsifiers with channel heights of 11, 14, and 26 μm generated droplets with mean diameters of 36, 45, and 65 μm, respectively. (D) Microscopy images of PEG/gelatin (6.3 %w/v PEG and 4.5 % w/v gelatin) droplets undergoing induced phase separation from a reduction in temperature and resulting in monodisperse shaped particles after UV polymerization. Green fluorescent images show the distribution of FITC conjugated gelatin during the process to aid in visualization. (E) The morphology of the crescent shaped nanovials was confirmed using confocal microscopy.

Despite of its benefits of high-throughput production rate, parallelized step-emulsifiers have not been adopted to fabricate microparticles with 3D shapes, since they are limited in that only a single phase or stable mixture can be easily introduced when parallelized. Leveraging the PEG/gelatin ATPS system, we are able to surpass these limitations by first generating droplets with a step emulsification device, starting at a single-phase composition between the binodal lines, and then inducing phase separation by reducing temperature to create uniform multiphase geometries.

As the temperature of the system is reduced, very small domains of the gelatin-rich phase form within the larger drops, which coalesce and coarsen over time to form a single large spherical gelatin-rich domain in each drop (Figure 3-6).

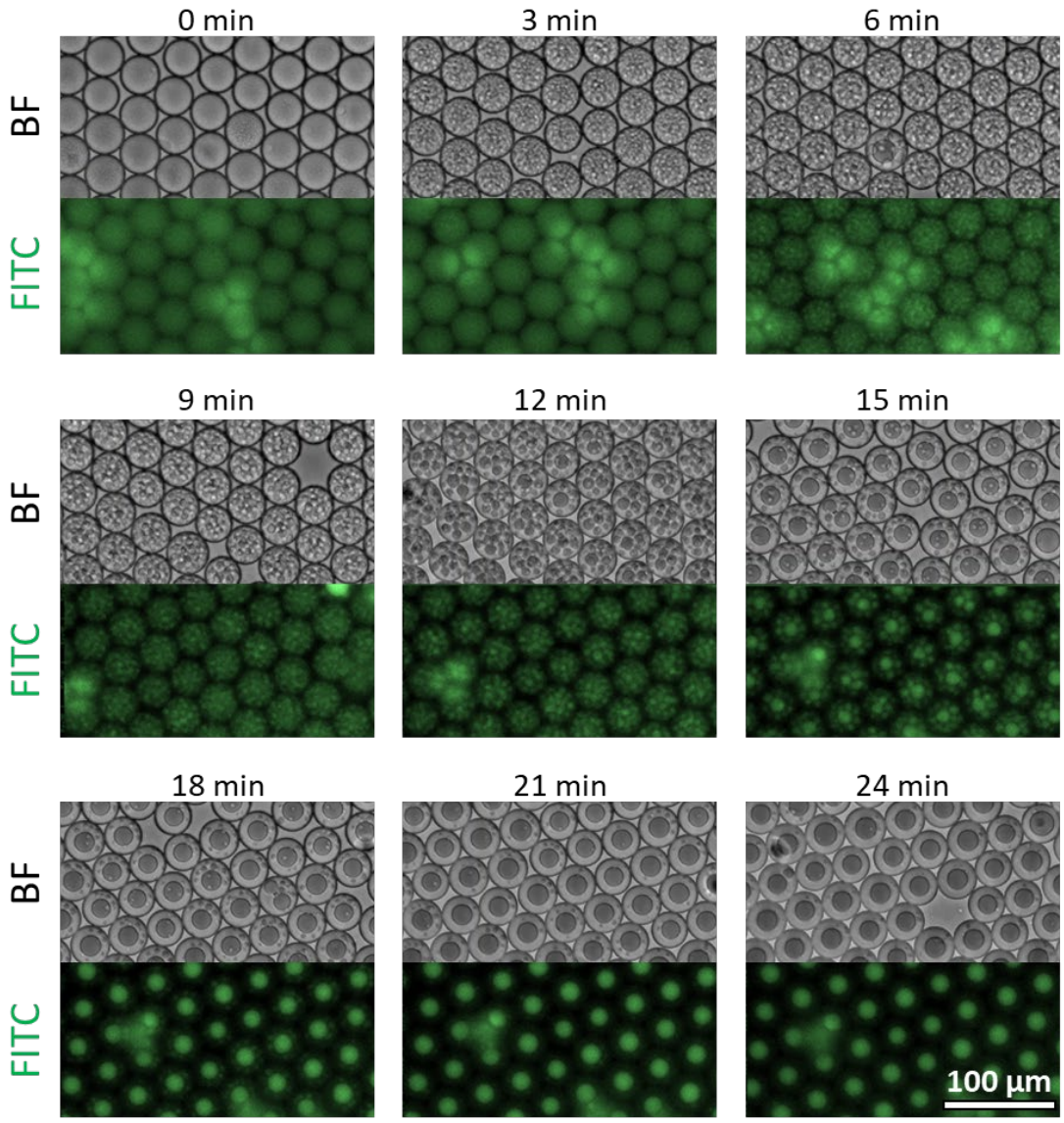

Figure 3-6. Bright field and FITC microscopy images of PEG/gelatin (6.3 % w/v PEG and 4.5 % w/v gelatin) droplets undergoing induced phase separation from a reduction in temperature.

The phase-separated droplets were then exposed to UV light to crosslink the PEG portion, yielding particles with crescent-shaped cross-sections after washing steps (Figure 3-5D). The resulting

particles were highly uniform in their size with an average diameter of 36.0 µm (CV = 6.8 %) and average cavity diameter of 21.4 µm (CV = 7.2 %) (Figure 3-5E). For the entire study, across different temperatures and in the presence of buffers and different media we did not observe particle aggregation or swelling, which indicates high stability of the nanovial particles. The particles were generated at rates of 40 million/hour which is ~11 times faster than previous methods that used a single flow-focusing device.[79] Nanovials of various sizes could be generated by using step-emulsifiers with different channel heights. The morphology of the ATPS droplets and resulting particles can be adjusted by changing the composition of PEG and gelatin. The compositions affect both the relative volumes of the PEG-rich and gelatin-rich regions as well as the balance of interfacial tensions between the PEG-rich, gelatin-rich, and oil phases. Increasing the concentration ratio of gelatin to PEG resulted in droplets with a higher volume fraction of the gelatin-rich phase, and nanovials with a larger exposed cavity when crosslinked (Figure 3-7A). Compositions were also found that result in particles with completely enclosed cavities (*i.e.* hollow shell particles) (Figure 3-7B).

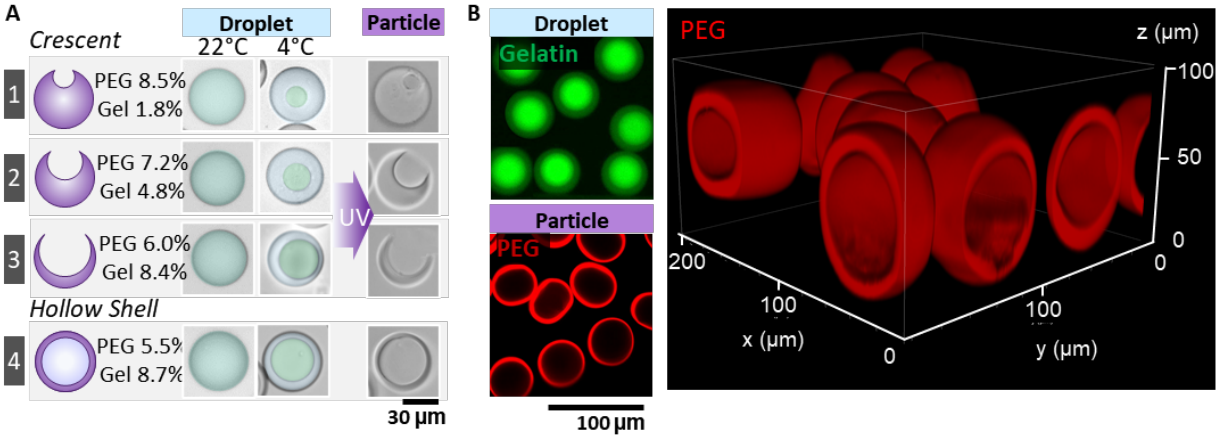

Figure 3-7. Different particle shapes fabricated using a parallelized step emulsification device and temperature-induced phase separation. (A) The structure of the resulting particles can be modified by adjusting the composition of PEG .and gelatin (The corresponding compositions are shown on the plot in Figure 3-3B). Conditions are shown for crescent particles with different cavity ratios as well as fully enclosed hollow shell particles. Droplets are false colored to aid in visualization of PEG (green) and gelatin (blue) phases. (B) The morphology of the hollow shell particles was confirmed using confocal microscopy.

Our fabrication approach results in a localization of gelatin on the inner cavity surface of the crescent shaped particles, which is advantageous for cell microcarrier applications utilizing this nanovial geometry. We found that during our particle manufacturing process gelatin molecules near the interface of the PEG-rich and gelatin-rich phases become trapped in the cross-linked surface. We used fluorescein isothiocyanate (FITC)-conjugated gelatin to visualize this localization effect using fluorescence and confocal microscopy (Figures 3-5D, 3-6, 3-8A). We found that even after vigorous washing steps, the gelatin remained embedded in the particle surface indicating either physical entanglement and/or chemical bonding had occurred.

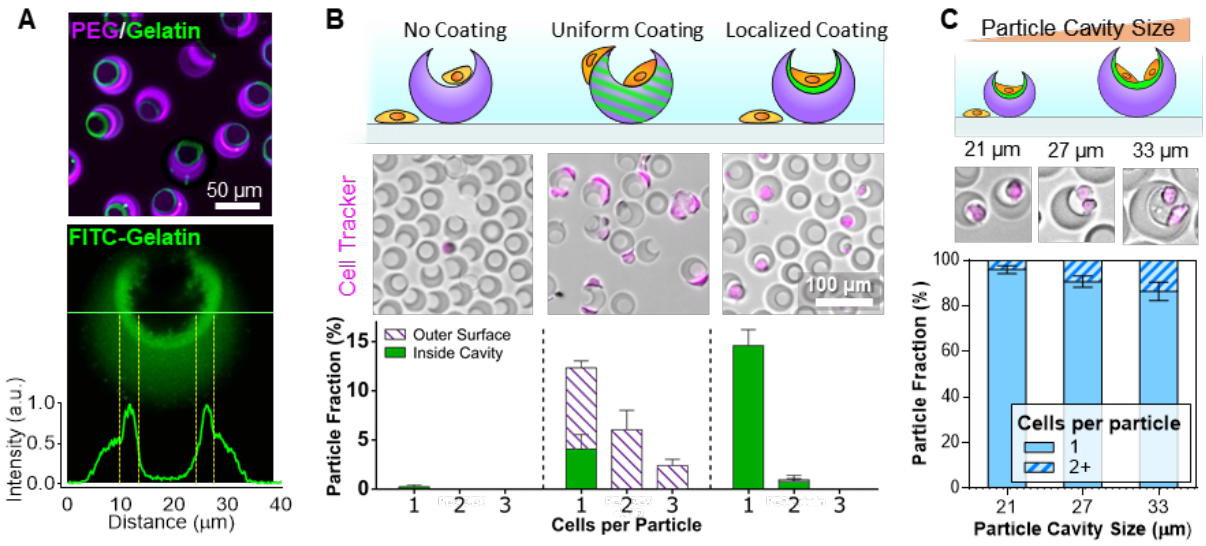

Figure 3-8. Nanovials with gelatin coated cavities for cell loading. (A) Confocal microscopy shows the localization of gelatin on the inner cavity surface of the crescent shaped particles. (B) Cell loading efficiency on nanovials with different distributions of binding moieties (No coating – PEG particles without RGD or gelatin, Uniform coating – PEG particles with RGD uniformly distributed, Localized coating – gelatin localized to the inner cavity). (C) The fraction of nanovials with single cells increases as the particle cavity size approaches the cell diameter.

To investigate the effect of the localized gelatin layer on cell adhesion and growth in nanovials, we compared the cell loading on three different particles with no binding motif, with uniform Arg-Gly-Asp (RGD) motifs, and with localized gelatin, respectively (Figure 3-8B). Chinese hamster ovary (CHO) cells were seeded at a 0.6:1 cell-to-particle ratio and after 2 hours of incubation, the samples were rinsed using a 20 µm reversible-strainer to remove the unbound cells. The particles without cell binding motifs had few cells attached to the particles (0.26 ± 0.17 % of particles had adhered cells). More cells were bound to RGD-coated nanovials as expected (20.73 ± 1.77 % of

particles), but a significant fraction of cells was bound to the outside of the particle (80.31 % of cells bound to particles). Particles with localized gelatin showed a significantly larger fraction of cells bound to the particle cavity, 15.39 ± 1.62 % of particles, while less than 1.33 ± 0.73 % of them were bound to the outer surface (a 60-fold improvement as compared to uniformly coated particles). By avoiding external adhesion, the majority of cells can be localized to cavity region which can help ensure loading of single cells as well as reduce unwanted shear stress during handling steps, improving cell viability. Also, we demonstrated that the cells bound to nanovials can be released by using a protease such as trypsin when it is required (Figure 3-9).

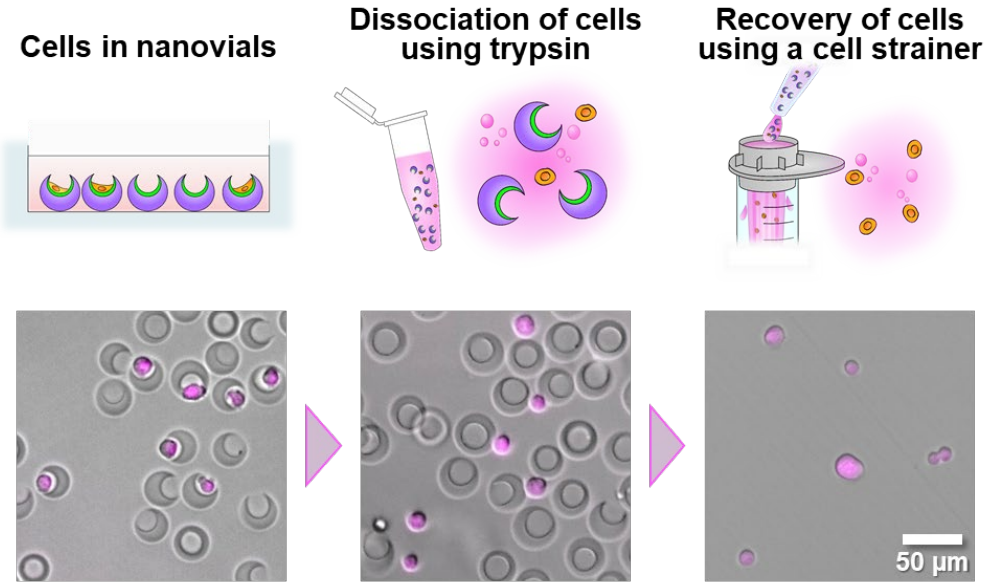

Figure 3-9. Schematics and microscope images to describe the dissociation and recovery of cells from nanovials using trypsin. Cells bound to nanovials were trypsinized and released from nanovials. The solution with unbound cells and nanovials were strained with a 20 µm cell strainer and cells were isolated from nanovials.

Localized adhesion combined with size exclusion effects of the cavity enables deterministic loading of single cells into the particle cavities. We found that for the same cell seeding concentrations, nanovials with uniformly distributed binding moieties yielded a significantly larger fraction of nanovials containing more than one cell (> 80 % cell containing nanovials) than nanovials with gelatin localized to the cavity (~ 1% of cell containing nanovials). The high-multiplet fraction for the nanovials with uniformly distributed binding moieties was attributed to the larger fraction of cells bound to the outside of the particles and resulted in loading statistics worse than Poisson loading (Figure 3-10A). For nanovials with localized gelatin, the reduction in cells binding to the outer surface combined with exclusion effects of the inner cavity size was found to improve loading of single cells beyond distributions predicted by Poisson statistics. Both cells loaded in RGD-coated nanovials and localized gelatin-nanovials showed high viability (>80 % over 5 days of culture (Figure 3-11)). Testing a range of nanovial sizes with three different cavity diameters 21, 27 and 33 μm, we found that as the cavity approached the average size of the cells (~17 μm diameter) the fraction of nanovials with singlets increased and multiplets decreased (Figures 3-8C, 3-10B). Since it is difficult to fit more than one cell, the nanovials with cavities of 21 μm in diameter maintained a lower fraction of multiplets than Poisson loading. This effect became more evident at the higher cell seeding densities. When increasing the cell-to-particle ratio from 0.4:1 to 1:1, the multiplet fraction for nanovials with 21 μm cavities was reduced by as much as 50% compared with Poisson loading (Figure 310C). We expect that improved singlet loading can dramatically improve utility of the cell carriers for applications where clonality is critical and overcomes one of the long-standing limitations of microfluidic platforms that are dictated by Poisson loading.[101]

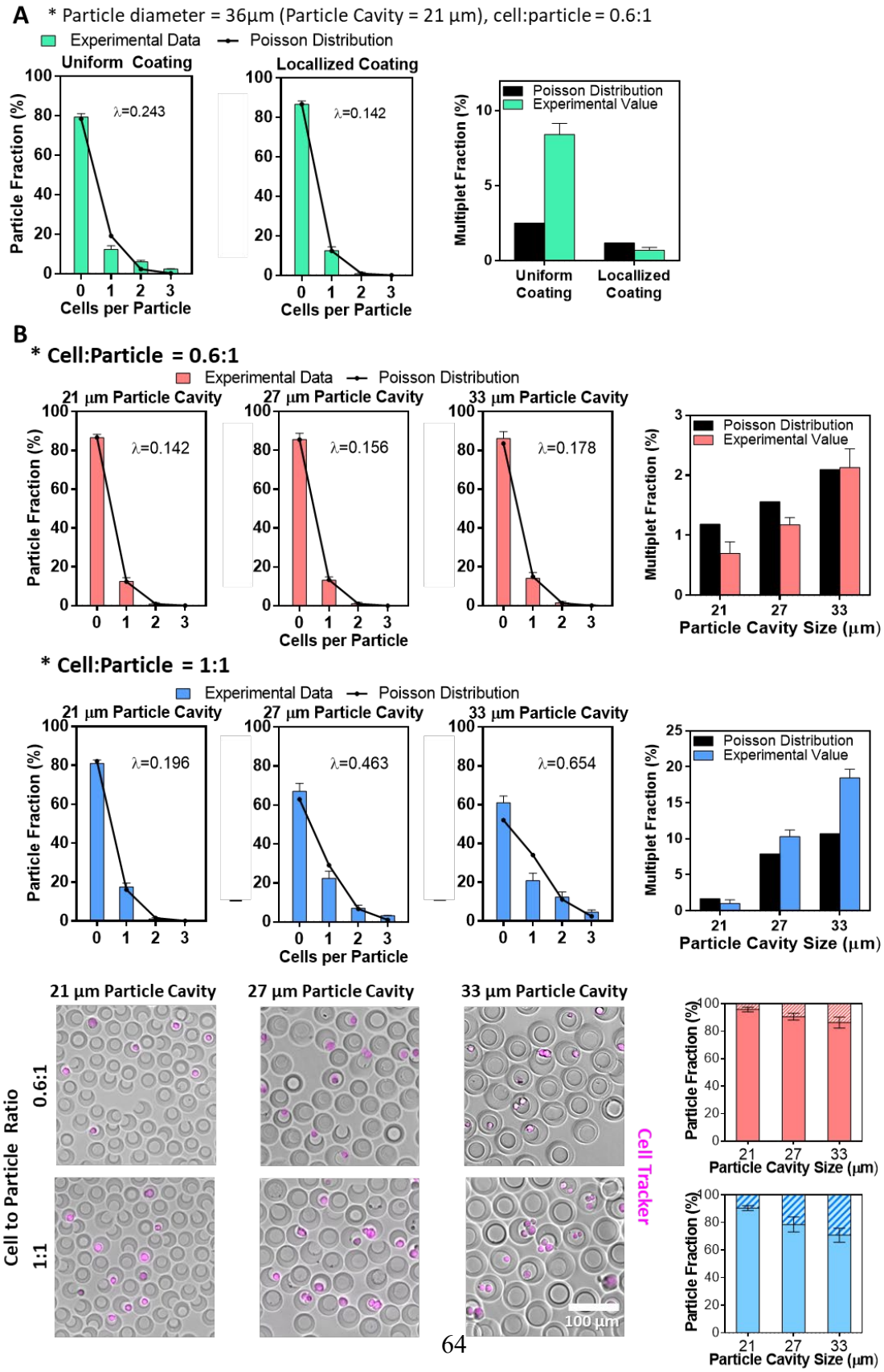
A
* Particle diameter = 36µm (Particle Cavity = 21 µm), cell:particle = 0.6:1
Experimental Data
Poisson Distribution
Uniform Coating
Localized Coating
Particle Fraction (%)
λ=0.243
λ=0.142
Cells per Particle
Multiplet Fraction (%)
Poisson Distribution
Experimental Value
Uniform Coating
Localized Coating
B
* Cell:Particle = 0.6:1
21 µm Particle Cavity
27 µm Particle Cavity
33 µm Particle Cavity
λ=0.142
λ=0.156
λ=0.178
Particle Cavity Size (µm)
* Cell:Particle = 1:1
λ=0.196
λ=0.463
λ=0.654
Cell to Particle Ratio
0.6:1
1:1
Cell Tracker
100 µm

Figure 3-10. Further characterization of cell loading into nanovials in comparison to Poisson loading. (A) Comparison of loading into 36 micron nanovials with uniform binding moieties and localized binding moieties. Particles with uniform binding moieties have loading statistics worse than the Poisson distribution, likely due to cell clusters being able to bind to the outside of the nanovials. This trend is highlighted when looking at the fraction of nanvovials with multiplets (>1 cell per nanovial). Localized binding moieties in particles promotes deterministic cell loading and reduces the multiplet fraction below the number predicted by Poisson statistics. (B) As the cavity size approached the average size of the cells (~17 μm), the fraction of nanovials with singlets increased and multiplets decreased. (C) The deterministic loading became more evident at higher cell seeding densities.

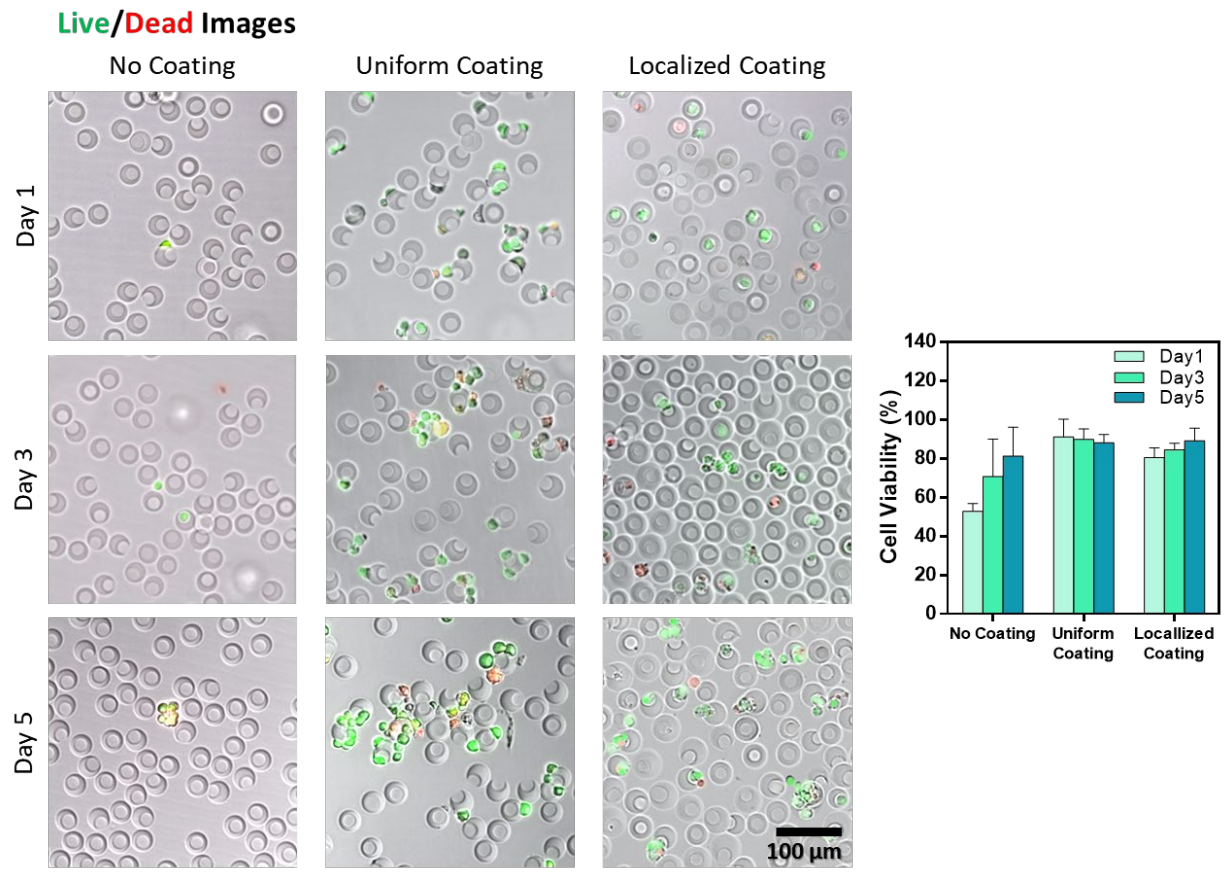

Figure 3-11. Viability of cells bound to nanovials with different cell binding moieties as reported in Figure 3-8B. No Significant difference in viability was observed for the samples with uniform and localized coating of binding moieties.

The 3D-structured nanovials with gelatin functionalized cavities facilitate cell growth and prevent cell death during standard assays that can induce high fluid dynamic shear stress such as fluorescence activated cell sorting (FACS). We sorted both freely suspended cells and cells adhered in nanovial cavities at high-throughput using FACS (~270 events/second) (Figure 3-12A-C) and expanded cells after sorting over several days (Figure 3-12E). We found that cells bound in the nanovial cavities showed significantly higher viability than unbound cells right after sorting

(54.9% *vs*. 80.0%, $p < 0.0001$) (Figure3-12D). Also, during the 5 days of culture after sorting, there were no significant differences in viability of nanovials bound cells that were sorted *vs* samples that were not sorted (Figure 3-12F). We attribute the high cell viability to the cavity acting as a protective shelter that reduces hydrodynamic shear stress on cells during the sorting process.[102] To further evaluate effects on long-term growth from the sorting process, we investigated the proliferation of cells before and after sorting. At different time points, the number of cells per each sample was counted and normalized to the number of nanovials for both sorted and un-sorted samples. The cells loaded in nanovials in both groups proliferated over time increasing the number of cells per nanovial (Figure 3-12G), suggesting that the sorting process did not have a substantial effect on cell growth. This high cell viability and activity is critical for the success of clonal expansion after sorting single cells and could be advantageous for analysis and recovery of adherent cells.

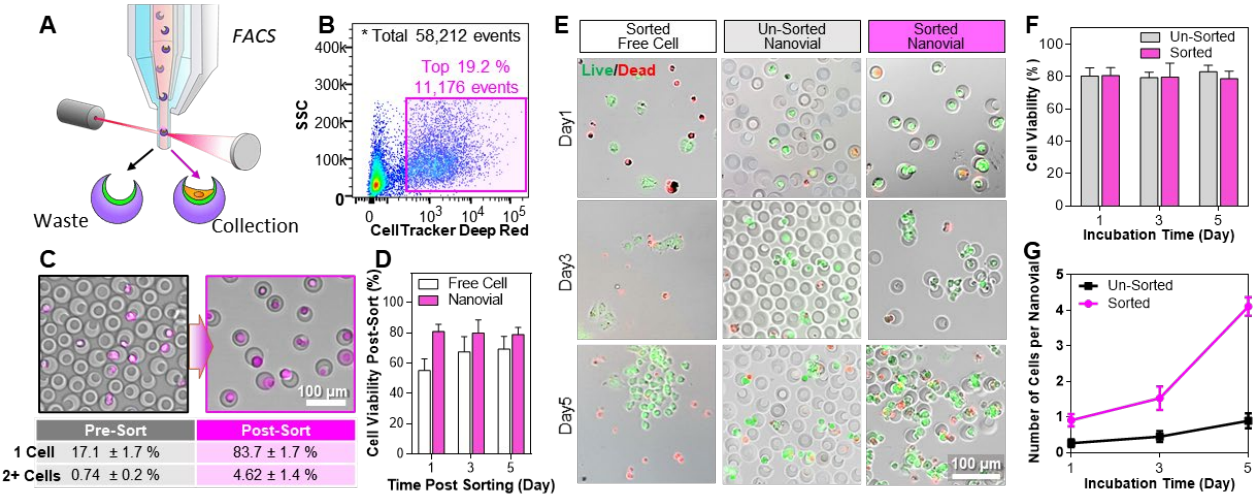

Figure 3-12. Nanovials with gelatin coated cavities for cell sorting. (A) A schematic to describe sorting nanovials loaded with cells. (B) Sorting nanovials loaded with cells based on CellTracker signal using FACS. (C) Cell-laden nanovials were sorted with high efficiency using FACS. (D)

Viability of suspended cells (Cell) and cells loaded in gelatin-nanovial cavities (Nanovial) after sorting. Cells bound to nanovials showed significantly higher cell viability following sorting, suggesting these nanovials provide protection from fluid shear stresses during the sorting process ($p < 0.0001$). (E) Example images of live/dead stained cells bound to nanovials after sorting. Cell viability of freely suspended cells after sorting and un-sorted cells on nanovials were also evaluated as controls. (F) Viability of cells loaded on nanovials remained ~80% over 5 days of culture for both un-sorted and sorted samples. (G) Average number of cells in nanovials increases as they proliferated for both sorted and un-sorted samples.

Gelatin localized on the inner particle surface enables facile spatial modification of particles with other biomolecules of interest. Due to the abundance of functional handles such as free amines and carboxylic acid, gelatin is a convenient base for bioconjugation. For example, free amines can be easily linked to using *N*-hydroxysuccinimide (NHS) ester conjugates (Figure 3-13A). Using an NHS-biotin conjugate we selectively modified the inner cavity of the particles with biotin, a biomolecule commonly used as a high affinity linker for antibodies, proteins, or oligonucleotides *via* the extremely high affinity biotin-streptavidin non-covalent interaction. To visualize the difference in localization, we fabricated particles with both biotin incorporated throughout the PEG backbone (Biotin-PEG) and biotin linked directly to the localized gelatin (Biotin-Gelatin) and stained with fluorescent streptavidin. Fluorescence and confocal microscopy revealed that the Biotin-PEG particles have a uniform distribution of biotin groups, while Biotin-Gelatin particles have a significant increase in fluorescence intensity around the inner surface of the cavity, indicating a higher concentration of available biotin groups (Figure 3-13B, C). The localization of biotin molecules in the cavity can dramatically expand the application of nanovials. As an example,

biotin molecules can be used to link biotinylated antibodies through streptavidin-biotin coupling in order to capture cells that otherwise do not adhere strongly to nanovials, such as suspension cells. We demonstrated that various cell types, including non-adherent cells, can be loaded into nanovials by using antibodies against cell-surface-specific antigens (Figure 3-14).

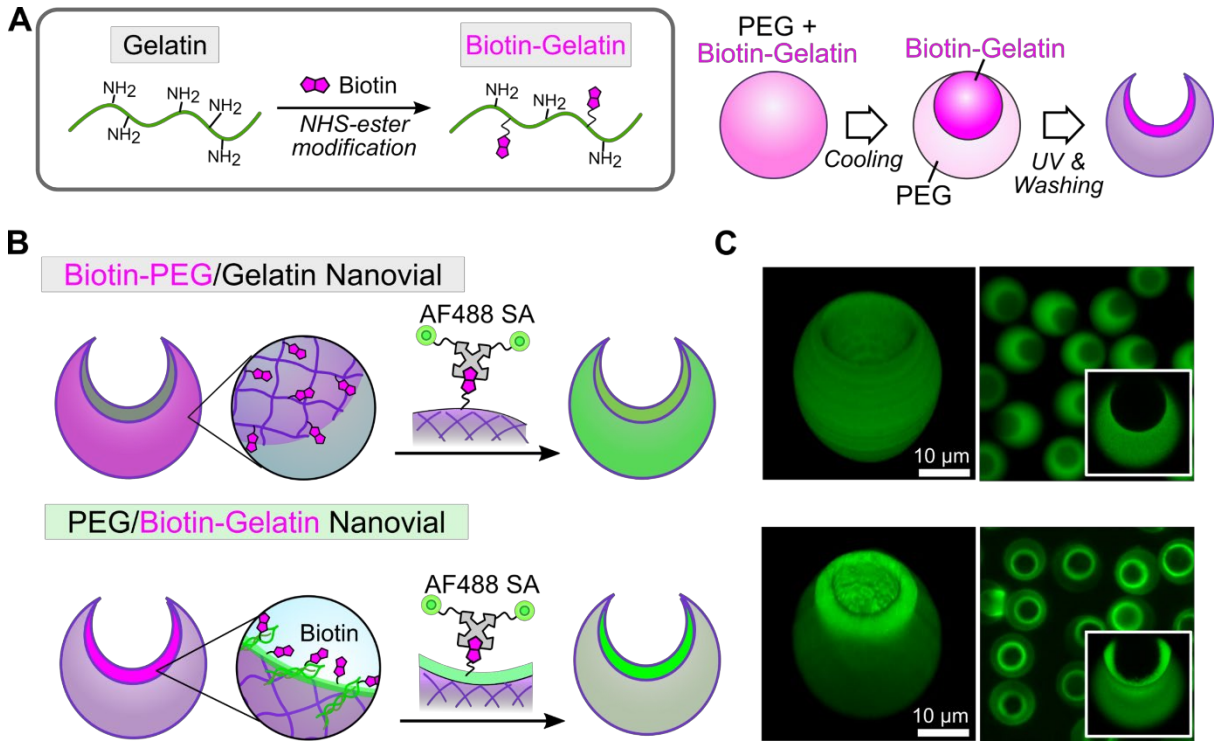

Figure 3-13. Spatial modification of particles with biomolecules using localized gelatin. (A) Free amine groups on gelatin are conjugated with biotin using NHS-ester modification. (B) Both biotin modified PEG (Biotin-PEG) and biotin modified gelatin (Biotin-Gelatin) are conjugated with AlexaFluor™ 488 conjugated streptavidin after fabrication. (C) Fluorescence and confocal imaging show increased fluorescence intensity in the inner cavity of Biotin-Gelatin nanovials indicating localization of biotin.

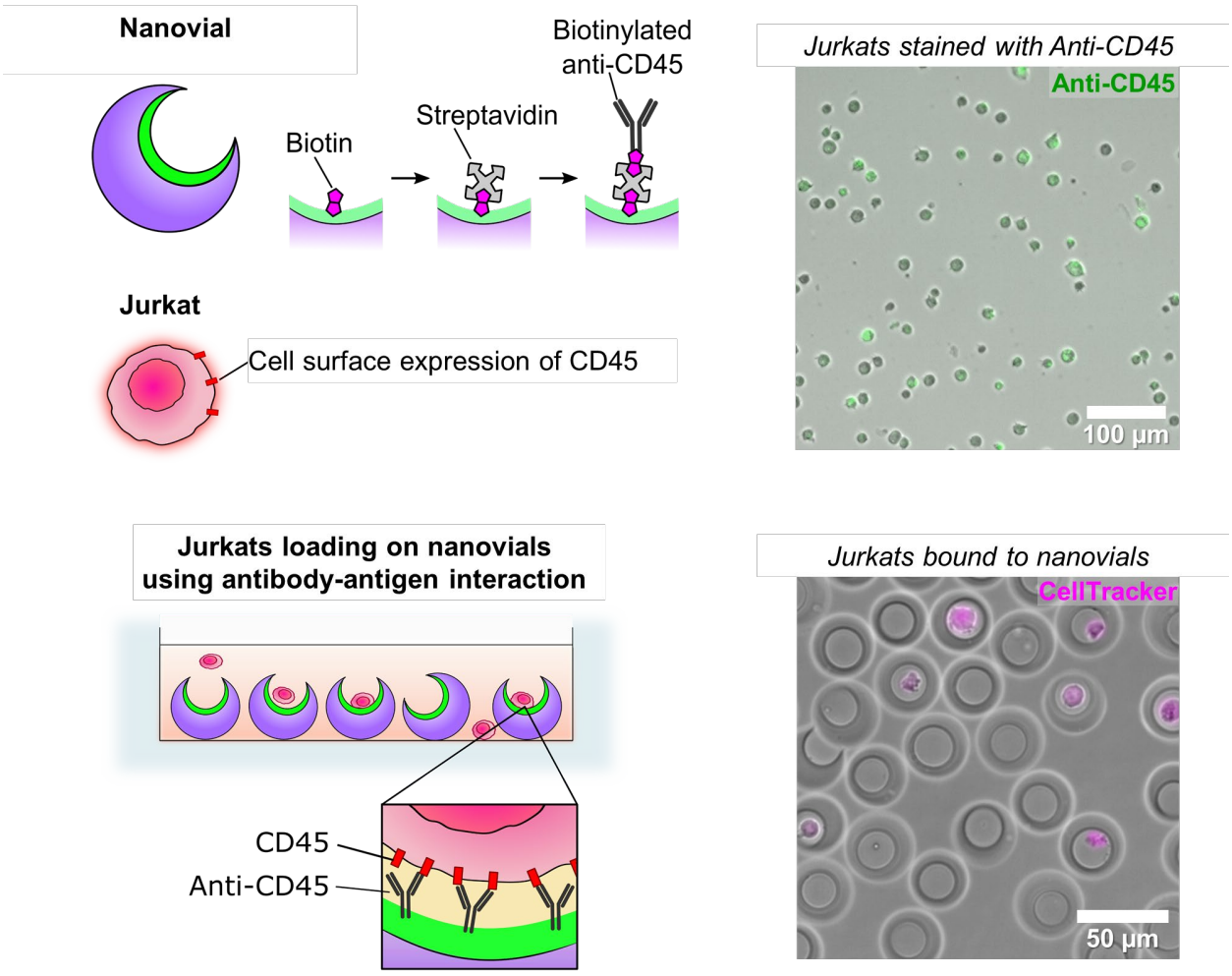

Figure 3-14. Loading jurkats to nanovials using antibodies that are against cell specific antigens. Jurkats with CD45 expression on their surface bind to nanovials labeled with anti-CD45 through antibody-antigen interactions.

The ability to spatially pattern biomolecules can be further exploited to enhance detection accuracy for high throughput analysis of single cell secreted products. Previously, we have shown that nanovials can be used to perform single cell secretion assays by using the particle surface to immobilize secreted antibodies and perform a fluorescent sandwich immunoassay. To reduce cross-talk between cells and ensure accurate measurements an emulsification step was required

with the previous particles.[79] Here, we show that performing the assay with nanovials, in which biotin is localized to the inner cavity surface, substantially reduces the amount of cross-talk between cells enabling single cell secretion assays, without the need for extra steps to prevent cross-talk.

To characterize the effect of localized biotin on cross-talk, we measured the secretion of a human immunoglobin G (IgG) against interleukin 8 (IL-8) produced by CHO cells loaded on both Biotin-PEG nanovials and Biotin-Gelatin nanovials (Figure 3-15A). We characterized the amount of cross-talk by introducing a population of empty control particles with a fluorescent label prior to the incubation step and measured the relative amount of secretions that were bound to these control "empty nanovials" compared to the cell containing population by flow cytometry (Figures 3-15B, C, 3-16).

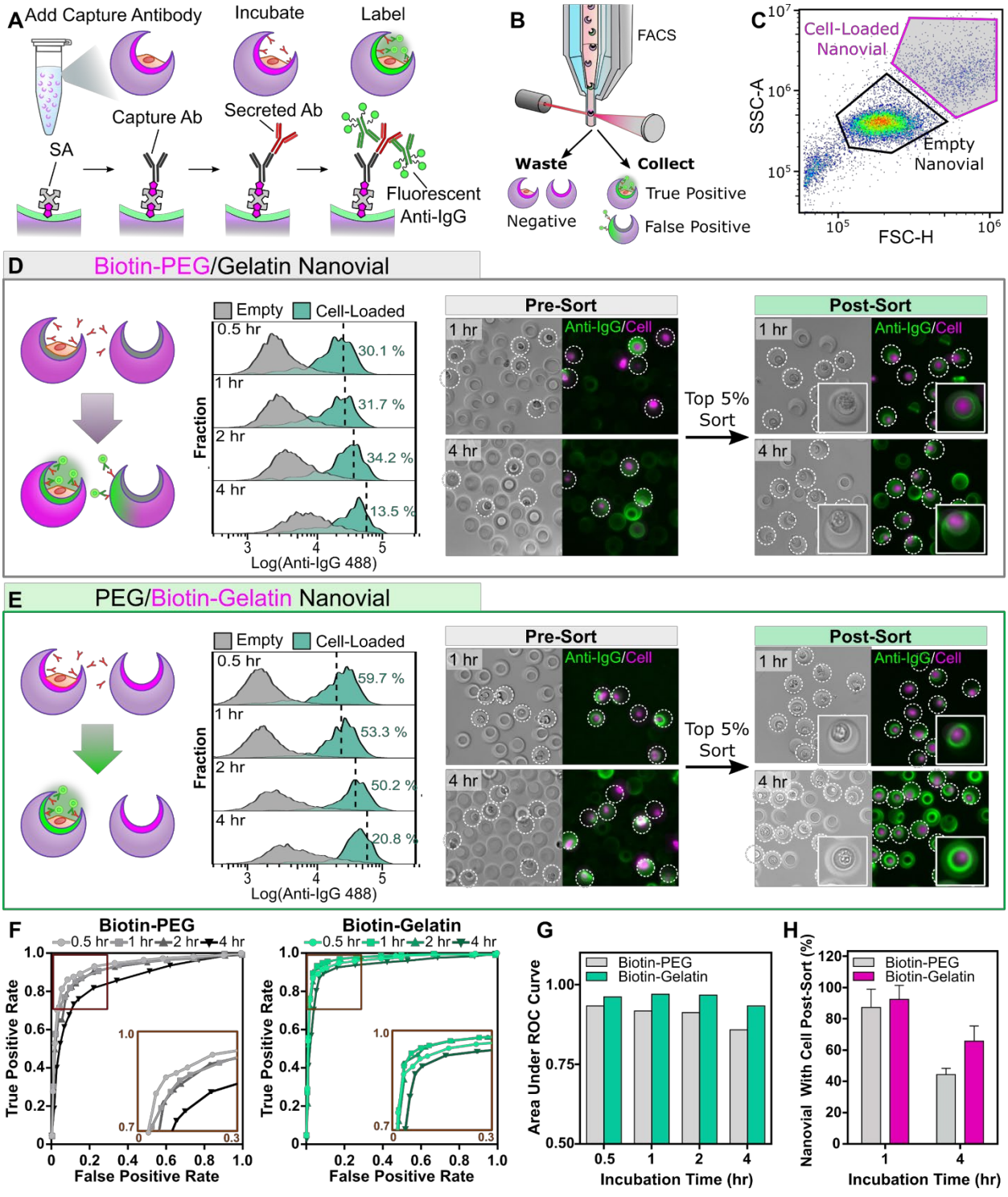

Figure 3-15. Localized conjugation of affinity agents reduces cross-talk for single cell secretion assays. (A) Single cell secretion assays were performed by first loading human IgG

producing CHO cells into nanovials. After cell adhesion free biotin groups were conjugated with streptavidin and biotinylated antibodies against IgG. Cells were then incubated for different durations to accumulate secreted molecules on the surface of the particles and captured secretions were then fluorescently labeled with fluorophore conjugated antibodies. (B) The nanovials were analyzed and sorted in high-throughput based on secretion signals using FACS. (C) A flow cytometry scatter plot of 0.5 hr incubated nanovials, showing distinct scatter signal for nanovials containing cells. (D,E) Flow cytometry analysis and microscopy images showed that assays with Biotin-Gelatin nanovials (E) led to higher secretion signal and lower background intensity on empty nanovials as compared to Biotin-PEG nanovials (D) due to the localized capture antibody in cavity. The dashed lines in the histograms show the threshold to exclude the bottom 99% of control empty nanovials. The samples were stained with CellTracker before imaging to aid in visualization of cells. (F) ROC analysis was performed to compare the classification accuracy for Biotin-PEG and Biotin-Gelatin nanovial-based assays. (G) Area under the ROC curve indicates that Biotin-Gelatin nanovials enable more accurate classification than Biotin-PEG nanovials due to reduced cross-talk ($p < 0.1$) across all incubation times. (H) Nanovial fraction containing cells after incubating for 1 and 4 hours and sorting, reflecting the cross-talk differences between Biotin-PEG and Biotin-Gelatin.

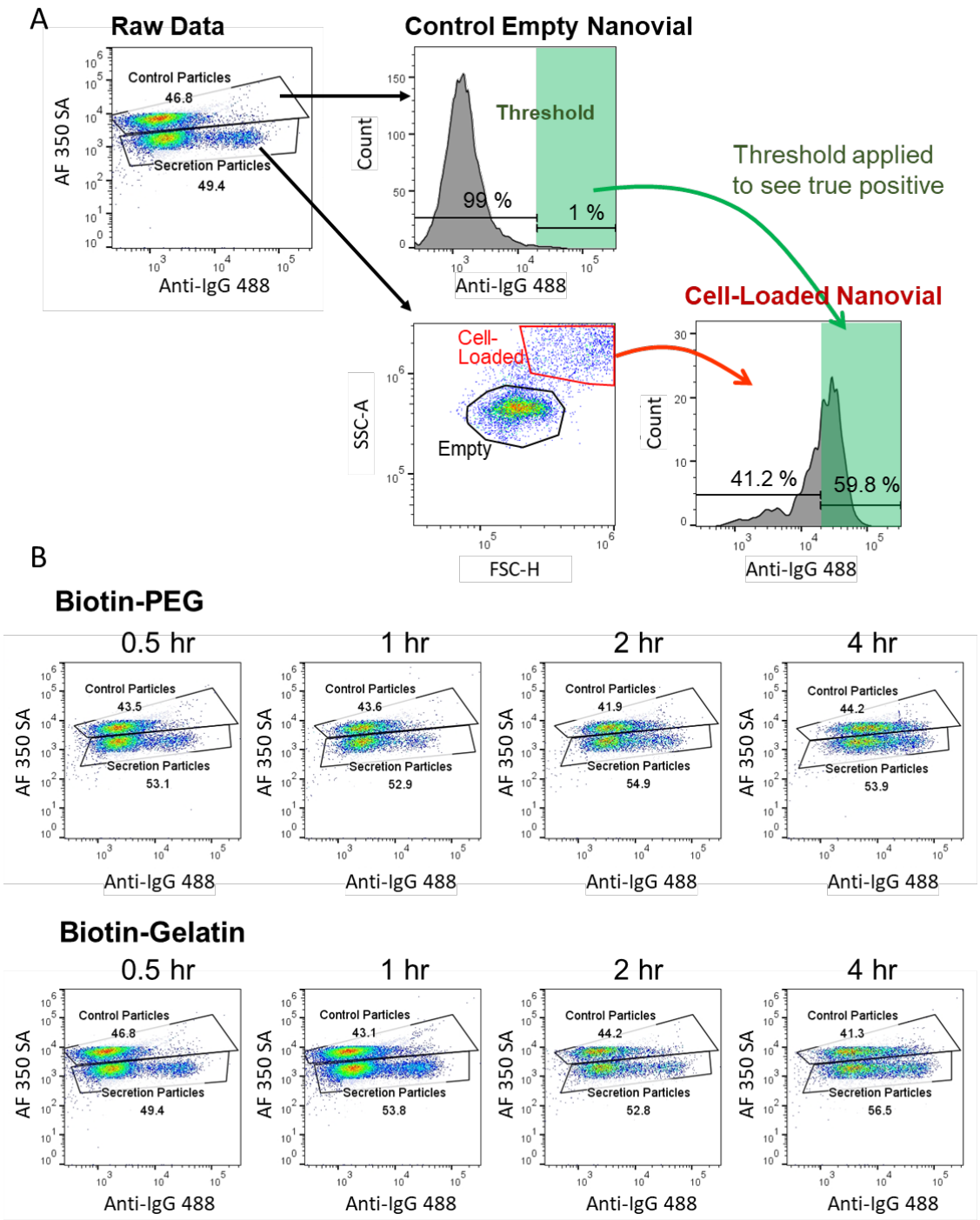

Figure 3-16. Flow cytometry gating strategy and scatter plots for secretion assay samples from Figure 6. (A) Cells that fall off during the assay can potentially skew the higher false positive signal. To account for this variability particles stained with AF350 were spiked into the

population at the beginning of the secretion assay to quantify amount of cross-talk signal. This population was first gated from the remainder of the population to define as our empty nanovial intensity. The remaining population was gated and the cell containing sub-population was then gated based off increased forward and side scatter signal. (B) Raw scatter plots and gating for all of the samples.

We found that Biotin-Gelatin nanovials possessed a higher secretion signal and lower background intensity as compared to Biotin-PEG nanovials, indicating that the localized capture antibody in cavity of nanovials enriched the secretion signals and reduced secretion leak from cells to neighboring empty nanovials (Figure 3-17). We defined a threshold of fluorescence intensity to exclude the bottom 99 % of control nanovials (1 % false positive rate) and identified the percent of cell-loaded nanovials (true positive rate) that were above this threshold (Figure 5D-E). For Biotin-PEG nanovials we found that ~30-34% of cell-loaded nanovials possessed positive signal above this threshold when incubated within 2 hrs, which decreased substantially by 4 hrs to ~13% due to an increase in crosstalk to control nanovials (Figures 3-15D, 3-17B). For the Biotin-Gelatin particles, ~60% of cell-loaded nanovials were detectable above threshold after 30 minutes of incubation, which decreased slowly over time to ~21% at 4 hrs, indicating a significant reduction in cross-talk as compared to Biotin-PEG nanovials (Figure 3-15E, 3-17B).

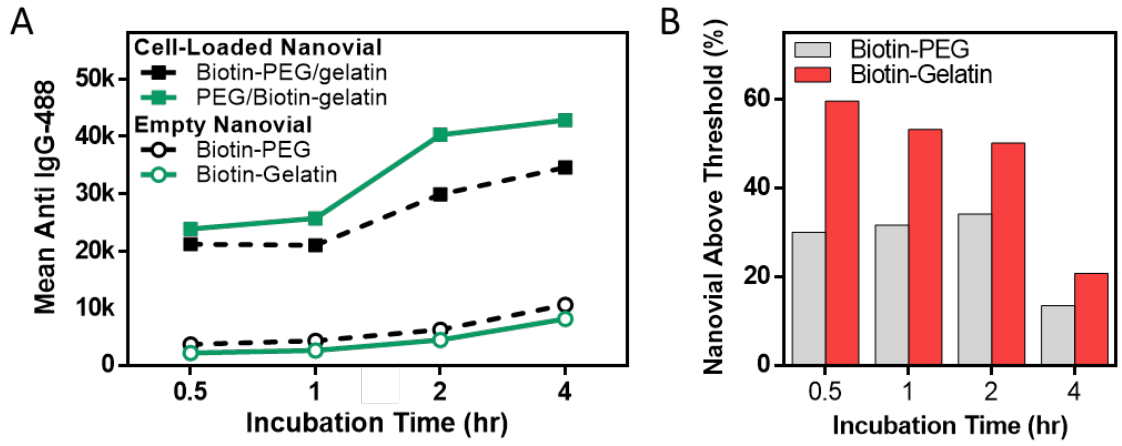

Figure 3-17. Additional characterization of the single cell secretion assay. (A) Biotin-Gelatin nanovials showed lower IgG secretion signal on empty nanovials, while having higher signal on cell-laden nanovials when compared to the same assay performed on biotin-PEG nanovials. (B) When we defined a threshold of fluorescence intensity to have an only 1 % false positive rate, Biotin-Gelatin nanovials had a higher fraction of nanovials with positive signal above this threshold, indicating a significant reduction in cross-talk. For both nanovials, the fraction dropped as the nanovials were incubated longer than 2 hours.

To fully characterize the capability of selecting out cell-containing nanovials from nanovials with signal cross-talk, we performed receiver operating characteristic (ROC) analysis, a standard method to assess classification accuracy independent of a single threshold. For each condition, a curve of true positive rate *versus* its false positive rate were obtained across a series of cutoff levels to depict the trade-off between the sensitivity and specificity (Figure 3-15F) and the area under the curve (AUC) for each ROC curve was calculated (Figure 3-15G). The ROC curve indicated that Biotin-Gelatin nanovials overall provide higher accuracy than Biotin-PEG nanovials with a minimum trade-off between true positive rate and false positive rate (Figure 3-15F). While both

nanovials allow accurate detection of secretions (AUC > 0.85), Biotin-Gelatin nanovials showed significantly higher AUC values (AUC > 0.93) than Biotin-PEG nanovials due to the reduced cross-talk ($p < 0.1$) (Figure 3-15G). This was also reflected in fluorescence microscopy images of the samples (Figure 3-18). The reduction in cross-talk for Biotin-Gelatin nanovials was further evidenced by inspecting nanovials sorted based on the top 5 % of fluorescence intensity. For shorter incubation times (1 hr) both the Biotin-PEG and Biotin-Gelatin particles had a relatively low fractions of nanovials without attached cells: 7.1 % and 12.1 % respectively (Figure 3-15D, E, H). After 4 hours, the amount of empty nanovials sorted for the Biotin-PEG nanovial condition increased to 55.5 ± 4.0 % while Biotin-Gelatin nanovial sorts yielded only 33.8 ± 8.6 % empty nanovials (Figure 3-15H). We hypothesize that having the antibody binding sites localized in the cavity reduces the amount of leaked secretions reaching the binding sites of other particles from convective transport. Convective flows into nanovial cavities are expected to be reduced given the boundary conditions. Further, it is possible that the higher concentration of binding sites in the cavity of the Biotin-Gelatin particles more efficiently captures secretions before they have time to diffuse out of the cavity or be convected away, further reducing crosstalk. Taken together, we conclude that locally functionalized nanovials can effectively capture the secretions from the single cells with lower cross-talk, enabling more accurate analysis and sorting of desired sub-populations with a reduced number of processing steps than previous approaches.

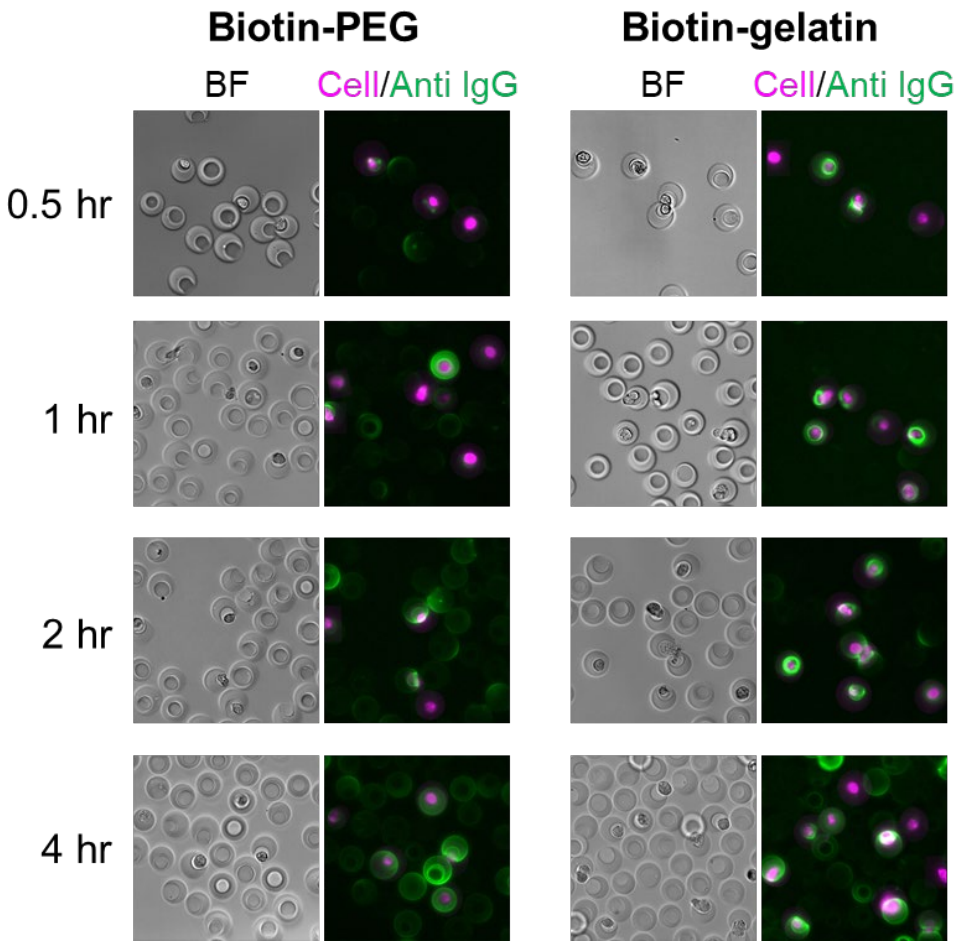

Figure 3-18. Brightfield and fluorescence microscopy images of nanovials and cells after an IgG secretion assay and prior to sorting. Biotin-Gelatin nanovials have signal more concentrated to the cavity and only start showing cross-talk at later time points. Signal on the biotin-PEG nanovials tends to bind more uniformly across the nanovial surface and shows signal on empty nanovials at earlier timepoints.

3.3. Conclusion

To summarize, this study presents a scalable approach to fabricate 3D structured microparticles locally functionalized with gelatin molecules. Our temperature sensitive PEG/gelatin ATPS

system enables generation of multiphase droplets using scalable step-emulsification devices to produce 3D structured particles at rates of 40 million/hr. We believe that using the temperature-induced ATPS system, production rate of >1 billion/hr can be easily achieved by further scaling these devices,[103] and can be potentially scaled further to >1 trillion/hr using other microfluidic approaches.[91] Crescent-shaped nanovial particles fabricated with this approach have an added benefit of gelatin localization inside the nanovial cavity. Harnessing this property enables deterministic loading of cells into the particle cavities and single cell loading at rates higher than expectations based on Poisson statistics. Moreover, the particle cavities act as a shelter for the cells that protects them from shear stress during handling and processing by FACS, improving viability and promoting cellular growth. We further exploit this localization effect to selectively functionalize biotin and capture antibodies to the cavities of the particles enabling single-cell secretion assays with reduced crosstalk. This can be applied beyond producer cells to other cell types such as B cells and T cells where secretion profiling is of importance for the development of antibody and cell-based therapeutics.[104]

Beyond these initial demonstrations, we anticipate broad impact of this technology across other systems. Cavity-containing cell carriers can be used more generally for improved viability of cells sorted using FACS.[105] Particles can be further modified to tune stiffness or extracellular matrix coatings to probe cellular response or provide more relevant cell microenvironments.[18] Due to the scalability of our approach, it unlocks potential utility in other areas such as tissue engineering which typically requires a significantly larger amount of materials. For example, the protective cavity of the particles can be exploited to reduce the harmful effects of shear on *in vivo* delivery of cells for cell therapy applications while also providing a matrix for improved cellular growth.[106] Localization of the binding moieties can further be exploited for the self-assembly of multicell

systems.[107] Aside from the crescent shaped nanovial particles we focus on in this work, this approach can also be applied for scaled fabrication of hollow-shell particles which can be used for studying clonal populations of mammalian cells, microalgae, and bacteria in biologically relevant environments,[87] or act as an immunoprotective layer for allogeneic or xenogeneic cell therapies.

3.4. Materials and Methods

Microfluidic Droplet Generator Fabrication

Step emulsification devices were fabricated as previously described.[18] Master molds were fabricated on silicon wafers using a two-layer photolithography process to define the nozzle heights and reservoir heights. Devices were molded from the masters with PDMS and bonded to glass slides. Devices were treated with 2% trichloro (1H,1H,2H,2H-perfluorooctyl) silane (Sigma) in Novec 7500 (3M) to make the channel surfaces fluorophilic. Flow focusing devices used for the phase diagram studies were fabricated using a similar process.[79]

Identifying Phase Separation Compositions in Bulk

For PEG and gelatin, 5000 Da 4 arm PEG acrylate (Advanced BioChemicals) and cold water fish gelatin (Sigma) were used. Nine different PEG/gelatin solutions comprising PEG at 5, 6, and 7 % w/v and gelatin at 5, 7.5, and 10 % w/v were prepared at room temperature and transferred to a refrigerator maintained at 4 °C. Three sets of conditions were identified in which a single phase of precursor materials transitioned to separated phases upon a temperature reduction from 22 °C to 4 °C.

Identifying Phase Transition Temperature for Different Gelatin Concentrations

30 % w/v PEG, 20 % w/v gelatin and Dulbecco's phosphate-buffered saline (DPBS), respectively, were injected into a flow focusing device with 3 aqueous inlets at different flowrates to precisely control the final compositions of water-in-oil droplets. As an oil phase, 0.5 % v/v Pico-Surf (Sphere Fluidics) in Novec 7500 was used. Five groups of droplets with fixed PEG concentration of 7.5 % w/v and different gelatin concentrations, 1.9, 2.7, 3.6, 4.4, and 5.3 % w/v, were generated. The PEG/gelatin droplets were collected in a downstream reservoir and immersed in a water bath in which the temperature was decreased from 22 °C to 4 °C by 1 °C every 30 minutes to identify at which temperature the droplets undergo phase separation.

Binodal Construction at Two Different Temperatures.

To build the binodal curve for PEG/gelatin droplets at 22 °C, different concentrations of PEG/gelatin droplets were generated using a flow focusing device as described above. Starting from 25 % w/v PEG, the target concentration of PEG was decreased by 0.75 % w/v and at each PEG concentration the minimum gelatin concentration required to yield phase separation in the ATPS droplet were measured. To build the binodal curve for PEG/gelatin droplets at 4 °C the above procedure used for 22 °C was followed but the generated droplets were collected in a downstream reservoir immersed in a 4 °C water bath.

Fabrication of Nanovials with Localized Gelatin

For the dispersed phase, a homogeneous precursor solution with 6.3 % w/v PEG, 4.5 % w/v gelatin and 1.5 % w/v lithium phenyl-2,4,6-trimethylbenzoylphosphinate (LAP) dissolved in DPBS was injected into a parallelized step-emulsifier at 8 μL/min. In some cases, biotinylated PEG, biotinylated gelatin and FITC-gelatin were added to the solution to make Biotin-PEG nanovials,

Biotin-Gelatin nanovials and FITC-labelled nanovials, respectively. The continuous phase comprised 2 % Pico-Surf in Novec 7500 injected at 16 μL/min. Single-phase PEG/gelatin droplets were generated and streamed through a Tygon tube (0.03" I.D., 0.0625" O.D, Murdock) immersed in a 4 °C water bath for temperature induced phase-separation of PEG and gelatin. The length of the tubing was adjusted to ensure full phase separation (~60 cm for 10 min incubation). The stream of phase separated droplets was directed into a PDMS reservoir submerged in the 4 °C water bath and exposed to UV light (200 mW/cm^2) for 1-3 seconds near the outlet region of the reservoir for polymerization. Upon UV exposure, the photocrosslinkable PEG components formed polymer networks while gelatin components remained unpolymerized. The crosslinked particles were collected, and the oil and the gelatin-rich drops were removed in a series of washing steps as previously described (for more details: see Methods in the Supporting Information),[79] yielding crescent-shaped particles with localized gelatin in the surface of cavities.

Fabrication of Nanovials with Uniform RGD Motifs

Nanovials with uniform RGD cell binding motifs were fabricated by injecting PEG and dextran solutions comprising RGD peptides into a flow-focusing device with 2 aqueous inlets as described in our previous study with some modification.[79] A PEG phase solution was prepared with 28.9 % w/w 10 kDa 4-arm PEG-Norbornene (Creative PEGWorks), 2 % w/w LAP, and 0.5 mg/ml Biotin-PEG-thiol (5000 MW, Nanocs) in DPBS. A dextran phase comprised of 11 % w/w 40 kDa dextran (Sigma), 0.7 % w/w dithiothreitol (DTT, Sigma), and 5 mM RGD peptide (Ac-RGDSPGERCGNH2, Genscript) in milli-q water. The PEG and dextran solutions were injected into a flow-focusing device at 0.5 μL/min separately. An oil phase comprised of 0.5% w/w Pico-Surf in Novec 7500 was injected at a rate of 10 μL/min to partition the aqueous phases into

monodisperse water-in-oil droplets. The droplets were exposed to UV light (500 mW/cm^2) for 1-2 seconds near the outlet region of the reservoir for polymerization. The oil and dextran-rich drops were removed using a series of washing steps.

Fabrication of Nanovials with No Binding Motif

Nanovials with no cell binding motifs were fabricated in the same way as RGD nanovials were made, except RGD was excluded from the composition.

Washing Particles

Surfactant oil was first removed by pipetting. A solution of 20% v/v perfluorooctanol (PFO, Sigma) in Novec 7500 and milli-q water were added consecutively to break the emulsions and transfer particles to the aqueous phase. Samples were centrifuged at 2500 ×g for 1 minute and oil phase was removed. Particles were washed with Novec 7500 twice to remove remaining PFO and surfactant. After removing the oil layer with pipetting, the residual oil was washed three times with hexane (Sigma). Samples were then washed three times with 70 % ethanol and then twice with milli-q water to remove gelatin. Particles were sterilized by incubating in 70 % ethanol overnight before use.

Labeling of Gelatin with FITC

50 mg gelatin was dissolved in 5 ml of pH 9.2 sodium carbonate/bicarbonate buffer. 0.25 mg of FITC was dissolved in 250 µL DMSO and slowly added to the gelatin solution. The reaction mixture was stirred for 6 hours in a 4 °C refrigerator. The reaction was quenched by the addition of 15 mg of ammonium chloride (50 mM) and the mixture was stirred for 2 more hours in the same

condition. The solution was dialyzed against milli-q water with 14,000 dalton dialysis tubing for 5 days to remove excess FITC. The FITC-gelatin solution was collected in a 50 mL Falcon tube and stored in a -80 °C freezer and lyophilized.

Cell Culture

CHO DP12 cells (ATCC CRL-12445) were cultured according to manufacture's specifications. Briefly, cells were cultured in DMEM (Invitrogen) supplemented with 10 % fetal bovine serum (FBS, Invitrogen), 1 % penicillin/streptomycin (P/S, Invitrogen), 0.002 mg/ml recombinant human insulin (Sigma), 0.1% Trace Elements A (Fisher Scientific), 0.1% Trace Elements B (Fisher Scientific), and 200 nM Methotrexate (MTX, Sigma).

Seeding Cells on Nanovials

CHO cells were loaded by adding a cell solution to nanovials as described earlier with some modification.[79] Nanovials were stained with AF 350 streptavidin (Fisher Scientific) before use. Nanovials were washed with cell culture media and concentrated in a conical. The amount of concentrated nanovials was calculated to cover the whole well area with a nanovial monolayer, which were 3.2, 4, and 4.8 μL/cm^2 for 36, 45 and 55 μm nanovials, respectively. The proper amount of nanovials were transferred and dispersed in a well plate. CHO cells pre-stained with CellTracker deep red (Invitrogen, C34565) were seeded into the well with the nanovial monolayer at a target cell-to-nanovial ratio. The solution in the well was pipetted multiple times to evenly disperse the cells and particles across the well area. The sample was incubated for 2 hours in a CO_2 incubator to allow cells to adhere to nanovials. In order to remove unattached cells, samples were strained with a 20 μm reversible cell strainer (CellTrics) and washed with "washing buffer" comprised of

0.5 % bovine serum albumin (BSA), 1 % P/S and 0.05 % Pluronic F-127 in DPBS. Since the cell size was smaller than the sieve, unbound cells passed through while the cells bound to nanovials were collected above the strainer. Next, the cell strainer was flipped, placed on top of a 15 mL conical tube and rinsed with the washing buffer to recover the nanovials in a conical tube. The nanovials were centrifuged to remove washing buffer, resuspended in media, and cultured in a CO_2 incubator.

Cell Loading Statistics

Cell loading efficiency was evaluated using custom image analysis algorithms in MATLAB. After cell loading, nanovials were transferred to a well plate and imaged with a fluorescence microscope. The number of total particles were first identified using the particle fluorescence channel by the MATLAB script and the number of cell-laden nanovials were counted manually with detailed information including the number and location of cells within nanovials ($n > 1500$).

Cell Viability Characterization

The viability of cells encapsulated in nanovials was evaluated using a live/dead assay. A staining solution of 2 μM calcein AM solution and 4 μM ethidium homodimer (EthD-1) was prepared in DPBS. Nanovials with cells were first concentrated in a conical tube by centrifugation and supernatant was aspirated. The concentrated nanovials were mixed with the staining solution and incubated for 30 minutes in a CO_2 incubator. The samples were washed with DPBS, centrifuged and transferred to a well-plate for imaging. Live and dead cells were observed by a fluorescence optical microscope where living cells were detected by calcein AM (green fluorescence), and dead cells by EthD-1 (red fluorescence). The number of viable cells was quantified using ImageJ (NIH)

software. Then, the viability rate was obtained by comparing the number of viable cells with total number of cells.

Cell Viability Before and After Sorting.

Cell viability of cells encapsulated in nanovials were characterized before and after sorting compared to unbound cells. CHO cells prestained with CellTracker were loaded in nanovials. Some of the samples were kept as un-sorted samples. The cell-loaded nanovials were sorted directly to a 96-well plate using a FACS machine (Sony SH800) based on the intensity of CellTracker signal at 100-500 events/second. Unbound cells were sorted in the same condition as a control. Viability of cells in different samples were assessed at days 1, 3, and 5 by staining live and dead cells as described above.

Single Cell Secretion Assay and Cross-Talk Characterization. Nanovials were used as a secretion assay platform to capture human IgG targeting IL-8 produced by a CHO cell line (ATCC® CRL-12445™). Biotin modified nanovials were fabricated and CHO cells were seeded on nanovials at a cell-to-particle ratio of 0.8 as described above and cultured for 12 hours prior to the secretion test. Empty nanovials were stained with Alexa Fluor 350 streptavidin to distinguish them from the nanovials loaded with cells. The cell-loaded nanovials were mixed with the blue-stained empty nanovials as a method to characterize cross-talk. This was done in order to ensure signal on empty particles that was measured did not arise from cells that may have detached from the particles during various steps of the assay. All later steps were performed on the mixed nanovials. Mixed nanovials were diluted in a streptavidin solution (0.1 μg/mL streptavidin (Thermo Fisher, 434302) in washing buffer) at a 1:10 ratio and incubated for 10 minutes. The

nanovials were washed with washing buffer three times. A capture antibody solution was prepared by adding 0.02 μg of biotin anti-FC (Thermo Fisher, A18821) per 1 mL of washing buffer. Nanovials were functionalized with capture antibody, biotin anti-FC (Thermo Fisher, A18821), by mixing the nanovial concentrate and the antibody solution at a 1:10 ratio and incubating for 10 min. The nanovials were washed three times and incubated in CHO cell media in a CO_2 incubator for different durations 0.5, 1, 2, and 4 hours to allow cells to secrete IgGs which can bind to capture antibody. "Staining buffer" was made by mixing 10 % FBS, 1 % P/S and 0.05 % Pluronic F-127 in DPBS. The samples were washed three times with staining buffer and incubated in 0.01 μg/mL AF 488 secondary anti-human IgG (Invitrogen, A18821) solution for 30 minutes. The nanovials were washed three times with staining buffer and analyzed using a FACS machine at 100-500 events/second using both 350 nm and 488 nm laser excitation. For 1 and 4 hour incubated samples, nanovials with the top 5 % secretion signal were sorted directly into a 96-well plate pre-filled with culture media and imaged with a microscope. The nanovials before and after sorting were imaged with a fluorescence microscope (Nikon, Eclipse Ti-S). The samples were stained with CellTracker before imaging to aid in visualization of cells. The FCS data files from flow cytometry were analyzed using FlowJo and secretion signals from control and cell-loaded nanovials were compared.

Receiver Operating Characteristic (ROC) Analysis. The signals from cell-loaded nanovials were identified based on their scatter readouts while control empty nanovials were found using their blue signals (Figure S9A). A threshold for anti-IgG signal was set and signals higher than the threshold from empty nanovials and cell-loaded nanovials were considered false positive and true positive signals, respectively. The true positive rates versus false positive rates at fifteen different

cut-off levels were plotted and the area under the ROC curve was calculated using the trapezoidal method.

Chapter 4 Selective Nanovial Capture and Single-Cell Sorting of Antigen-Specific T Cells Based on Cytokine Secretion

4.1. Introduction

In this chapter, we highlight the broad generalizability of the lab-on-a-particle platform by demonstrating the ability to screen and sort primary human T cells as well as genetically engineered CAR-T cells based on cytokine production.

Our immune system is comprised of an incredibly complex network of cells which work in harmony to protect the body from a seemingly limitless array of pathogens and infections. Although the cells which comprise the immune system are drastically different in both form and function, much of their collective behavior is tightly regulated through a shared library of secreted effector proteins. Unfortunately, due to the complexity of accurately detecting and quantifying secreted proteins much of the nuance surrounding such signaling dynamics is still not well understood. Most common laboratory assays measure secretions from bulk cell cultures, providing insights into average production rates across cell populations but obscuring heterogeneity in individual cell function.[20] Newer single-cell technologies are beginning to enable researchers to measure protein production from individual cells massively in parallel, however high costs and the need for specialized end-user expertise have limited broad translation in research settings.

Here, we demonstrate a workflow for the rapid screening and sorting of individual T-cells based on secreted factors that are accumulated on 3D-structured microparticles using a standard fluorescence activated cell sorter (FACS). We adopted the nanovial-based single-cell assay platform, that was utilized for identifying highly productive antibody secreting CHO cells in the previous chapter, to detect and isolate single T cells based on their cytokine production. Cytokines

are small molecular weight proteins or peptides secreted by many cell types, particularly immune system cells, that regulate the duration and intensity of the immune response. We engineer the nanovials with commercially available antibody capture reagents and analyze the production of the cytokines which are tumor necrosis factor-alpha (TNF-α), interferon-gamma (IFN-γ), and interleukin-2 (IL-2) from human primary T cells. To enhance the accuracy of detection, we included a detailed exploration of the optimal sorting conditions to minimize detection noise from non-specific staining.

Next, we expand the findings from this cytokine-based T cell screening platform to screen chimeric antigen receptor (CAR) T cells genetically modified to respond to specific antigen for therapeutic purposes. Engineered T cell therapy is an emerging and effective cancer immunotherapy especially in hematological malignancies, which is accounting for more than half of the cell therapies that are currently under development or in the market.[108] In a CAR-T cell immunotherapy, cells are withdrawn from a patient, genetically engineered to target tumor cells, expanded ex vivo, and finally reinjected into the patient to systemically search for and destroy malignancies. Chimeric antigen receptors are designed by pairing target antigen specific single chain variable fragments (scFvs) with components of the native intracellular T cell receptor signaling apparatus. While simple in principle, the modular design of CARs can become quite complex, with factors such as the affinity of the scFv, the length of the extracellular hinge region, the structure of the transmembrane region and the identities of the intracellular costimulatory domains each having significant impact on the final CAR activity.[109-110] Since treatment works by using the immune system, off-target activity of engineered T cells promotes inappropriate immune responses which can cause severe side effects.[111-112] Therefore, ability to screen individual CAR T cells with the specific antigen-receptor is important to minimize the adverse effects of T cell therapy.

In this study, we targeted to screen universal anti-FITC CAR based on their cytokine secretory function potentially for improved discovery and manufacturing of CAR T cell therapies.[113-114] We engineered nanovials to have FITC molecules as well as capture reagents on the cavities, enabling T cells that express the anti-FITC CAR to bind to FITC molecules on the cavities and the secreted cytokines from them to be captured and analyzed.

The compatibility of lab-on-a-particle technology with standard laboratory equipment yields transformative potential by democratizing functional analysis of single cells for immunotherapy across laboratories.[79, 115] Such highly accessible screening tools will prove imperative for advancing both basic immunological science as well as for informing novel strategies in the development of next generation immune cell therapies.

4.2. Results and Discussion

Improving on our previous work to adhere CHO cells and capture secreted antibodies on nanovials, we have further modified the nanovials to be optimized for T-cell cytokine secretion assay. The assay workflow was similar as in the previous chapter that single cells were loaded on nanovials functionalized with ligands to capture the secretions and they are incubated to enrich the secretions from the cells on the nanovial cavities (Figure 4-1A). However, unlike the adherent cells like CHO which adhered to the gelatin coated cavities of nanovials, suspension cells such as T cells can not adhere to the nanovials through integrin binding. Therefore, we incorporated antibody against CD45, a unique and ubiquitous membrane glycoprotein expressed on almost all hematopoietic cells, as a binding moiety on nanovial cavities for loading non-adherent T cells.[116] To localize the CD45 antibodies on the cavities of nanovials, gelatin coating on nanovials were biotinylated, modified with streptavidin and then labelled with biotinylated anti CD45 as well as with capture

antibodies for TNF-α, IFN-γ, and IL-2 secretions. The cells were selectively bound to the cavities, which is proven in the previous chapter to be required for single cell loading and precise secretion analysis. In addition to introducing the localized cell binding antibodies, cell loading conditions were also optimized to enhance the single cell loading fraction. As cell seeding density increased, both the fraction of nanovials with single-cells and multiplets increased (Figure 4-1B). Testing a range of cell seeding densities, we found that when we load 1.6 cell per particle, we achieve around 16 % of single-cell loading efficiency with multiplets fraction as low as 3 %.

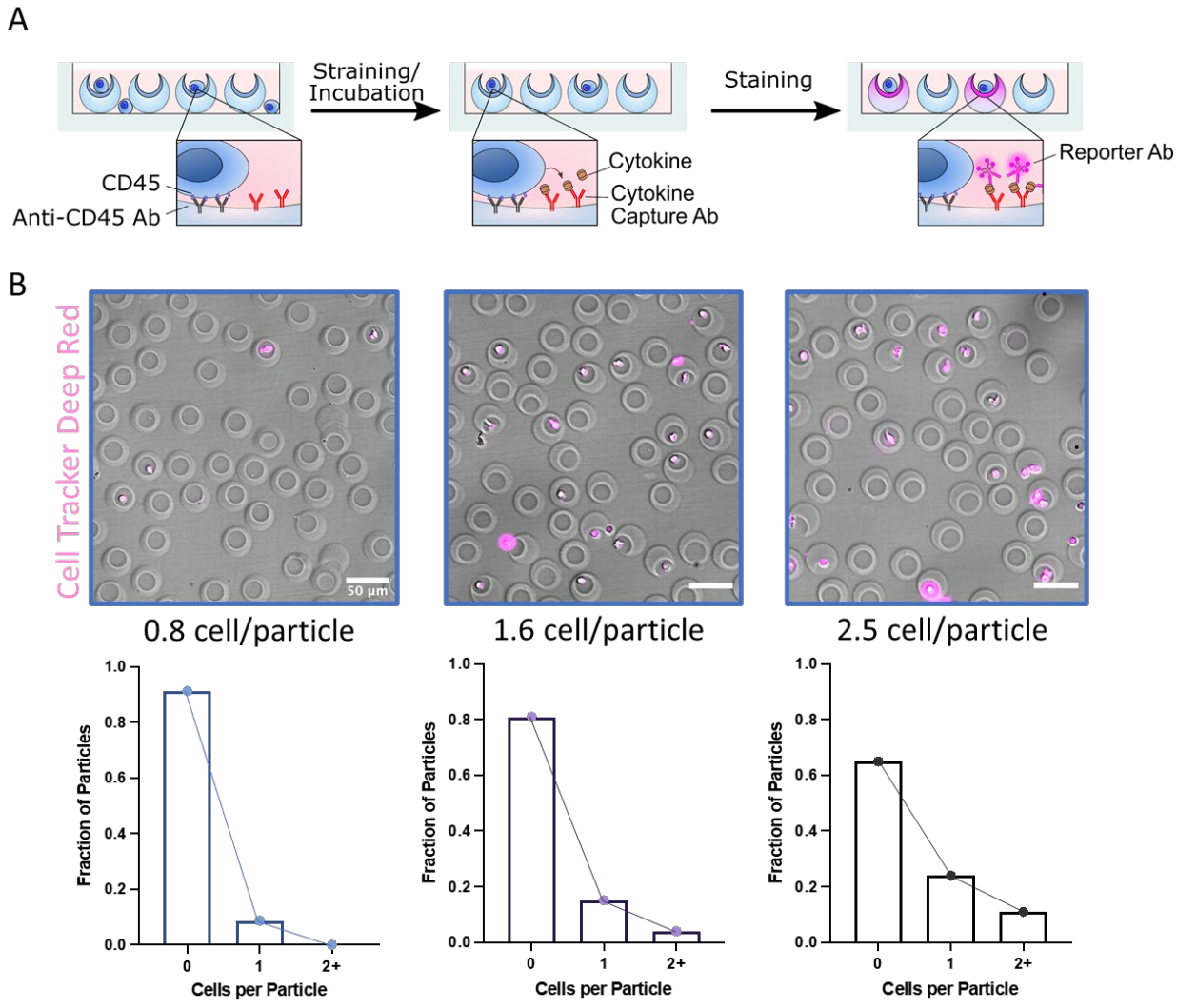

Figure 4-1. Primary T cell loading on nanovials using CD45 antibodies for analysis of cytokine secretion. (A) Overview of cytokine secretion assay for T cells workflow. (B) Characterization of primary T cell loading into nanovials with varying cell seeding density.

Prior to performing single-cell secretion assays, the dynamic range and detection limit of the nanovial cytokine assay were investigated by incubating nanovials with different concentrations of recombinant TNF-α, IFN-γ, and IL-2 then staining with detection antibodies. Nanovials combined with the FACS analysis could detect each cytokine as low as 1-10 ng/ml with four orders of magnitude dynamic range, while the nanovials on fluorescence microscopy has a higher detection limit of 10-100 ng/mL (Figure 4-2). These values are comparable with the other state of the art single cell cytokine detection platforms.[117-118]

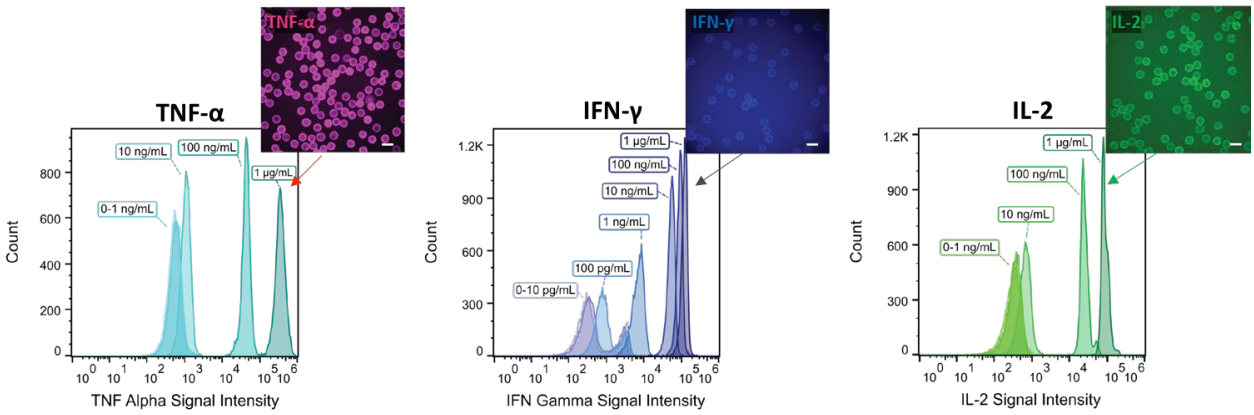

Figure 4-2. Dynamic range of cytokine detection on nanovials. Nanovials were functionalized with capture antibodies targeting either TNF-α, IFN-γ or IL-2 and incubated with varying concentrations of the appropriate cytokine. Samples were analyzed using both fluorescence microscopy and flow cytometry. Cytokines were detectable down to a concentration of 10-100 ng/mL using fluorescence microscopy, or 1-10 ng/mL using FACS depending on the target cytokine.

Next, we demonstrated the cytokine secretion assay with single T cells. Cells are first loaded into the nanovial cavities via CD45 antigen-antibody binding and unbound cells are rinsed to remove background secretions. For cytokines to be produced by primary T cells, the T cells should be activated to make immune response because under normal growth conditions, none or little amount of cytokines are produced. We used phorbol myristate acetate (PMA) and ionomycin to initiate the T cell activation. PMA diffuses through the T cell membrane into the cytoplasm and activates protein kinase C which trigger calcium ion release and mobilization, resulting in a cascade of additional cellular responses mediating T-cell activation.[119]

For 3 hours of T cell incubation with PMA/ionomycin-included culture media, we enrich either TNF-α, IFN-γ, or IL-2 on the nanovial cavities depending on our target cytokines. However, after staining with the fluorescent reporter antibodies, we found significant amount of cell loaded samples showed intracellular cell staining which obscured the signals from soluble cytokine secretions (Figure 4-3A). These false positive signals from the cell stain were observed in the nanovial assays for all three of cytokines. Since the intensity of two different types of staining were comparable, isolating high producer T cells by gating the high signal populations on FACS as done in previous chapter was less effective.

In order to differentiate these two signals, we focused on area versus height metrics. When a sample passes through the laser beam spot in a flow cytometer, it generates scattered light or fluorescence signals, and the flow cytometer quantifies the signals by calculating its height, width, and area (Figure 4-3B). The height of signals is the maximum amount of the output intensity, the width represents the time interval during which the signal occurs, and the area is the integral of the height over width. The signal from cell stain is smaller in width than the secretion signal on

nanovials, having a distinct population in a lower area region than the secretion population on the area versus height plot (Figure 4-A, C, D). Using the strategy, we were able to sort out nanovials with only secretion signal without the cell stain.

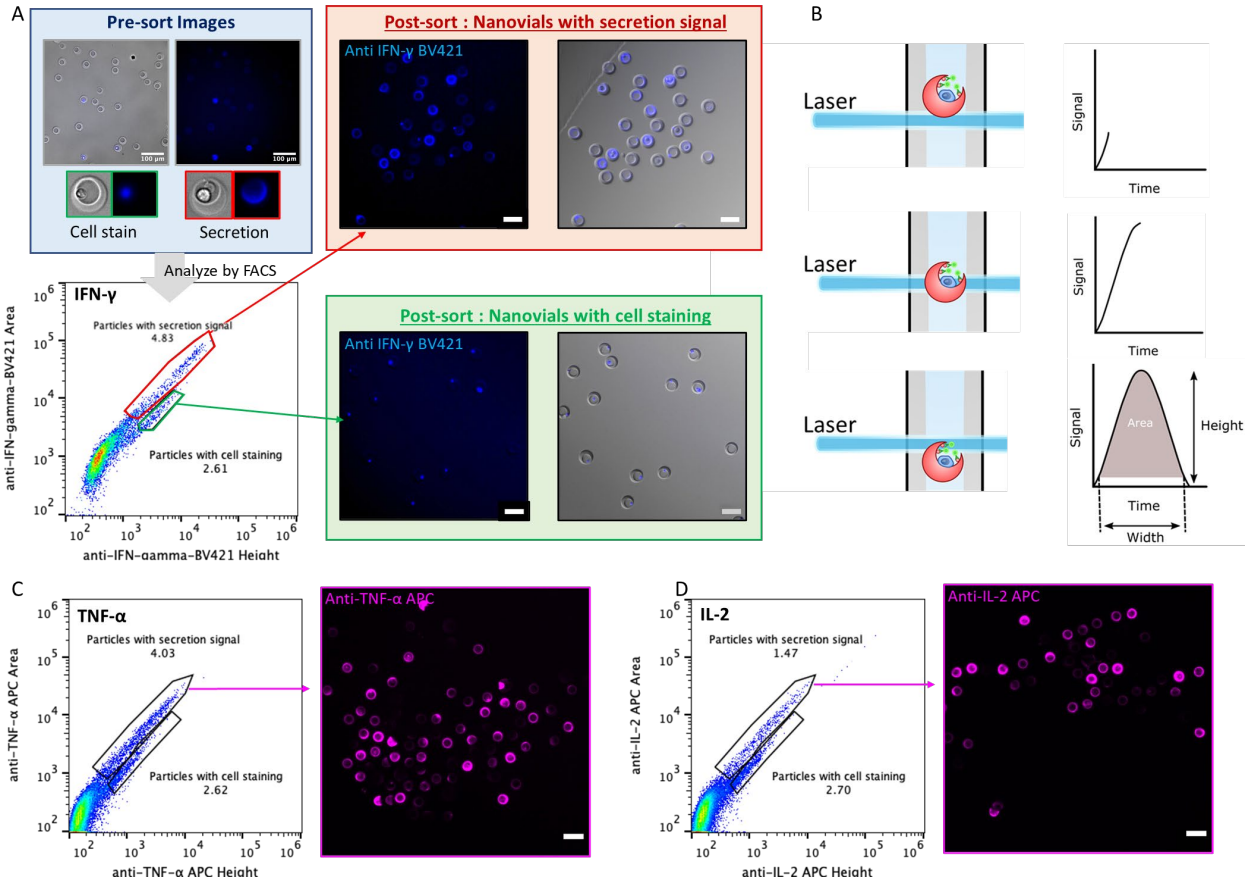

Figure 4-3. Screening and sorting cells with high secretory functions. (A) Gating strategy to differentiate the secreted cytokine signal on wider nanovials from the signal solely from presumably permeabilized or dead cells. (B) A schematic to explain how flow cytometer generates signals when a sample pass through the laser path. The T cells secreting high dose of (C) TNF-α and (D) IL-2 are identified using the gating strategy (scale bar 50 μm).

Furthermore, we found that the cell stain occurs when the membrane of cells on nanovial are damaged and internally stained with detection antibody and we exploited it to eliminate the cell stain population. We multiplexed secretion signals with signals from a non-invasive, non-toxic dye that stains intact cell membrane, calcein AM. When live cells take up calcein AM, the ester groups in calcein AM gets hydrolyzed into fluorescent calcein by intracellular enzyme and the dye is retained in the cytosol and not bound to DNA. It has been proved that calcein AM at its working concentration does not induce any cell stress or death upon exposure to the dye and after exposure to calcein AM, cells were able to proliferate as efficiently as the controls.[120] As we gated the calcein AM positive population, we could remove the cell stain population on the area versus height plot. Targeting TNF-α and IFN-γ secretions from T cells, we could split the secretion signal population into three based on their secretion levels and sorted each group separately (Figure 4-4).

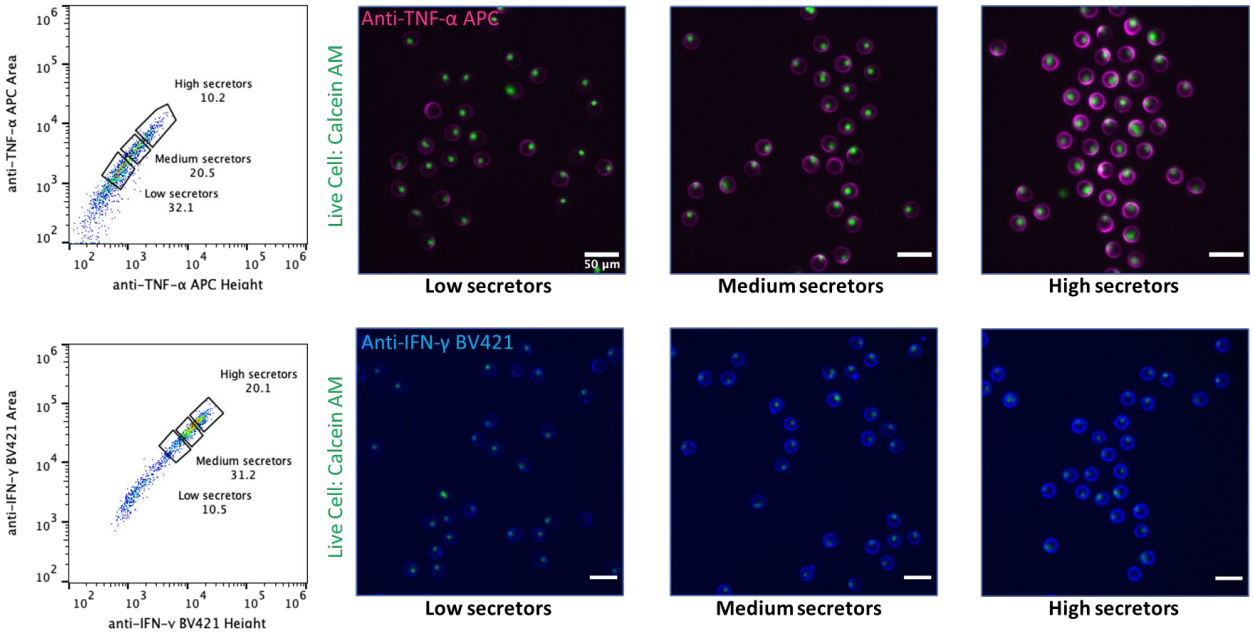

Figure 4-4. Selecting T cells based on their cytokine secretion levels. We multiplexed secretion signals with calcein AM to exclude the cell stain as well as to select viable cells. High, medium,

and low secretor T cells for TNF-α and IFN-γ are identified and sorted successfully (scale bar 50 μm).

Next, we performed multiplexed profiling of TNF-α and IFN-γ. We located the four populations that secrete either or both of the cytokines on the TNF-α versus IFN-γ plot by comparing with the signals from negative control samples (Figure 4-5). By gating these populations, we were able to sort and recover the cells that secrete each cytokine as well as polyfunctional cells secreting multiple cytokines which represent only 13.4 % of the total population.

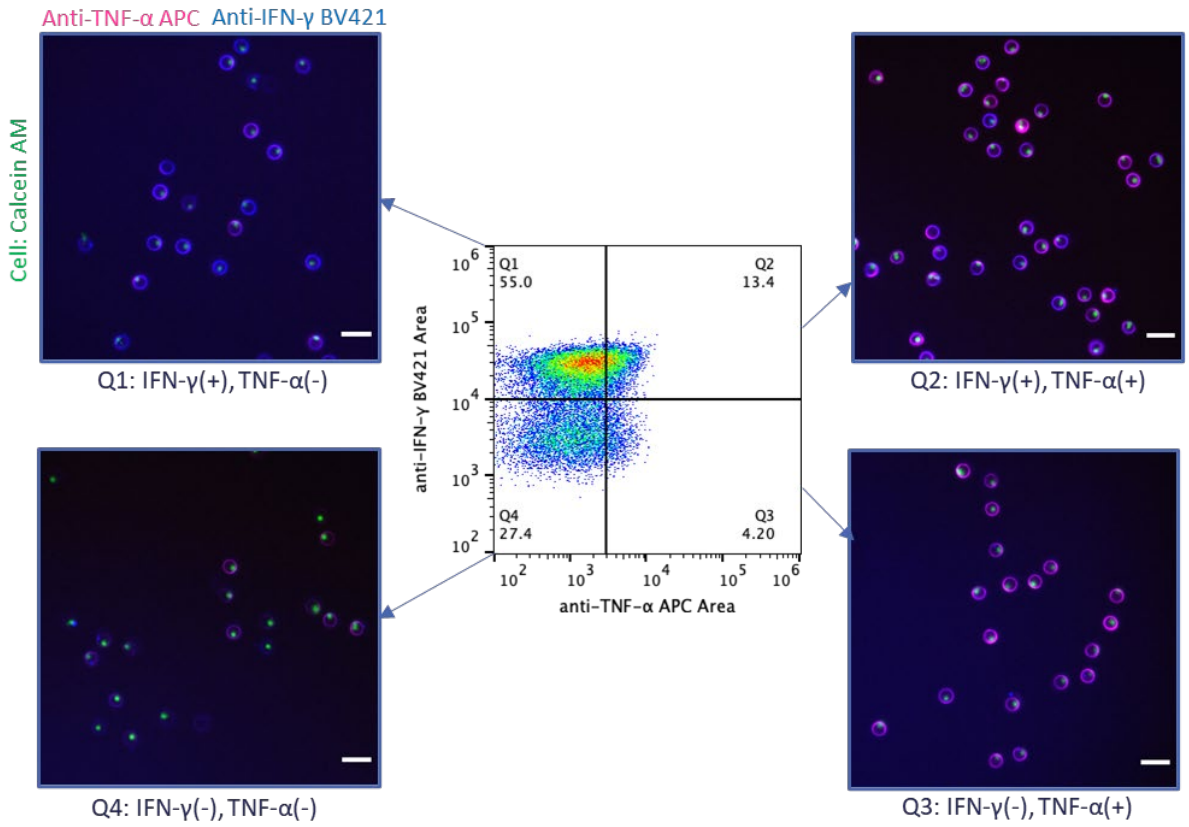

Figure 4-5. Multiplexed profiling of TNF-α and IFN-γ secretion of primary T cells using PMA/ionomycin as an activator (scale bar 50 μm).

We demonstrated that we could sort T cells based on their secretory functions using PMA/ionomycin as activating agents. We further appled our nanovial based cytokine assay platform to identify and sort antigen specific T cells such as CAR T cells.

In this study, we engineered Jurkat cells (a CD4+ T cell leukemia line) and peripheral blood mononuclear cells (PBMCs) with anti-FITC CAR which is designed for the T cells not to directly recognize antigen on target cells but recruited to effector cells through a bispecific small molecule (Figure 4-6A). This universal anti-FITC CAR is beneficial in that they can target various antigens by using bispecific anti-tumor antibodies conjugated with FITC. Therefore, antigenically heterogeneous tumors comprised of different tumor clones can be eradicated by a single anti-FITC CAR T cell.[121]

Nanovials can be functionalized with target antigens as well as the capture antibodies targeting the cytokines of interests. The antigens enable selective binding to CAR T cells with the specific receptors, and individual clones demonstrating enhanced cytokine production could be recovered for improved discovery and manufacturing of cell therapies or sequenced to identify their constructs.

Prior to performing nanovial assays, we first confirmed that the engineered anti-FITC CAR T cells secrete cytokines upon interacting with FITC nanovials using commercial ELISA kits. FITC nanovials are prepared by conjugating FITC molecules to gelatin molecules on nanovials. We cultured 1.5 million/mL of anti-FITC CAR Jurkats in different activation conditions, including incubation with no activator, PMA/ionomycin and nanovials that were functionalized with different concentrations of FITC solutions, 0, 0.25, and 2.5 mg/mL. After 12 hours of incubation, we collected the conditioned media to measure the secretion of cytokines, either TNF-α, IFN-γ or IL-2 (Figure 4-6B). The ELISA results showed that when cultured with FITC nanovials, the

Jurkats became activated and secreted IL-2, but not TNF-α and IFN-γ, while jurkats were activated by PMA/ionomycin secreted IFN-γ and IL-2. The amount of FITC molecules on nanovials affect the activation of jurkats. The cells incubated with nanovials labelled with 0.25 and 2.5 mg/mL FITC solutions showed 15.5 pg/mL and 62.5 pg/mL of IL-2 secretions, respectively, which corresponds to on average 10.3 pg and 41.6 pg of IL-2 secretions per one million cells, showing the presence of more FITC molecules enhances the secretion amount from Jurkats.

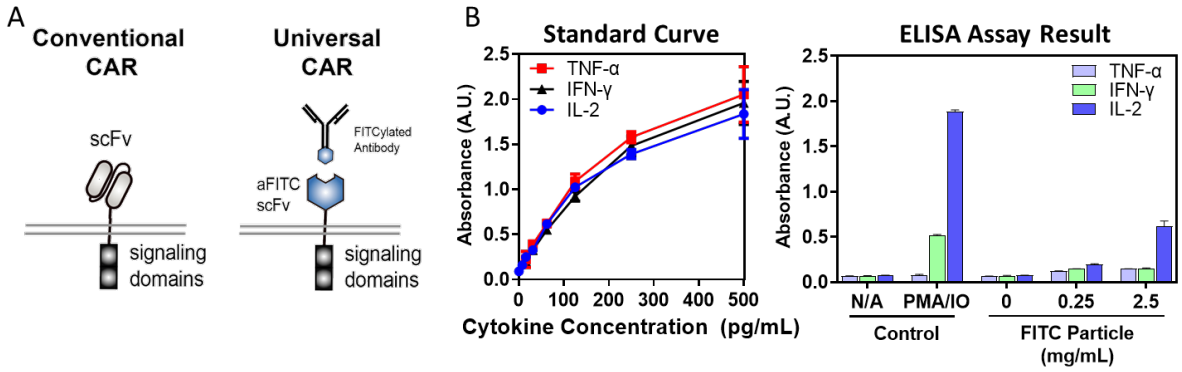

Figure 4-6. The secretory function of CAR T cells designed to specifically bind to FITC and become activated. (A) Schematic representation of universal anti-FITC CAR constructs as compared to conventional CAR constructs. (B) Cytokine secretion analysis of anti-FITC CAR Jurkats cultured with different activating conditions using a commercial ELISA kit.

Since FITC conjugation and biotinylation of gelatin, which is required to functionalize nanovials with cytokine capture antibodies, occurs on the same functional groups on gelatin polymer chain (Figure 4-7A), we assessed the trade-off between FITC- and biotin-conjugation on nanovials using microscopy and flow cytometry. Nanovials were first conjugated with FITC by incubating them in a FITC solution for 2 hours at room temperature and then biotinylated with 5 mg/mL biotin solution for 15 hours at 4 ºC. Sweeping the concentration of FITC solution from 0 to 2.5 mg/mL,

we found that the nanovials with higher FITC concentrations have lower biotin concentrations, which was proven by streptavidin-biotin staining (Figure 4-7B). However, when we tested the IL-2 detection of the non-FITC and FITC nanovials that were functionalized with IL-2 capture antibodies, the detection signals from 10-1000 ng/mL of IL-2 solution only slightly decreased by using the nanovial with FITC molecules (Figure 4-7C). Therefore, considering that the nanovials with higher FITC concentrations provide significantly higher activation for anti-FITC CAR T cells, we decided to use 2.5 mg/mL FITC solutions to conjugated FITC molecules to nanovials for the rest of the study.

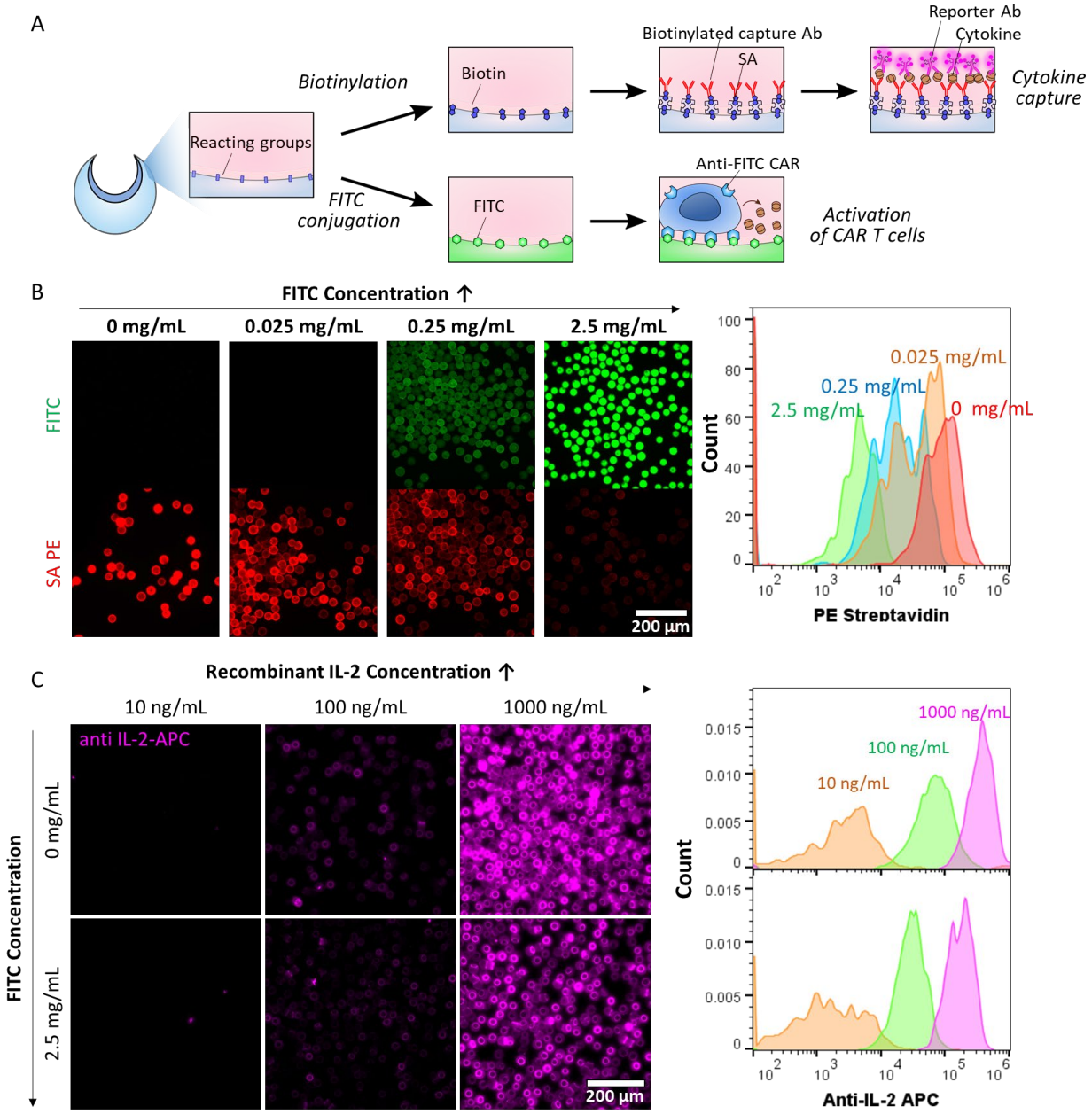

Figure 4-7. Trade-off between biotinylation and FITC conjugation of nanovials. (A) Schematic to explain the trade-off between biotinylation and FITC-conjugation on nanovials. (B) The increase in FITC-conjugation of nanovials reduced the biotinylation of nanovials, proven by the lower streptavidin staining (R-phycoerythrin, PE) in highly FITC-conjugated nanovials. (C) Two groups of the nanovials, the blank nanovials whose reacting groups were solely functionalized

with biotin and eventually capture antibodies and the FITC nanovials which partially shared their reacting groups for FITC conjugation, were incubated with different concentration of standard IL-2 and subsequently stained with reporter antibodies (APC). The increase in FITC concentration on nanovials slightly decreased the dynamic range of nanovial assay because of the reduced biotinylation.

After the optimization of FITC nanovials, anti-FITC CAR Jurkats were loaded on to the FITC nanovials (Figure 4-8A). Because of the affinity between the FITC molecules on the nanovials and the anti-FITC CARs on the loaded cells, cells were loaded without incorporating additional cell binding motifs (e.g. anti-CD45) to nanovials. We explored the cell to particle ratio to find a cell loading condition that gives high single-cell loading but low cell multiplets (Figure 4-8B). To decide the incubation duration for cytokine secretion, we cultured the anti-FITC CAR Jurkats in various activation conditions, including incubation with no activator, PMA/ionomycin and FITC nanovials (Figure 4-8C). We found that in all activating conditions the cells started secretion between 3- and 5-hours post activation. For the cells activated by FITC particle (2.5 mg/mL FITC condition), there was little increase in the secretion between 7- and 15-hours post activation. While the secretion signals from PMA/ionomycin triggered samples stopped increasing after 5-7 hours-post activation, we assumed that it could be explained that the secretion level reached over the maximum detection range and the signal was saturated.

After 12 hours of incubation, the cell-loaded nanovials were washed and labelled with the detection antibodies (Figure 4-8D). Under a fluorescence microscope, we found localized bright signals on the cavities of nanovials which demonstrates that the FITC nanovial activated the loaded CAR T cells to secrete IL-2 and captured the secretions on their cavities. When manually counted, 0. 83 ±

0.17 % of the total nanovials, which was equivalent to 4.01 ± 1.24 % of the total cell-loaded nanovials, showed secretion signals. We attributed this rarity of the signals to the low cytokine secretions of Jurkats, which has been previously reported, and potential low transduction efficiency.

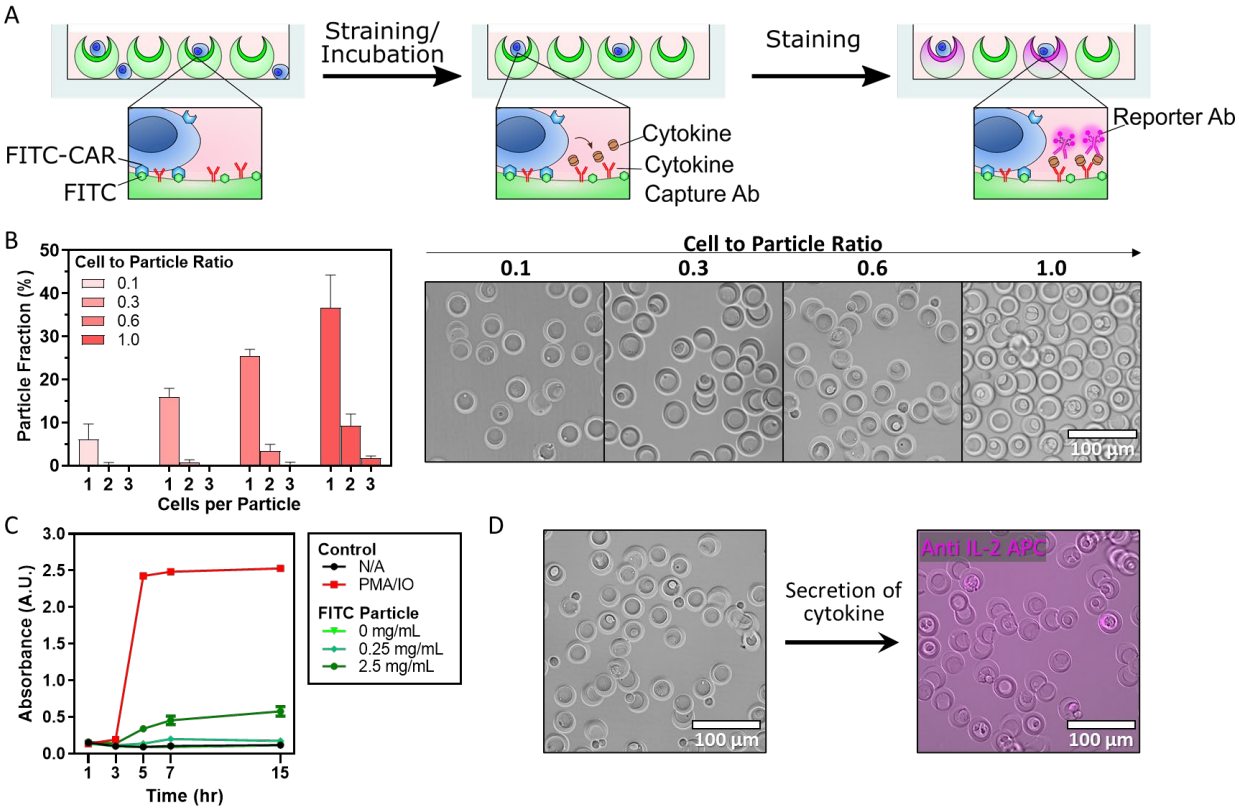

Figure 4-8. Nanovial-based cytokine secretion assay for anti-FITC CAR T cells. (A) Schematic overview of cytokine secretion assay for anti-FITC CAR T cells workflow. (B) Characterization of anti-FITC CAR jurkats cell loading into nanovials with varying cell seeding density. (C) ELISA was performed to assess the time dependence of IL-2 secretion from anti-FITC CAR jurkats and to decide the proper incubation duration for nanovial secretion assay. (D) After 12 hours of incubation, IL-2 secretions (APC) were captured on some of the cell-filled nanovials.

In addition to the Jurkats transduced with the FITC CAR, we expanded the study to PBMCs transduced with anti-FITC CARs which secrete higher levels of TNF-α and IFN-γ and a lower amount of IL-2 (Figure 4-9A). We followed the same workflow as for anti-FITC CAR Jurkats in terms of particle preparation, cell loading and capturing cytokines on the nanovials, but targeted TNF-α and IFN-γ instead of IL-2. We prepared nanovials functionalized with capture antibodies against either of TNF-α or IFN-γ and a mixture of both for multiplexed secretomic analysis. Individual PBMCs were bound to the inner surface of nanovials, and secretion assays were performed to assess their production of the cytokines. PBMCs were activated by FITC molecules on nanovials and incubated for a period of 12 hours to generate signal. After incubation and subsequent staining, both the TNF-α- and IFN-γ-targeting nanovials showed bright fluorescent signals along the edge of cell-filled nanovial cavities. Flow cytometry analysis revealed that IFN-γ staining led to some cell staining populations, but we could use the area versus height parameters to differentiate them from the cytokine secretion signal populations as done for primary T cells cytokine assays (Figure 4-9B). Additionally, we have been able to detect the production of both IFN-γ and TNF-α from single viable CAR-T cells. Secreting cells were easily identified using flow cytometry and fluorescence microscopy and could be possibly enriched via standard FACS sorting (4-9 C).

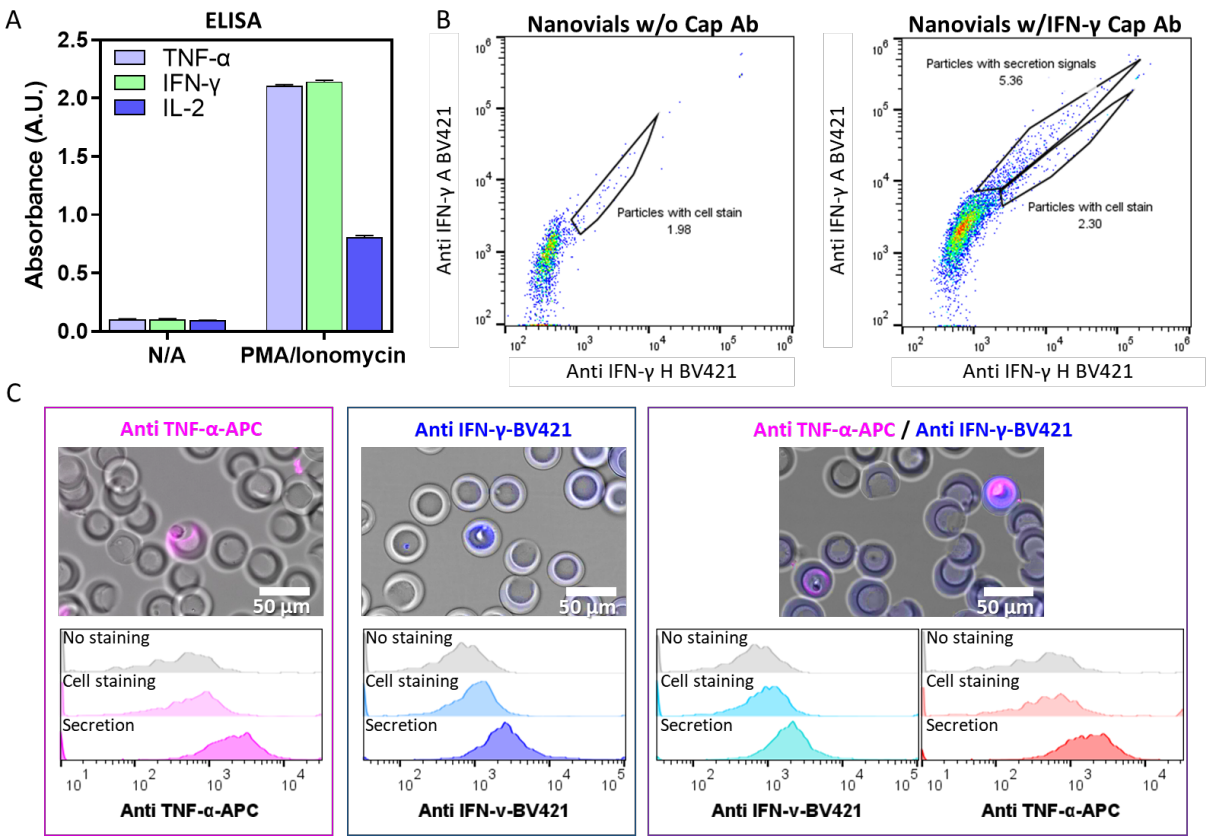

Figure 4-9. Nanovial-based cytokine secretion assay for anti-FITC CAR PBMCs. (A) ELISA tests proved that anti-FITC CAR PBMCs secrete TNF-α (APC) and IFN-γ (brilliant violet 421) and lower dose of IL-2. (B) We could differentiate the secretion signals from the cell stain signals by applying the same gating strategy that we used for primary T cells. (C) After incubation and subsequent staining, nanovials with either of TNF-α and IFN-γ capture antibodies showed bright fluorescent signals on the nanovial cavities. The nanovials with the mixture of both capture antibodies showed multiplexed signals as well as the single signals of each cytokine.

4.3. Conclusion

Our technology can quantitatively screen, and sort millions of viable cells based on cytokine secretion, which will aid in discovery of TCRs, CARs, and surface markers involved in specific

immune responses. It may also prove useful for analysis of unwanted phenomena, such as generation of consecutive signaling from CAR constructs in the absence of target antigen (tonic signaling), providing a route to select out CAR designs that will result in rapid cell exhaustion. We can further investigate the transcriptome of sorted polyfunctional T cells to uncover drivers of this phenotype, potentially improving upon the current paradigm of cell therapies.

4.4. Materials and Methods

Culture of Primary T cells

Trima filters were purchased from the UCLA virology core and eluted to recover concentrated volumes of whole blood. T cells were isolated from the trima filter eluent using the RosetteSepTM Human T Cell Enrichment Cocktail (STEMCELL Technologies) according to manufacturer instructions and immediately frozen at a concentration of 1×10^7 cells/mL of freezing media. Before analysis, each aliquot of T cells was rapidly thawed and transferred into pre-warmed ImmunoCultTM-XF T Cell Expansion Media supplemented with 25 μL/mL ImmunoCultTM Human CD3/CD28 T cell activatior, and 50 IU/mL IL-2 at a final concentration of 1×10^6 cells/mL. Cells were passaged twice a week. Culture media was replenished with 50 IU/mL of IL-2 every 2 days. Cells were cultured in a sterile incubator at 37ºC and 5% CO^2 for up to 3 weeks before thawing a fresh vial of cells.

Engineering Anti-FITC CAR Jurkats

Jurkat T cells were maintained in complete RPMI-1640 media as described above. For transduction, replication-incompetent lentivirus was packaged via PEI transfection of HEK293FT cells in a 6 well plate with lentiviral packaging and envelope plasmids (pDelta, Vsvg, and pAdv)

and the anti-FITC CAR construct in a pHR lentiviral expression vector. Virus-containing supernatant was collected 3 days post-transfection and spun down to remove cell debris. 5×10^5 Jurkat cells were infected with 500 uL – 1 mL of anti-FITC CAR viral supernatant then diluted with 4 mL complete RPMI media 24 hr post infection. Four days after infection, transduced Jurkat cells were analyzed via flow cytometry to assess transduction efficiencies and anti-FITC CAR expression via mCherry or myc tag staining.

Engineering Anti-FITC CAR PBMCs

Anonymized whole peripheral blood was obtained from Boson Children's hospital and primary CD8+ T cells were isolated using the STEMCELL CD8+ Enrichment cocktail and RosetteSep system. CD8+ T cells were cryopreserved in 90 % human Ab serum (Valley Biomedical) and 10 % DMSO. Two days prior to transduction, T cells were thawed and activated with ImmunoCult human CD3/CD28 T cell activator (STEMCELL).

For transduction, replication-incompetent lentivirus was packaged via PEI transfection of HEK293FT cells in a T175 flask with lentiviral packaging and envelope plasmids and the anti-FITC CAR construct. One day after transfection, the HEK293FT culture media was removed and replaced with prewarmed FreeStyle 293 expression medium (Gibco) supplemented with 100 U/mL penicillin, 100 μg/mL streptomycin, 1 mM sodium pyruvate, and 5 mM sodium butyrate. Beginning 48 hours post transfection, viral supernatant was collected and replenished with fresh FreeStyle 293 media for 3 days. Then, the harvested lentivirus was concentrated using a 40 % (w/v) PEG-8000 and 1.2 M NaCl solution overnight and spun down for 1 hr at 1600 ×g at 4°C.

One day prior to transduction, T cells were activated with Immunocult Human CD3/CD28 T cell Activator according to manufacturer instructions. Additionally, a non-TC treated 6-well plate was

coated with 20 µg/mL of Retronectin in PBS and left at 4°C overnight. For primary T cell transduction, all of the concentrated virus collected from one T175 flask was spun onto one well of the Retronectin coated plate for 90 min at 1200 ×g. The viral supernatant was then removed and 4 mL of activated primary CD8+ T cells was added and incubated for 72 hrs at 37 °C before moving to a T75 flask for expansion. Transduction efficiencies were analyzed via mCherry expression or myc tag staining.

Nanovial FITC Conjugation

Nanovial was spun down to a pellet. FITC solution is made by dissolving 1 mg of Fluorescein isothiocyanate isomer I (Sigma F7250) into a solution made of 200 µl of DMSO and 200 µl of sodium bicarbonate buffer. 25 µl of nanovial was incubated with 50 µl of FITC solution for 1 hour at room temperature on a rotator. After an hour, the nanovials are washed 5 times with washing buffer.

Biotinylation of Nanovials

Biotin solution was prepared by dissolving 5 mg of sulfo-NHS-Biotin (ApexBio) into 1.1 mL of DPBS. 10 mg of gelatin in nanovials was mixed with 330 mL of biotin solution and incubated in a 4 ºC refrigerator over 12-18 hours. After incubation, nanovials were triple washed with washing buffer.

Primary T Cell Cytokine Secretion Assay

Nanovials were used as a secretion assay platform to capture cytokines produced by primary T cells. For primary T cells, biotin nanovials were incubated in 0.2 mg/mL streptavidin for 30

minutes and then washed three times. The streptavidin labelled nanovials were labelled with biotinylated-anti CD45 antibody and biotinylated cytokine capture antibodies either for TNF-α, IFN-γ, and IL-2 for 30 minutes. T cells were seeded on nanovials at an appropriate ratio between cells and particles and incubated for 1 hour. The cell loaded nanovials were rinsed on top of the 27 μm strainer to remove unbound cells and resuspended to a well plate (12 μl of nanovial pellet per well in a 24 well-plate).

The culture media was supplemented with 100 ng/mL phorbol 12-myristate 13-acetate (PMA) and 2.5 μM ionomycin, and cells were incubated for 3 hours to accumulate the secretions on the nanovials. After the incubation, the sample was recovered in an Eppendorf tube and washed with washing buffer three times. The captured secretions on nanovials were labelled with detector antibodies for the target cytokines for 30 minutes and then washed three times. The secretion signals were analyzed using microscopy and flowcytometry.

Anti-FITC CAR T Cell Cytokine Secretion Assay

Nanovials were used as a secretion assay platform to capture cytokines produced by CAR T cells. For the CAR T cell loading, FITC and biotin-labelled nanovials were incubated in 0.2 mg/mL streptavidin for 30 minutes and then washed three times. Anti-FITC CAR T cells were seeded on FITC nanovials at an appropriate ratio between cells and particles and incubated for 1 hour. The cells adhered to nanovials through FITC and FITC anyibody interaction. The cell loaded nanovials were rinsed on top of the 27 μm strainer to remove unbound cells and resuspended to a well plate (12 μl of nanovial pellet per well in a 24 well-plate). With no need to add any other activation agent, the anti-FITC CAR T cells were stimulated by incubating the cells on FITC nanovials. After 12 hours of incubation, the sample was recovered in an Eppendorf tube and washed with washing

buffer three times. The captured secretions on nanovials were labelled with detector antibodies for the target cytokines for 30 minutes and then washed three times. The stained samples were analyzed with fluorescent microscopy and flow cytometry.

Chapter 5 Concluding Remarks

The focus of this work was developing multifunctional hydrogels and applying them to overcome the challenges of the existing microfabrication techniques such as 3D bioprinting and microfluidics. Microfabrication techniques are poised to revolutionize the next generation of biotechnology, as it can interfere and manipulate the interactions between materials and biological systems in microscale. Cells sense and respond to the properties of biomaterials such as stiffness, adhesive ligands, and geometry. Understanding this complex microenvironment and their impact on cells and, more importantly, optimizing these properties would help resolving current challenges in micro fabrication. In this work, we investigated this interaction at multi-cellular tissue level to single cell level using two microfabrication methods 3D bioprinting and microfluidics.

In Chapter 2, we developed a highly biocompatible and elastic bioink for fabrication of complex biomimetic structures such as vascularized cardiac tissue constructs. The 3D bioprinting of soft tissues has been challenging primarily due to the lack of suitable bioinks. To address these shortcomings, we used recombinant human tropoelastin as a novel bioink with high printability, biocompatibility, biomimicry, and proper mechanical properties. We successfully bioprinted vascularized cardiac constructs using two-nozzles, which mimic key functions of vascularized cardiac tissue *in vivo* such as endothelium barrier function and spontaneous beating of cardiac cells.

Furthermore, the printed construct elicited minimal inflammatory responses, and were shown to be efficiently biodegraded *in vivo* when implanted subcutaneously in rats

The nanovial-based assay platform highlighted in chapters 3 and 4 of this work is a novel technology that has the potential to transform the study of single cell secretions across numerous applications. In addition to the assessment of antibody production from producer cell lines such as CHO-DP 12, we have also been able to detect various cytokines (TNF-α, IFN-γ, and IL-2) produced by primary T cells and CAR T cells. We proved that using this platform, we could detect the cytokines down to 1 ng/mL, and sort high secreting cell clones out of a background of non-producers.

The new tools of microfabrication are opening up opportunities for biotechnology, refashioning strategies and perspectives how we approach molecular, cellular and tissue engineering. Overall, we believe the work described here demonstrates how microfabrication techniques can advance the existing technologies, providing multiple options to innovate related studies.

Chapter 6 Reference

1. Park, H.; Cannizzaro, C.; Vunjak-Novakovic, G.; Langer, R.; Vacanti, C. A.; Farokhzad, O. C., Nanofabrication and microfabrication of functional materials for tissue engineering. *Tissue engineering* **2007,** *13* (8), 1867-1877.
2. Verhulsel, M.; Vignes, M.; Descroix, S.; Malaquin, L.; Vignjevic, D. M.; Viovy, J.-L., A review of microfabrication and hydrogel engineering for micro-organs on chips. *Biomaterials* **2014,** *35* (6), 1816-1832.
3. Rahmati, M.; Silva, E. A.; Reseland, J. E.; Heyward, C. A.; Haugen, H. J., Biological responses to physicochemical properties of biomaterial surface. *Chemical Society Reviews* **2020,** *49* (15), 5178-5224.
4. Moroni, L.; Boland, T.; Burdick, J. A.; De Maria, C.; Derby, B.; Forgacs, G.; Groll, J.; Li, Q.; Malda, J.; Mironov, V. A., Biofabrication: a guide to technology and terminology. *Trends in biotechnology* **2018,** *36* (4), 384-402.
5. Fonseca, A. C.; Melchels, F. P.; Ferreira, M. J.; Moxon, S. R.; Potjewyd, G.; Dargaville, T. R.; Kimber, S. J.; Domingos, M., Emulating human tissues and organs: a bioprinting perspective toward personalized medicine. *Chemical Reviews* **2020,** *120* (19), 11093-11139.
6. Whitesides, G. M.; Ostuni, E.; Takayama, S.; Jiang, X.; Ingber, D. E., Soft lithography in biology and biochemistry. *Annual review of biomedical engineering* **2001,** *3* (1), 335-373.
7. Ostuni, E.; Chen, C. S.; Ingber, D. E.; Whitesides, G. M., Selective deposition of proteins and cells in arrays of microwells. *Langmuir* **2001,** *17* (9), 2828-2834.
8. Yeh, J.; Ling, Y.; Karp, J. M.; Gantz, J.; Chandawarkar, A.; Eng, G.; Blumling Iii, J.; Langer, R.; Khademhosseini, A., Micromolding of shape-controlled, harvestable cell-laden hydrogels. *Biomaterials* **2006,** *27* (31), 5391-5398.
9. Rivest, C.; Morrison, D.; Ni, B.; Rubin, J.; Yadav, V.; Mahdavi, A.; Karp, J.; Khademhosseini, A., Microscale hydrogels for medicine and biology: synthesis, characteristics and applications. *Journal of Mechanics of materials and structures* **2007,** *2* (6), 1103-1119.
10. Simon, E. M., NIH Phase I Final Report: Fibrous Substrates for Cell Culture (R3RR03544A). ResearchGate: 2017.
11. Azimi, B.; Maleki, H.; Zavagna, L.; De la Ossa, J. G.; Linari, S.; Lazzeri, A.; Danti, S., Bio-based electrospun fibers for wound healing. *Journal of Functional Biomaterials* **2020,** *11* (3), 67.
12. Gluais, M.; Clouet, J.; Fusellier, M.; Decante, C.; Moraru, C.; Dutilleul, M.; Véziers, J.; Lesoeur, J.; Dumas, D.; Abadie, J., In vitro and in vivo evaluation of an electrospun-aligned microfibrous implant for Annulus fibrosus repair. *Biomaterials* **2019,** *205*, 81-93.
13. Zamani, M.; Prabhakaran, M. P.; Ramakrishna, S., Advances in drug delivery via electrospun and electrosprayed nanomaterials. *International journal of nanomedicine* **2013,** *8*, 2997.
14. Duffy, D. C.; McDonald, J. C.; Schueller, O. J.; Whitesides, G. M., Rapid prototyping of microfluidic systems in poly (dimethylsiloxane). *Analytical chemistry* **1998,** *70* (23), 4974-4984.
15. Si, L.; Bai, H.; Rodas, M.; Cao, W.; Oh, C. Y.; Jiang, A.; Moller, R.; Hoagland, D.; Oishi, K.; Horiuchi, S., Human organ chip-enabled pipeline to rapidly repurpose therapeutics during viral pandemics. **2020**.

16. Si, L.; Bai, H.; Rodas, M.; Cao, W.; Oh, C. Y.; Jiang, A.; Moller, R.; Hoagland, D.; Oishi, K.; Horiuchi, S., A human-airway-on-a-chip for the rapid identification of candidate antiviral therapeutics and prophylactics. *Nature biomedical engineering* **2021,** *5* (8), 815-829.
17. Mohamed, M. G.; Ambhorkar, P.; Samanipour, R.; Yang, A.; Ghafoor, A.; Kim, K., Microfluidics-based fabrication of cell-laden microgels. *Biomicrofluidics* **2020,** *14* (2), 021501.
18. de Rutte, J. M.; Koh, J.; Di Carlo, D., Scalable high‐throughput production of modular microgels for in situ assembly of microporous tissue scaffolds. *Advanced Functional Materials* **2019,** *29* (25), 1900071.
19. Klein, A. M.; Mazutis, L.; Akartuna, I.; Tallapragada, N.; Veres, A.; Li, V.; Peshkin, L.; Weitz, D. A.; Kirschner, M. W., Droplet barcoding for single-cell transcriptomics applied to embryonic stem cells. *Cell* **2015,** *161* (5), 1187-1201.
20. Lagus, T. P.; Edd, J. F., A review of the theory, methods and recent applications of high-throughput single-cell droplet microfluidics. *Journal of Physics D: Applied Physics* **2013,** *46* (11), 114005.
21. Bageritz, J.; Raddi, G., Single-cell RNA sequencing with Drop-Seq. In *Single Cell Methods*, Springer: 2019; pp 73-85.
22. Klein, A. M.; Macosko, E., InDrops and Drop-seq technologies for single-cell sequencing. *Lab on a Chip* **2017,** *17* (15), 2540-2541.
23. Freytag, S.; Tian, L.; Lönnstedt, I.; Ng, M.; Bahlo, M., Comparison of clustering tools in R for medium-sized 10x Genomics single-cell RNA-sequencing data. *F1000Research* **2018,** *7*.
24. Murphy, S. V.; Atala, A., 3D bioprinting of tissues and organs. *Nature biotechnology* **2014,** *32* (8), 773.
25. Clyne, A. M.; Swaminathan, S.; Lantada, A. D., Biofabrication strategies for creating microvascular complexity. *Biofabrication* **2019,** *11* (3), 032001.
26. Kolesky, D. B.; Homan, K. A.; Skylar-Scott, M. A.; Lewis, J. A., Three-dimensional bioprinting of thick vascularized tissues. *Proceedings of the national academy of sciences* **2016,** *113* (12), 3179-3184.
27. Kolesky, D. B.; Truby, R. L.; Gladman, A. S.; Busbee, T. A.; Homan, K. A.; Lewis, J. A., 3D bioprinting of vascularized, heterogeneous cell‐laden tissue constructs. *Advanced materials* **2014,** *26* (19), 3124-3130.
28. Zhang, Y.; Kumar, P.; Lv, S.; Xiong, D.; Zhao, H.; Cai, Z.; Zhao, X., Recent advances in 3D bioprinting of vascularized tissues. *Materials & Design* **2021,** *199*, 109398.
29. Dai, X.; Liu, L.; Ouyang, J.; Li, X.; Zhang, X.; Lan, Q.; Xu, T., Coaxial 3D bioprinting of self-assembled multicellular heterogeneous tumor fibers. *Scientific reports* **2017,** *7* (1), 1-11.
30. Gao, Q.; He, Y.; Fu, J.-z.; Liu, A.; Ma, L., Coaxial nozzle-assisted 3D bioprinting with built-in microchannels for nutrients delivery. *Biomaterials* **2015,** *61*, 203-215.
31. Zhang, W.; Feng, C.; Yang, G.; Li, G.; Ding, X.; Wang, S.; Dou, Y.; Zhang, Z.; Chang, J.; Wu, C., 3D-printed scaffolds with synergistic effect of hollow-pipe structure and bioactive ions for vascularized bone regeneration. *Biomaterials* **2017,** *135*, 85-95.
32. Jia, W.; Gungor-Ozkerim, P. S.; Zhang, Y. S.; Yue, K.; Zhu, K.; Liu, W.; Pi, Q.; Byambaa, B.; Dokmeci, M. R.; Shin, S. R., Direct 3D bioprinting of perfusable vascular constructs using a blend bioink. *Biomaterials* **2016,** *106*, 58-68.
33. Zhang, R.; Larsen, N. B., Stereolithographic hydrogel printing of 3D culture chips with biofunctionalized complex 3D perfusion networks. *Lab on a Chip* **2017,** *17* (24), 4273-4282.

34. Cui, H.; Esworthy, T.; Zhou, X.; Hann, S. Y.; Glazer, R. I.; Li, R.; Zhang, L. G., Engineering a novel 3D printed vascularized tissue model for investigating breast cancer metastasis to bone. *Advanced healthcare materials* **2020,** *9* (15), 1900924.
35. Murphy, S. V.; De Coppi, P.; Atala, A., Opportunities and challenges of translational 3D bioprinting. *Nature biomedical engineering* **2019**, 1-11.
36. Park, J. H.; Jang, J.; Lee, J.-S.; Cho, D.-W. J. A. o. b. e., Three-dimensional printing of tissue/organ analogues containing living cells. **2017,** *45* (1), 180-194.
37. Derby, B. J. S., Printing and prototyping of tissues and scaffolds. **2012,** *338* (6109), 921-926.
38. Hong, S.; Sycks, D.; Chan, H. F.; Lin, S.; Lopez, G. P.; Guilak, F.; Leong, K. W.; Zhao, X., 3D printing of highly stretchable and tough hydrogels into complex, cellularized structures. *Advanced materials* **2015,** *27* (27), 4035-4040.
39. Highley, C.; Rodell, C.; Burdick, J. In *Direct 3D printing of shear-thinning hydrogels at high resolution using open-source technologies*, Front. Bioeng. Biotechnol. Conference Abstract: 10th World Biomaterials Congress. doi: 10.3389/conf. FBIOE, 2016.
40. Włodarczyk-Biegun, M. K.; del Campo, A., 3D bioprinting of structural proteins. *Biomaterials* **2017,** *134*, 180-201.
41. Cui, X.; Boland, T., Human microvasculature fabrication using thermal inkjet printing technology. *Biomaterials* **2009,** *30* (31), 6221-6227.
42. Ma, X.; Yu, C.; Wang, P.; Xu, W.; Wan, X.; Lai, C. S. E.; Liu, J.; Koroleva-Maharajh, A.; Chen, S., Rapid 3D bioprinting of decellularized extracellular matrix with regionally varied mechanical properties and biomimetic microarchitecture. *Biomaterials* **2018,** *185*, 310-321.
43. Noor, N.; Shapira, A.; Edri, R.; Gal, I.; Wertheim, L.; Dvir, T., 3D Printing of Personalized Thick and Perfusable Cardiac Patches and Hearts. *Advanced Science* **2019**, 1900344.
44. Lee, A.; Hudson, A.; Shiwarski, D.; Tashman, J.; Hinton, T.; Yerneni, S.; Bliley, J.; Campbell, P.; Feinberg, A., 3D bioprinting of collagen to rebuild components of the human heart. *Science* **2019,** *365* (6452), 482-487.
45. Wise, S. G.; Yeo, G. C.; Hiob, M. A.; Rnjak-Kovacina, J.; Kaplan, D. L.; Ng, M. K.; Weiss, A. S., Tropoelastin: a versatile, bioactive assembly module. *Acta biomaterialia* **2014,** *10* (4), 1532-1541.
46. Williamson, M. R.; Shuttleworth, A.; Canfield, A. E.; Black, R. A.; Kielty, C. M., The role of endothelial cell attachment to elastic fibre molecules in the enhancement of monolayer formation and retention, and the inhibition of smooth muscle cell recruitment. *Biomaterials* **2007,** *28* (35), 5307-5318.
47. Yin, Y.; Wise, S. G.; Nosworthy, N. J.; Waterhouse, A.; Bax, D. V.; Youssef, H.; Byrom, M. J.; Bilek, M. M.; McKenzie, D. R.; Weiss, A. S., Covalent immobilisation of tropoelastin on a plasma deposited interface for enhancement of endothelialisation on metal surfaces. *Biomaterials* **2009,** *30* (9), 1675-1681.
48. Sani, E. S.; Lara, R. P.; Aldawood, Z.; Bassir, S. H.; Nguyen, D.; Kantarci, A.; Intini, G.; Annabi, N. J. M., An Antimicrobial Dental Light Curable Bioadhesive Hydrogel for Treatment of Peri-Implant Diseases. **2019**.
49. Annabi, N.; Mithieux, S. M.; Zorlutuna, P.; Camci-Unal, G.; Weiss, A. S.; Khademhosseini, A., Engineered cell-laden human protein-based elastomer. *Biomaterials* **2013,** *34* (22), 5496-5505.

50. Noshadi, I.; Hong, S.; Sullivan, K. E.; Shirzaei Sani, E.; Portillo-Lara, R.; Tamayol, A.; Shin, S. R.; Gao, A. E.; Stoppel, W. L.; Black Iii, L. D.; Khademhosseini, A.; Annabi, N., In vitro and in vivo analysis of visible light crosslinkable gelatin methacryloyl (GelMA) hydrogels. *Biomater Sci* **2017**.
51. Yue, K.; Trujillo-de Santiago, G.; Alvarez, M. M.; Tamayol, A.; Annabi, N.; Khademhosseini, A., Synthesis, properties, and biomedical applications of gelatin methacryloyl (GelMA) hydrogels. *Biomaterials* **2015,** *73*, 254-271.
52. Yeo, G. C.; Keeley, F. W.; Weiss, A. S., Coacervation of tropoelastin. *Advances in colloid and interface science* **2011,** *167* (1-2), 94-103.
53. Annabi, N.; Zhang, Y.-N.; Assmann, A.; Sani, E. S.; Cheng, G.; Lassaletta, A. D.; Vegh, A.; Dehghani, B.; Ruiz-Esparza, G. U.; Wang, X. J. S. t. m., Engineering a highly elastic human protein–based sealant for surgical applications. **2017,** *9* (410), eaai7466.
54. Soucy, J. R.; Shirzaei Sani, E.; Portillo Lara, R.; Diaz, D.; Dias, F.; Weiss, A. S.; Koppes, A. N.; Koppes, R. A.; Annabi, N., Photocrosslinkable Gelatin/Tropoelastin Hydrogel Adhesives for Peripheral Nerve Repair. *Tissue Engineering Part A* **2018**.
55. Annabi, N.; Rana, D.; Sani, E. S.; Portillo-Lara, R.; Gifford, J. L.; Fares, M. M.; Mithieux, S. M.; Weiss, A. S., Engineering a sprayable and elastic hydrogel adhesive with antimicrobial properties for wound healing. *Biomaterials* **2017,** *139*, 229-243.
56. Assmann, A.; Vegh, A.; Ghasemi-Rad, M.; Bagherifard, S.; Cheng, G.; Sani, E. S.; Ruiz-Esparza, G. U.; Noshadi, I.; Lassaletta, A. D.; Gangadharan, S.; Tamayol, A.; Khademhosseini, A.; Annabi, N., A highly adhesive and naturally derived sealant. *Biomaterials* **2017,** *140*, 115-127.
57. Sinha, R. P.; Häder, D.-P., UV-induced DNA damage and repair: a review. *Photochemical & Photobiological Sciences* **2002,** *1* (4), 225-236.
58. Soucy, J. R.; Askaryan, J.; Diaz, D.; Koppes, A. N.; Annabi, N.; Koppes, R. A., Glial cells influence cardiac permittivity as evidenced through in vitro and in silico models. *Biofabrication* **2019,** *12* (1), 015014.
59. Yeh, Y.-C.; Highley, C. B.; Ouyang, L.; Burdick, J. A., 3D printing of photocurable poly (glycerol sebacate) elastomers. *Biofabrication* **2016,** *8* (4), 045004.
60. Shin, S.; Park, S.; Park, M.; Jeong, E.; Na, K.; Youn, H. J.; Hyun, J., Cellulose nanofibers for the enhancement of printability of low viscosity gelatin derivatives. *BioResources* **2017,** *12* (2), 2941-2954.
61. Jungst, T.; Smolan, W.; Schacht, K.; Scheibel, T.; Groll, J. r., Strategies and molecular design criteria for 3D printable hydrogels. *Chemical reviews* **2015,** *116* (3), 1496-1539.
62. Yang, F.; Tadepalli, V.; Wiley, B. J., 3D printing of a double network hydrogel with a compression strength and elastic modulus greater than those of cartilage. *ACS Biomaterials Science & Engineering* **2017,** *3* (5), 863-869.
63. Chimene, D.; Peak, C. W.; Gentry, J. L.; Carrow, J. K.; Cross, L. M.; Mondragon, E.; Cardoso, G. B.; Kaunas, R.; Gaharwar, A. K., Nanoengineered ionic–covalent entanglement (NICE) bioinks for 3D bioprinting. *ACS applied materials & interfaces* **2018,** *10* (12), 9957-9968.
64. Compaan, A. M.; Christensen, K.; Huang, Y., Inkjet bioprinting of 3D silk fibroin cellular constructs using sacrificial alginate. *ACS Biomaterials Science & Engineering* **2016,** *3* (8), 1519-1526.
65. Kraut, G.; Yenchesky, L.; Prieto, F.; Tovar, G. E.; Southan, A., Influence of shear thinning and material flow on robotic dispensing of poly (ethylene glycol) diacrylate/poloxamer 407 hydrogels. *Journal of Applied Polymer Science* **2017,** *134* (29), 45083.

66. Hinton, T. J.; Jallerat, Q.; Palchesko, R. N.; Park, J. H.; Grodzicki, M. S.; Shue, H.-J.; Ramadan, M. H.; Hudson, A. R.; Feinberg, A. W., Three-dimensional printing of complex biological structures by freeform reversible embedding of suspended hydrogels. *Science advances* **2015,** *1* (9), e1500758.
67. Nguyen, D.; Hägg, D. A.; Forsman, A.; Ekholm, J.; Nimkingratana, P.; Brantsing, C.; Kalogeropoulos, T.; Zaunz, S.; Concaro, S.; Brittberg, M., Cartilage tissue engineering by the 3D bioprinting of iPS cells in a nanocellulose/alginate bioink. *Scientific reports* **2017,** *7* (1), 1-10.
68. Kang, H.-W.; Lee, S. J.; Ko, I. K.; Kengla, C.; Yoo, J. J.; Atala, A., A 3D bioprinting system to produce human-scale tissue constructs with structural integrity. *Nature biotechnology* **2016,** *34* (3), 312.
69. Malik, A. B.; Lynch, J. J.; Cooper, J. A., Endothelial barrier function. *Journal of Investigative Dermatology* **1989,** *93* (2), S62-S67.
70. Santana, L. F.; Cheng, E. P.; Lederer, W. J., How does the shape of the cardiac action potential control calcium signaling and contraction in the heart? *Journal of molecular and cellular cardiology* **2010,** *49* (6), 901.
71. Sani, E. S.; Kheirkhah, A.; Rana, D.; Sun, Z.; Foulsham, W.; Sheikhi, A.; Khademhosseini, A.; Dana, R.; Annabi, N., Sutureless repair of corneal injuries using naturally derived bioadhesive hydrogels. *Science Advances* **2019,** *5*, eaav1281.
72. Baldock, C.; Oberhauser, A. F.; Ma, L.; Lammie, D.; Siegler, V.; Mithieux, S. M.; Tu, Y.; Chow, J. Y. H.; Suleman, F.; Malfois, M., Shape of tropoelastin, the highly extensible protein that controls human tissue elasticity. *Proceedings of the National Academy of Sciences* **2011,** *108* (11), 4322-4327.
73. Annabi, N.; Zhang, Y.-N.; Assmann, A.; Sani, E. S.; Cheng, G.; Lassaletta, A. D.; Vegh, A.; Dehghani, B.; Ruiz-Esparza, G. U.; Wang, X., Engineering a highly elastic human protein–based sealant for surgical applications. *Science translational medicine* **2017,** *9* (410), eaai7466.
74. Spencer, A.; Shirzaei Sani, E.; Soucy, J. R.; Corbet, C. C.; Primbetova, A.; Koppes, R. A.; Annabi, N., Bioprinting of a cell-laden conductive hydrogel composite. *ACS applied materials & interfaces* **2019**.
75. Soucy, J. R.; Askaryan, J.; Diaz, D.; Koppes, A. N.; Annabi, N.; Koppes, R., Glial cells in the heart? Replicating the diversity of the myocardium with low-cost 3D models. *Replicating the Diversity of the Myocardium with Low-Cost 3D Models* **2018**.
76. Williamson, I. A.; Arnold, J. W.; Samsa, L. A.; Gaynor, L.; DiSalvo, M.; Cocchiaro, J. L.; Carroll, I.; Azcarate-Peril, M. A.; Rawls, J. F.; Allbritton, N. L., A high-throughput organoid microinjection platform to study gastrointestinal microbiota and luminal physiology. *Cellular and molecular gastroenterology and hepatology* **2018,** *6* (3), 301-319.
77. Griffin, D. R.; Weaver, W. M.; Scumpia, P. O.; Di Carlo, D.; Segura, T., Accelerated wound healing by injectable microporous gel scaffolds assembled from annealed building blocks. *Nature materials* **2015,** *14* (7), 737.
78. Wu, C.-Y.; Ouyang, M.; Wang, B.; de Rutte, J.; Joo, A.; Jacobs, M.; Ha, K.; Bertozzi, A. L.; Di Carlo, D., Monodisperse drops templated by 3D-structured microparticles. *Science Advances* **2020,** *6* (45), eabb9023.
79. de Rutte, J.; Dimatteo, R.; van Zee, M.; Damoiseaux, R.; Di Carlo, D., Massively parallel encapsulation of single cells with structured microparticles and secretion-based flow sorting. *BioRxiv* **2020**.

80. Prakash, S.; Ashley, B. K.; Doyle, P. S.; Hassan, U., Design of a Multiplexed Analyte Biosensor using Digital Barcoded Particles and Impedance Spectroscopy. *Scientific reports* **2020,** *10* (1), 1-10.
81. Pregibon, D. C.; Toner, M.; Doyle, P. S., Multifunctional Encoded Particles for High-Throughput Biomolecule Analysis. *Science* **2007,** *315* (5817), 1393-1396.
82. Perry, J. L.; Reuter, K. G.; Kai, M. P.; Herlihy, K. P.; Jones, S. W.; Luft, J. C.; Napier, M.; Bear, J. E.; DeSimone, J. M., PEGylated PRINT nanoparticles: the impact of PEG density on protein binding, macrophage association, biodistribution, and pharmacokinetics. *Nano letters* **2012,** *12* (10), 5304-5310.
83. Dendukuri, D.; Pregibon, D. C.; Collins, J.; Hatton, T. A.; Doyle, P. S., Continuous-flow lithography for high-throughput microparticle synthesis. *Nature materials* **2006,** *5* (5), 365-369.
84. Bong, K. W.; Kim, J. J.; Cho, H.; Lim, E.; Doyle, P. S.; Irimia, D., Synthesis of Cell-Adhesive Anisotropic Multifunctional Particles by Stop Flow Lithography and Streptavidin–Biotin Interactions. *Langmuir* **2015,** *31* (48), 13165-13171.
85. Wang, W.; Zhang, M. J.; Xie, R.; Ju, X. J.; Yang, C.; Mou, C. L.; Weitz, D. A.; Chu, L. Y., Hole–shell microparticles from controllably evolved double emulsions. *Angewandte Chemie International Edition* **2013,** *52* (31), 8084-8087.
86. Li, W.; Zhang, L.; Ge, X.; Xu, B.; Zhang, W.; Qu, L.; Choi, C.-H.; Xu, J.; Zhang, A.; Lee, H., Microfluidic fabrication of microparticles for biomedical applications. *Chemical Society Reviews* **2018,** *47* (15), 5646-5683.
87. van Zee, M.; de Rutte, J.; Rumyan, R.; Williamson, C.; Burnes, T.; Radakovits, R.; Eugenio, A. S.; Badih, S.; Lee, D.-H.; Archang, M., High-throughput selection of microalgae based on biomass accumulation rates in production environments using PicoShell Particles. *bioRxiv* **2021**.
88. Pushkarsky, I.; Tseng, P.; Black, D.; France, B.; Warfe, L.; Koziol-White, C. J.; Jester, W. F.; Trinh, R. K.; Lin, J.; Scumpia, P. O., Elastomeric sensor surfaces for high-throughput single-cell force cytometry. *Nature biomedical engineering* **2018,** *2* (2), 124-137.
89. Bose, S.; Wan, Z.; Carr, A.; Rizvi, A. H.; Vieira, G.; Pe'er, D.; Sims, P. A., Scalable microfluidics for single-cell RNA printing and sequencing. *Genome biology* **2015,** *16* (1), 1-16.
90. Li, X.; Zhang, D.; Zhang, H.; Guan, Z.; Song, Y.; Liu, R.; Zhu, Z.; Yang, C., Microwell array method for rapid generation of uniform agarose droplets and beads for single molecule analysis. *Analytical chemistry* **2018,** *90* (4), 2570-2577.
91. Amstad, E.; Chemama, M.; Eggersdorfer, M.; Arriaga, L. R.; Brenner, M. P.; Weitz, D. A., Robust scalable high throughput production of monodisperse drops. *Lab on a Chip* **2016,** *16* (21), 4163-4172.
92. Muluneh, M.; Issadore, D., Hybrid soft-lithography/laser machined microchips for the parallel generation of droplets. *Lab on a Chip* **2013,** *13* (24), 4750-4754.
93. Dhar, M.; Lam, J. N.; Walser, T.; Dubinett, S. M.; Rettig, M. B.; Di Carlo, D., Functional profiling of circulating tumor cells with an integrated vortex capture and single-cell protease activity assay. *Proceedings of the National Academy of Sciences* **2018,** *115* (40), 9986-9991.
94. Liu, Q.; Zhao, M.; Mytnyk, S.; Klemm, B.; Zhang, K.; Wang, Y.; Yan, D.; Mendes, E.; van Esch, J. H., Self‐Orienting Hydrogel Micro‐Buckets as Novel Cell Carriers. *Angewandte Chemie* **2019,** *131* (2), 557-561.

95. Ma, S.; Thiele, J.; Liu, X.; Bai, Y.; Abell, C.; Huck, W. T., Fabrication of microgel particles with complex shape via selective polymerization of aqueous two‐phase systems. *Small* **2012,** *8* (15), 2356-2360.
96. Johansson, G.; Walter, H., Partitioning and concentrating biomaterials in aqueous phase systems. *International review of cytology* **1999,** *192*, 33-60.
97. Yanagisawa, M.; Yamashita, Y.; Mukai, S.-a.; Annaka, M.; Tokita, M., Phase separation in binary polymer solution: Gelatin/poly (ethylene glycol) system. *Journal of Molecular Liquids* **2014,** *200*, 2-6.
98. Torza, S.; Mason, S., Three-phase interactions in shear and electrical fields. *Journal of colloid and interface science* **1970,** *33* (1), 67-83.
99. Sugiura, S.; Nakajima, M.; Seki, M., Preparation of monodispersed emulsion with large droplets using microchannel emulsification. *Journal of the American Oil Chemists' Society* **2002,** *79* (5), 515-519.
100. Sugiura, S.; Nakajima, M.; Iwamoto, S.; Seki, M., Interfacial tension driven monodispersed droplet formation from microfabricated channel array. *Langmuir* **2001,** *17* (18), 5562-5566.
101. Collins, D. J.; Neild, A.; DeMello, A.; Liu, A.-Q.; Ai, Y., The Poisson distribution and beyond: methods for microfluidic droplet production and single cell encapsulation. *Lab on a Chip* **2015,** *15* (17), 3439-3459.
102. Mollet, M.; Godoy-Silva, R.; Berdugo, C.; Chalmers, J. J., Computer simulations of the energy dissipation rate in a fluorescence-activated cell sorter: Implications to cells. *Biotechnol Bioeng* **2008,** *100* (2), 260-72.
103. Stolovicki, E.; Ziblat, R.; Weitz, D. A., Throughput enhancement of parallel step emulsifier devices by shear-free and efficient nozzle clearance. *Lab on a Chip* **2018,** *18* (1), 132-138.
104. June, C. H.; Blazar, B. R.; Riley, J. L., Engineering lymphocyte subsets: tools, trials and tribulations. *Nature Reviews Immunology* **2009,** *9* (10), 704-716.
105. Wu, C.-Y.; Stoecklein, D.; Kommajosula, A.; Lin, J.; Owsley, K.; Ganapathysubramanian, B.; Di Carlo, D., Shaped 3D microcarriers for adherent cell culture and analysis. *Microsystems & nanoengineering* **2018,** *4* (1), 1-9.
106. Koh, J.; Griffin, D. R.; Archang, M. M.; Feng, A. C.; Horn, T.; Margolis, M.; Zalazar, D.; Segura, T.; Scumpia, P. O.; Di Carlo, D., Enhanced in vivo delivery of stem cells using microporous annealed particle scaffolds. *Small* **2019,** *15* (39), 1903147.
107. Kuribayashi-Shigetomi, K.; Onoe, H.; Takeuchi, S., Cell origami: self-folding of three-dimensional cell-laden microstructures driven by cell traction force. *PloS one* **2012,** *7* (12), e51085.
108. Ferreira, L. M.; Muller, Y. D.; Bluestone, J. A.; Tang, Q., Next-generation regulatory T cell therapy. *Nature reviews Drug discovery* **2019,** *18* (10), 749-769.
109. Waldman, A. D.; Fritz, J. M.; Lenardo, M. J., A guide to cancer immunotherapy: from T cell basic science to clinical practice. *Nature Reviews Immunology* **2020,** *20* (11), 651-668.
110. Ma, P.; Ren, P.; Zhang, C.; Tang, J.; Yu, Z.; Zhu, X.; Fan, K.; Li, G.; Zhu, W.; Sang, W., Avidity‐Based Selection of Tissue‐Specific CAR‐T Cells from a Combinatorial Cellular Library of CARs. *Advanced Science* **2021,** *8* (6), 2003091.
111. Rafiq, S.; Hackett, C. S.; Brentjens, R. J., Engineering strategies to overcome the current roadblocks in CAR T cell therapy. *Nature reviews Clinical oncology* **2020,** *17* (3), 147-167.

112. Bloemberg, D.; McComb, S.; Weeratna, R., Building a better CAR: emerging high-throughput in vitro tools for CAR selection and optimization. *Cell & Gene Therapy Insights* **2019,** *5*, 681-692.
113. Chu, W.; Zhou, Y.; Tang, Q.; Wang, M.; Ji, Y.; Yan, J.; Yin, D.; Zhang, S.; Lu, H.; Shen, J., Bi-specific ligand-controlled chimeric antigen receptor T-cell therapy for non-small cell lung cancer. *BioScience trends* **2018**.
114. Kim, M. S.; Ma, J. S.; Yun, H.; Cao, Y.; Kim, J. Y.; Chi, V.; Wang, D.; Woods, A.; Sherwood, L.; Caballero, D., Redirection of genetically engineered CAR-T cells using bifunctional small molecules. *Journal of the American Chemical Society* **2015,** *137* (8), 2832-2835.
115. Lee, S.; de Rutte, J.; Dimatteo, R.; Koo, D.; Di Carlo, D., Scalable fabrication and use of 3D structured microparticles spatially functionalized with biomolecules. *ACS nano* **2021**.
116. Altin, J. G.; Sloan, E. K., The role of CD45 and CD45 - associated molecules in T cell activation. *Immunology and cell biology* **1997,** *75* (5), 430-445.
117. Han, Q.; Bradshaw, E. M.; Nilsson, B.; Hafler, D. A.; Love, J. C., Multidimensional analysis of the frequencies and rates of cytokine secretion from single cells by quantitative microengraving. *Lab on a chip* **2010,** *10* (11), 1391-1400.
118. Lu, Y.; Xue, Q.; Eisele, M. R.; Sulistijo, E. S.; Brower, K.; Han, L.; Amir, E.-a. D.; Pe'er, D.; Miller-Jensen, K.; Fan, R., Highly multiplexed profiling of single-cell effector functions reveals deep functional heterogeneity in response to pathogenic ligands. *Proceedings of the National Academy of Sciences* **2015,** *112* (7), E607-E615.
119. Minami, Y.; Samelson, L. E.; Klausner, R. D., Internalization and cycling of the T cell antigen receptor. Role of protein kinase C. *Journal of Biological Chemistry* **1987,** *262* (27), 13342-13347.
120. Uggeri, J.; Gatti, R.; Belletti, S.; Scandroglio, R.; Corradini, R.; Rotoli, B. M.; Orlandini, G., Calcein-AM is a detector of intracellular oxidative activity. *Histochemistry and cell biology* **2000,** *122* (5), 499-505.
121. Lee, Y. G.; Marks, I.; Srinivasarao, M.; Kanduluru, A. K.; Mahalingam, S. M.; Liu, X.; Chu, H.; Low, P. S., Use of a single CAR T cell and several bispecific adapters facilitates eradication of multiple antigenically different solid tumors. *Cancer Research* **2019,** *79* (2), 387-396.